Spring 4-15-2019

A Transient Thermal and Structural Analysis of Fuel in the Annular Core Research Reactor

Elliott Pelfrey
University of New Mexico

Follow this and additional works at: https://digitalrepository.unm.edu/me_etds

Part of the Mechanical Engineering Commons

Elliott Pelfrey
_____

Candidate

Mechanical Engineering
_____

Department

This thesis is approved, and it is acceptable in quality and form for publication:

Approved by the Thesis Committee:

Dr. Yu-Lin Shen   , Chairperson
_____

Dr. Nima Fathi
_____

Dr. Edward Parma
_____

_____

_____

_____

_____

_____

A TRANSIENT THERMAL AND STRUCTURAL ANALYSIS
OF FUEL IN THE ANNULAR CORE RESEARCH REACTOR

by

ELLIOTT PELFREY

B.S., MECHANICAL ENGINEERING,
UNIVERSITY OF NEW MEXICO, 2017

THESIS

Submitted in Partial Fulfillment of the
Requirements for the Degree of

Master of Science
Mechanical Engineering

The University of New Mexico
Albuquerque, New Mexico

May, 2019

ACKNOWLEDGEMENTS

I would like to express the greatest appreciation to my mentors, Ed Parma and Darren Talley, for the patience, support, advice, and time they have dedicated to help me succeed. I would also like to extend my gratitude to Curtis Peters and Aaron Miller for their assistance with this thesis. Without their help, this work would not have been possible. I would like to thank Tommy Ball for his friendship, guidance, and support through the course this project. Also, I would like to thank Dr. Shen for answering all of my questions as well as being the chair of my committee. I would also like to thank Dr. Fathi for being on my committee. Most of all I would like to thank my wonderful wife, Jocelyn, for all of her love and encouragement throughout this project.

A Transient Thermal and Structural Analysis of Fuel in

the Annular Core Research Reactor

by

ELLIOTT PELFREY

B.S., Mechanical Engineering, University of New Mexico, 2017

M.S., Mechanical Engineering, University of New Mexico, 2019

ABSTRACT

The health of a nuclear reactor's fuel is essential to the operational longevity of the reactor. The health of the fuel in the Annular Core Research Reactor (ACRR) is a topic of increased interest due to both a proposed new facility that would include the ACRR and the recent resurfacing of contradictory reports regarding thermal stresses in its fuel pellets. Unlike other reactor fuels, which are widely used and well-characterized, the fuel in the ACRR is unique. The ACRR's fuel elements consist of UO_2-BeO fuel pellets, fluted niobium refractory liners, and stainless-steel cladding. The purpose of this thesis is to examine the thermal stresses in the ACRR's peak fuel pellets under maximum pulse conditions. Because the properties are not well-characterized, the material properties of the fresh fuel pellets were first determined using approximations including the rule of mixtures and the Voigt-Reuss-Hill approximation. Then the material properties were

adjusted to account for the effects of burnup and radiation. Next a transient thermal analysis was performed using the commercial finite element code ANSYS Mechanical 19.2. The temperature gradients calculated in the transient thermal analysis were used to calculate the thermal stresses in the fuel pellets. The thermal stresses were also calculated using ANSYS Mechanical 19.2. Using the same process, a material sensitivity study was performed to examine the sensitivity of the thermal stresses to the material properties. Finally, the effects of the thermal stresses were examined from a fracture mechanics perspective. The analyses showed that the fuel pellets experience large thermal stresses that are caused by the fuel element's unique geometry. Despite the large thermal stresses, it was concluded that the thermal stresses are unlikely to cause fracture.

TABLE OF CONTENTS

LIST OF FIGURES

LIST OF TABLES

1 INTRODUCTION

The purpose of this thesis was to calculate the thermal stresses in the Annular Core Research Reactor's (ACRR) fuel pellets. This work was initiated due to a recent proposal for a new facility that would include the ACRR and the resurfacing of contradicting reports regarding the thermal stresses in the ACRR's fuel. A nuclear reactor's longevity is highly dependent on the fuel's ability to withstand the induced thermal stresses without fracturing excessively. If the fuel does experience repeated fracture, the fuel's ability to dissipate heat can be affected causing excessive heating of the fuel. Exceeding the temperature limits for the fuel can have an impact on the structural integrity of the fuel elements.

Thermal stresses are dependent on a material's properties and the temperature gradients within the material. Because the properties of the fuel used in the ACRR are not well documented and the fuel used in the ACRR is unique, Chapters 3 and 4 are dedicated to approximating the current material properties of the fuel pellets. The temperature gradients and resultant thermal stresses are documented in Chapter 5. Because the material properties are uncertain, a property sensitivity study was performed and documented in Chapter 6 to better understand how much each property affects the thermal stresses. Finally, Chapter 7 documents the implications of the thermal stresses from a fracture mechanics perspective.

This thesis documents the approximate material properties of the fresh fuel at its current level of burnup. Also, this thesis documents the most detailed thermal and structural analysis ever performed on the ACRR's fuel. Finally, this thesis presents how material properties impact the thermal stresses in the ACRR's fuel pellets.

1.1 Annular Core Research Reactor

The Annular Core Research Reactor (ACRR) was developed in the 1970's and became operational in 1978. It was originally designed as part of a fast reactor safety program; however, it is now primarily used to perform radiation effects testing on electronic components. The ACRR is a TRIGA type reactor that consists of 236 fuel elements with UO_2-BeO fuel pellets [1]–[4]. The fuel elements are arranged in an annulus around a 9" dry central cavity. The ACRR can be coupled with the Fuel Ringed External Cavity-II (FREC-II) which is a subcritical neutron multiplier with its own 20" dry cavity. The dry cavities enable experiments to be placed at the reactor centerline.

The ACRR is operated by adjusting its 11 moveable elements to control the reactivity of the reactor. The 11 moveable rods consist of six control rods, three transient rods, and two safety rods. The moveable rods all contain a boron carbide upper portion that absorbs neutrons and both the safety and control rods have fuel in the lower half. To operate the reactor, the safety rods are moved to the up position, and the control rods are adjusted depending on the desired steady-state power or pulse size. In pulse operations, the transient rods are ejected using pressurized nitrogen causing the ACRR to go prompt supercritical. During pulses, the ACRR shuts itself down due to doppler broadening effects in the fuel. The ACRR is capable of operating at 4 MW steady-state and reaching pulse powers up to 50,000 MW_{th} with total energy yields over 300 MJ. The maximum pulse operations cause the maximum stresses that are experienced by the fuel. Figure 1.1 shows the ACRR during

a pulse operation with a blue glow caused by Cherenkov radiation. Figure 1.2 shows the

ACRR's dry central cavity where experiments are placed [5].
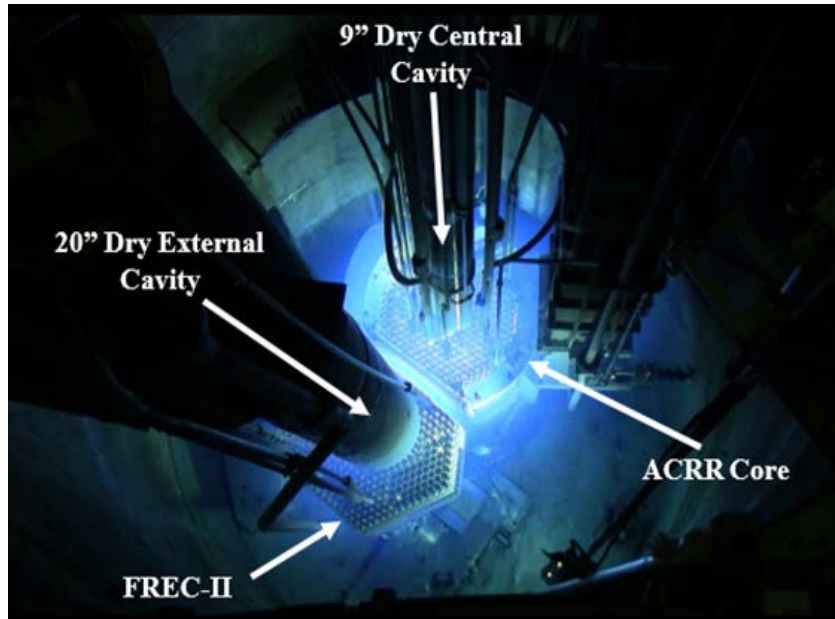
Figure 1.1: The ACRR during pulse operation with FREC-II decoupled.
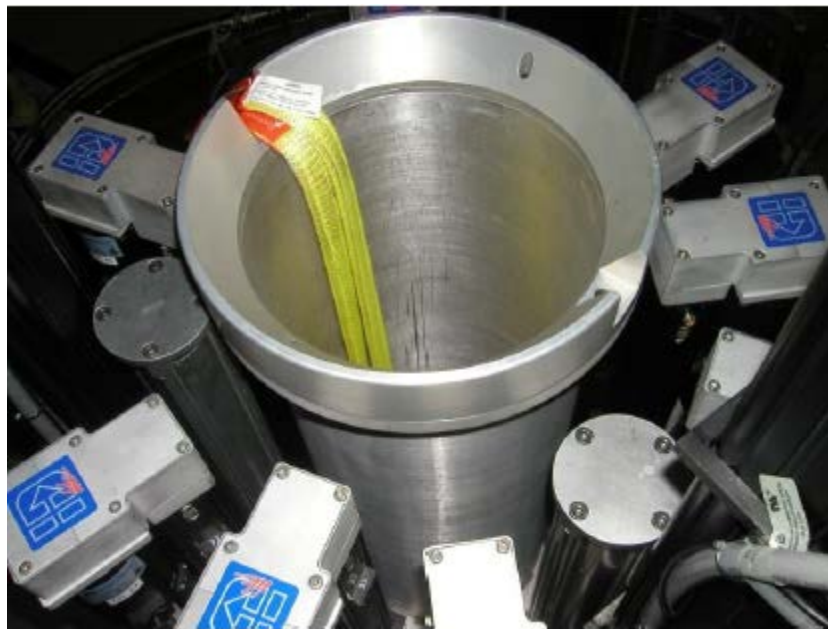
Figure 1.2: The ACRR's dry central cavity.

1.2 Fuel Elements

The most unique feature of the ACRR is its UO_2-BeO fuel pellets. The BeO allows the fuel to have a large thermal conductivity. The large thermal conductivity reduces stresses during transient operations, allowing for large pulses. The fuel pellets contain 6.9 volume percent (v/o) UO_2 that is enriched to 35% ^{235}U. The fuel pellets were manufactured to have UO_2 dispersions no larger than 1 µm [6]. Each fuel pellet was manufactured by being cold pressed and sintered to 99% of the material's theoretical density.

The fuel elements in the ACRR consist of 304 stainless-steel (SS) cladding, five niobium (Nb) cans which contain 16 fuel pellets per can. A fuel element is shown in Figure 1.3. Each fuel pellet consists of a split inner annulus and a split outer annulus totaling four pieces per pellet. The fuel elements were evacuated and then backfilled with helium (He) to a pressure of 2 atm [7]. The Nb cans were included in the fuel elements to provide a refractory metal barrier between the fuel and the cladding. The Nb cans are also designed to contain the fuel if excessive fracture does occur [6], [8]. The Nb cans are fluted to maintain proper spacing between the fuel pellets and the SS cladding. The fuel elements are 2.5 feet tall and 1.5 inches in diameter. Each fuel element has approximately 101 g of ^{235}U. Figure 1.4 shows a cross-section of a fuel element with the fuel element split along a horizontal plane. In Figure 1.4 the SS cladding, fluted Nb can, and split fuel pellet are all shown.
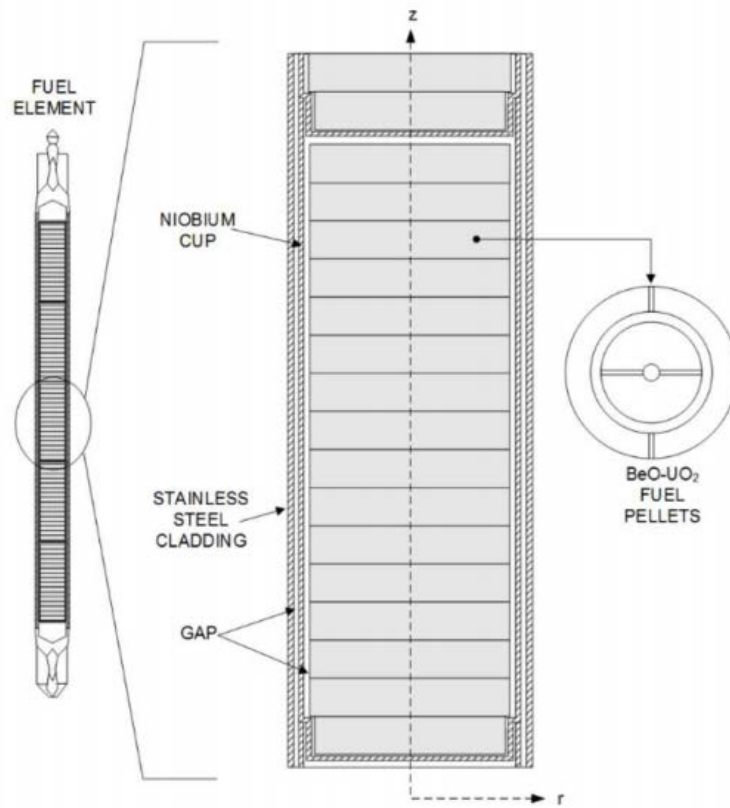
Figure 1.3: Schematic of an ACRR fuel element [9].
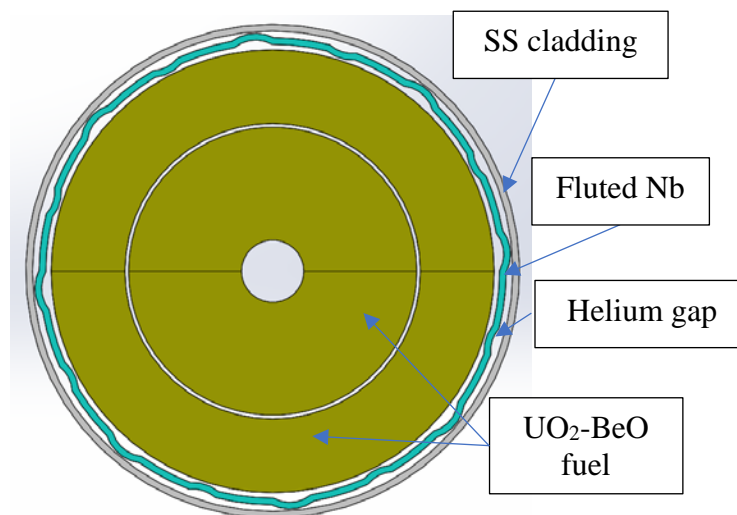
Figure 1.4: Cross-sectional view of the ACRR's fuel element.

1.3 Heating in a Nuclear Reactor

Heat is generated in a nuclear reactor when fission occurs. A fission occurs when a neutron is absorbed by a fissile atom making the atom unstable. The unstable atom splits emitting gamma-rays, neutrons, and fission fragments. Although the neutrons and gamma-rays can leave the site of fission, the fission fragments deposit their energy in the material within several microns of the fission site. It is the deposition of fission fragment, neutron, and gamma-ray energy that heats the materials in the reactor core. The heating of a specific volume of fuel is directly related to the number of fissions that occur within that volume. Due to the neutronics of nuclear reactors, more fissions occur towards the reactor's center and around its axial centerline. The increased amount of fissions leads to regionally dependent heating of the fuel. The location where the most fissions occur is called the peak location.

The number of fissions also vary locally within fuel pellets. More fissions occur near the outer surface of the fuel than in the inner region. Neutron self-shielding effects cause this phenomenon. The radial fission profile within the peak fuel pellet within the ACRR is shown in Figure 1.5. Figure 1.5 shows that ~1.2 times more fission occur towards the outer edge of a pellet than occur on average within the pellet. This leads to radially dependent heating in the fuel pellets. The radially dependent heating produces temperature gradients that induce stresses in the fuel.
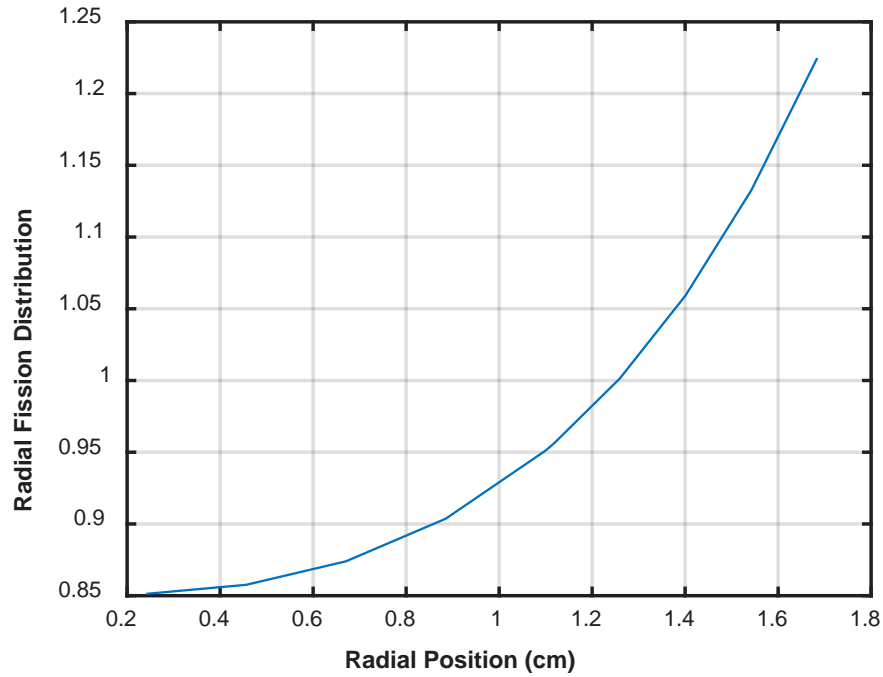
Figure 1.5: Fission distribution in a fuel pellet.

1.4 Burnup and Radiation Effects

The fission of an atom comes at a cost to the materials within the reactor. Both the interaction of the energetic particles with materials and the buildup of impurities can impact the material properties within a reactor. The amount of damage accrued by the fuel is directly related to the amount of burnup in the fuel. Burnup is a measure of how much energy has been extracted from the fuel and is proportional to the number of atoms that have fissioned. Sections 1.4.1 and 1.4.2 discuss the mechanics of damage in the fuel in more detail.

1.4.1 Buildup of Impurities

Impurities are introduced to the fuel through the transmutation and fission of atoms. Transmutation occurs when an energetic particle interacts with the nucleus of a non-fissile atom in a way that causes it to become another atom. One way that transmutations occur is when an atom absorbs a neutron which makes it unstable. The unstable isotope radioactively decays and becomes a new atom. Another way that transmutation occurs in nuclear fuel is through the transformation of a stable, non-fissile isotope into a fissile isotope. This does not change the mechanical properties of the fuel; however, it does increase the amount of fissile material in the fuel. Some of the common transmutations that occur in the ACRR are listed below. As the number of transmutations accrue, the material properties of the fuel change [10]. Equations 1.1-1.3 show common transmutations that occur in the BeO. The transmutation of Be into He creates interstitial impurities that both weaken the fuel and decrease the thermal conductivity.

$$n + {}_{4}^{9}\text{Be} \rightarrow \left[{}_{4}^{10}\text{Be} \right] \rightarrow 2n + 2{}_{2}^{4}\text{He} \qquad \text{Eqn. 1.1}$$

$$n + {}_{4}^{9}\text{Be} \rightarrow \left[{}_{4}^{10}Be \right] \rightarrow {}_{2}^{6}\text{He} + {}_{2}^{4}\text{He} \qquad \text{Eqn. 1.2}$$

$$\gamma + {}_{4}^{9}\text{Be} \xrightarrow{n} \left[{}_{4}^{8}\text{Be} \right] \rightarrow 2{}_{2}^{4}\text{He} \qquad \text{Eqn. 1.3}$$

The common transmutation that results in fissile material is shown in Eqn. 1.4 where ^{238}U absorbs a neutron and then betta decays into ^{239}Np, which undergoes another betta decay into $^{239}_{94}Pu$ which is fissile.

$$^{238}_{92}\text{U} + n \rightarrow {}^{239}_{92}\text{U} \xrightarrow{\beta^-} {}^{239}_{93}\text{Np} \xrightarrow{\beta^-} {}^{239}_{94}\text{Pu} \qquad \text{Eqn. 1.4}$$

8
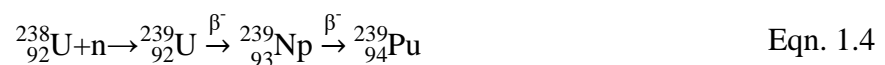
The other prominent source of impurities in the fuel is fission products. When an atom undergoes fission, it splits into at least two resultant atoms. These resultant atoms are called fission products. Common fission products of a ^{235}U fission are Xe, I, and Zr [11]. Common fission products of $^{239}_{94}Pu$ include Ba and Xe. As a nuclear reactor operates, fission products accumulate in the fuel. These fission products can affect the fuel's thermal conductivity, strength, and can cause swelling of the fuel.

1.4.2 Lattice Defects

Lattice defects occur when an energetic particle interacts with the lattice of a material. If the energetic particle has enough energy, the atom in the lattice can be knocked out its position in the lattice creating a Frenkel pair [12]. The first atom hit by the energetic partial is referred to as a primary knock-on atom (PKA). The PKA can also cause a cascade of defects when it interacts with other atoms in the lattice. The atoms that are part of the cascade are called secondary knock-on atoms (SKA). The accumulation of dislocations can cause dislocation loops, depletion zones and other defects. The accumulation of these defects can have significant impacts on a materials porosity, stiffness, strength, and thermal conductivity.

2   PREVIOUS WORK

There have been several attempts to examine whether the fuel pellets in the ACRR are capable of withstanding the stresses they experience during operation. The first attempt is documented in the "ACPR Upgrade Quarterly Reports" which were written from 1974-1977 [8], [13]–[23]. The second attempt was performed by Jack Tills and was completed in 1982 [24]. And finally, the most recent attempt was made in the mid-1990's by Steve Wright [25]. These three attempts are summarized in the following sections.

2.1 Quarterly Reports

The ACRR began as a project to upgrade the Annular Core Pulse Reactor (ACPR), which was the predecessor to the ACRR. The design process of the ACRR is thoroughly documented in the *Experimental Fast Reactor Safety Research Program* quarterly reports and later in the *Annular Core Pulse Reactor Upgrade Quarterly Report* [8], [13]–[23]. These reports provided programmatic updates on the progress being made in the Annular Core Pulse Reactor upgrade. Overall there are 12 reports that span from 1974-1977.

To determine whether the fuel pellets could survive pulses in the ACRR, the engineers who designed the ACRR placed the proposed fuel pellets in the central cavity of the ACPR and pulsed it. When the fuel was placed in the core and the reactor was pulsed, the neutrons from the pulse caused fission of the ^{235}U in the fuel pellet producing a fission distribution like the one shown in Figure 1.5. The fuel pellets tested in these experiments were enriched to 93% ^{235}U. Because the pellets were enriched to 93% ^{235}U, the fission

distribution was much more severe compared to the fission profile in a pellet enriched to 35% ^{235}U. These experiments sought to examine both the single pulse and multi-pulse survivability of the fuel. In the set of experiments aimed at testing the single-pulse survivability of the fuel, the ACPR was pulsed at increasing power levels until the fuel pellets began to fracture. In the multi-pulse survivability tests, the ACPR was pulsed multiple times at the same power level to determine if repeated pulses would fracture the fuel. From these experiments, the engineers determined that the UO_2-BeO fuel was the best candidate for the new reactor.

The results of the experiments for the UO_2-BeO fuel are displayed in Table 2.1-2.3. Table 2.1 shows the results of the single-pulse survivability tests. The first column is the approximate maximum surface temperature of the experimental fuel during the pulse. The second column is the number of fuel pellets tested and the third column is the number of pellets that fractured. As Table 2.1 shows, the fuel did not begin to fracture until the outer surface reached a temperature of 1410°C.

Table 2.1: Results of single-pulse experiments found in the ACPR upgrade quarterly reports [16],[17].

Maximum Surface Temperature (°C)	Number of Outer Samples Tested	Number of Outer Samples Fractured
650	26	0
760	12	0
890	14	0
860	12	0
960	26	0
1000	12	0
1155	18	0
1200	10	0
1320	10	0
1410	10	1

Table 2.2 shows the results of the multi-pulse survivability experiments. The pulses induced a maximum temperature of 1150°C. The table shows that although no pellets failed initially, after 51 pulses one out of ten pellets failed and after 101 pulses two out of ten pellets failed.

Table 2.2: Results of multi-pulse experiment at 1150°C found in the ACPR upgrade quarterly reports [16],[17].

Number of Pulses	Number of Outer Samples Tested	Number of Samples Outer Failed
1	8	0
11	8	0
31	8	0
51	8	1
71	8	2
101	8	2

Table 2.3 shows the results of multi-pulse experiment with the maximum fuel temperature reaching 1400°C. The table shows that from the first pulse, one out of ten pellets failed and by 71 pulses six out of the ten pellets failed. A higher failure rate was expected because the pulses were larger.

Table 2.3: Results of multi-pulse experiments at 1400°C found in the ACPR upgrade quarterly reports [16],[17].

Number of Pulses	Number of Outer Samples Tested	Number of Outer Samples Failed
1	10	1
11	10	1
31	10	1
51	10	3
71	10	6

2.2 Tills' Report

The second attempt to examine thermal stresses in the fuel came from Jack Tills of Science and Engineering Associates Inc. in 1982 [24]. The goal of Tills' work was to compare the thermal stresses of in-pile experiments, which were performed in the ACRR in 1978, to thermal stresses experienced by the fuel pellets during actual operations. Tills did this by first calculating the thermal stresses experienced by the fuel during in-pile experiments using the finite element method. Tills then performed a transient thermal analysis of maximum pulse operations in the ACRR and determined that the stresses are 1.5 times what he determined to be the fracture stress of the fuel. At the time Tills performed his analysis, the ACRR had only 226 elements. Because the ACRR only had fuel 226 elements, each fuel element produced more power to reach the same power levels currently available with 236 fuel elements. The difference in core configuration could have resulted in Tills conclusion that the size of the pulses should be limited. Unlike the experiments documented in the quarterly reports, the pellets used in the experiments had UO_2 enriched to 35% ^{235}U. A summary of the results is shown in Table 2.4. Tills found that about 25% of the pellets fail at calculated stresses of 88 MPa (12.8 ksi).

Table 2.4: Results of 1978 in-pile experiments found in Tills' report [24].

Maximum Surface Temperature (°C)	Number of Samples Tested	Number of Samples Failed	Calculated Stresses (MPa)
1182	24	0	74
1340	24	8	88

2.3 Wright's Report

Steven A. Wright of Sandia National Laboratories also performed analyses that sought to determine the health of the fuel [25]. Wright's work was initiated due to concerns that the burnup caused by production of ^{99}Mo in the ACRR would compromise the performance of the fuel. Producing ^{99}Mo requires steady-state operations which cause more burnup than pulse operations. Wright's report covered the peaking factors in the ACRR, the effects of burnup on heat transfer, the effects of burnup on material properties, and the thermal stresses experienced by the fuel during maximum pulse operations. Wright took a similar approach to Tills in that he used in-pile ACPR experiments to estimate the fracture strength of the fuel. The in-pile experiments that he used were those that had been performed as part of the ACPR upgrade program found in Section 2.1 [17]. Rather than use a finite element code to calculate the stresses, Wright used an analytical solution for calculating thermal stresses in circular square beam that is found in reference [26]. Using the calculated thermal stresses and the strength of BeO he found in other literature, Wright fit a Weibull distribution to the fracture strengths to estimate the fracture strength of the fuel. He estimated that the fracture strength of the UO$_2$-BeO fuel is around 179 MPa (26 ksi). Wright then used the analytical solution of thermal stresses in a circular-square beam to calculate the maximum thermal stresses caused by the fission profile in the ACRR's peak fuel element. He calculated that the maximum thermal stress caused by the maximum fission profile during normal ACRR operations is 56.7 MPa (8.23 ksi). Wright concluded

in his report that it is highly unlikely that the pellets will fracture during normal pulse operations.

2.4 Summary

Although the effects of thermal stresses in the ACRR fuel have been studied three times, the studies yielded different conclusions. Tills concluded that fuel could fracture under pulse operations, whereas Wright and the ACPR upgrade study found that the fuel could adequately withstand the thermal stresses experienced by the fuel pellets during pulse operations. Also, the tools used to calculate the thermal stresses were insufficient to accurately calculate the thermal stresses. Tills used a finite element code; however, his model did not include the true geometry of the Nb and did not account for the locally dependent material properties caused by the temperature gradient. Wright's analysis did not include a thermal analysis, because he assumed maximum stresses were a result of the fission profile. Also, Wright's analysis did not account for the variation of material properties across the fuel pellets due to the temperature gradient. The contradictory conclusions and deficiencies necessitated further work.

3   ESTIMATION OF BURNUP AND RADIATION EFFECTS

Section 1.4 discussed the mechanisms of property change in reactor fuel, this chapter addresses the approximate change in material properties due to the burnup. The exact effects of burnup and radiation on fuel are dependent on the fuel's composition, microstructure, and the energy spectrum of the radiation environment. Because burnup and radiation effects testing has not been performed on the ACRR's fuel, literature published on radiation effects in other BeO fuels was used to estimate the effects. Though this is not ideal, it is enough to provide an approximate change in material properties due to burnup. Section 3.1 gives the estimated burnup in the ACRR fuel as of 2017.

3.1 Estimated Burnup

As discussed in Section 1.4, the change in material properties of nuclear fuel is directly related to the burnup. Burnup calculations were not performed as part of this work, however preliminary results from work performed by Krista Kaiser of SNL were used. She calculated the estimated core-wide burnup by calculating the total mass fissioned of each fissile isotope using MCNP. Her results are shown in Table 3.1 [27].

Table 3.1: Approximate core-wide burnup in the ACRR [27].

Element	Mass (g)
^{238}U	10.00
^{235}U	150.0
^{239}Pu	15.57

The results found in Table 3.1 were converted into other commonly used units of burnup which are reported in Table 3.2. The first column of Table 3.2 is simply the total mass in grams of ^{235}U that has under gone fission from Table 3.1. The second column is the average mass of ^{235}U that has undergone fission per fuel element. The third column is the percent of the total ^{235}U that has undergone fission compared to the amount of ^{235}U that was originally in the reactor. The fourth column is the average total number of atoms that have fissioned per cubic centimeter of fuel. This number includes the fission of ^{235}U, ^{238}U, and ^{239}Pu. The fifth column is the percentage of heavy atoms that have undergone fission in the reactor. This is the total number of fissions compared to the total number of heavy atoms of any isotope that were originally in the reactor. The last column is the amount of energy in MW-days that has been extracted from the fuel.

Table 3.2: Approximate burnup in the ACRR in units of % ^{235}U, fissions/cm³, % heavy atom, and MW-day [27].

Total Mass(g) ^{235}U	Mass(g) ^{235}U per Element	% ^{235}U	Fissions/cm³	% Heavy Atom Burnup	MW-Day
150	0.64	0.63	4.4E18	0.16	167

The following sections report the best estimate of the percent change in the material properties due to burnup. Also, the following sections provide approximately how long the ACRR can operate before reaching the largest burnup reported in the cited literature. The tables in each of the following sections report the burnup associated with the property change using the same units as the original literature. They also include the burnup in units of fissions/cm^3 which is helpful in relating damage in different fuels.

3.2 Effect on Strength

As fission products build up and lattice damage occurs, materials tend to experience a reduction in strength. It is postulated that the reduction in strength, in fuels with fine fuel particles (<5 µm), is due to the damage caused by fission fragment bombardment [28]. Reference [28] documents the reduction in strength in a UO_2-BeO-ThO_2 fuel. Although this is not a perfect comparison, it is similar enough to give an estimate of the change in strength due to burnup in the ACRR fuel. In these experiments, ThO_2 and UO_2 fuel particles were dispersed in a BeO matrix and irradiated in a thermal flux in the High Flux Australian Reactor (HIFAR) which was operated by the Australian Atomic Energy Commission at Lucas Heights, Sydney Australia. There were 1.7 v/o fuel dispersions in the fuel. These experiments tested the pre and post irradiation modulus of rupture for coarse (150-200 µm), medium (30-50 µm) and fine dispersions (<5 µm). Because the ACRR's fuel contains 1 µm particles, the results for the fine dispersion fuel were used to make the comparison. Table 3.3 summarizes the change in strength with respect to burnup for the fine dispersion

19

fuel reported in reference [28]. As Table 3.3 shows, the strength of the fuel decreases as the burnup increases.

Table 3.3: The change in strength with respect to burnup in BeO-UO₂-ThO₂ fuel [28].

% Heavy Atom Burnup	Fissions/cm³	Fast Neutron Dose (neutrons/cm²)	Strength Remaining (%)
4.7	2.06E19	3.6E20	93
5	2.19E19	4.0e20	86
5.4	2.36E19	4.5e20	84

With the estimated burnup in the ACRR being 4.4E18 fissions/cm^3, the current burnup is ~20% of the lowest burnup reported in reference [28]. By linearly interpolating to determine the change in strength due to burnup, it can be estimated that there has been a 1.5% decrease in strength. At the current rate of burnup in the ACRR, the reactor will be able to operate for another ~150 years before it reaches a 7% reduction in strength.

3.3 Effect on Modulus of Elasticity

The only study found relating burnup to the modulus of elasticity is found in reference [29]. The fuel that was tested was hot-pressed to densities of 2.7 g/cm^3 and 2.9 g/cm^3 and each density had specimens with 2 w/o and 10 w/o UO$_2$. The UO$_2$ particles ranged from 6 µm-12 µm. The UO$_2$ was enriched to 30% ^{235}U. The fuel samples were irradiated in sealed aluminum cans at Hanford Engineering Works (HEW). The higher

density fuel was used for the comparison. Table 3.4 reports the change in the modulus of elasticity with respect to burnup.

Table 3.4: Change of modulus of elasticity with respect to burnup [29].

% ^{235}U	% Heavy Atom Burnup	Fissions/cm^3	Change in Modulus of Elasticity (%)
1.77	0.53	3.45E18	Not reported
3.61	1.08	7.03E18	-23.3
6.22	1.81	1.2E19	-30.7

Reference [29] documents that the elastic modulus actually decreased as the burnup increased. The document gives no explanation for why this could be the case. Typically, materials become more brittle in radiation environments. The burnup in the ACRR is ~60% of the first reported change in burnup reported in

Table 3.4. Again, by linearly interpolating, it can be estimated that the ACRR fuel has experienced a 14% reduction in modulus of elasticity. At the current rate of burnup in the ACRR the reactor will be able to operate for another 70 years before it experiences a 31% reduction in the modulus.

3.4 Effect on Thermal Conductivity

Reference [29] also documents the change in thermal resistivity with respect to burnup. Thermal resistivity is defined as the inverse of thermal conductivity. Table 3.5 reports the resistivity change with respect to burnup and shows that the resistivity increases

by a factor of 5 by 7.03E18 fissions/cm^3 which means that the thermal conductivity decreased by a factor of 5. This increase in resistivity of the fuel is likely due to the introduction of fission products and impurities due to transmutation into the matrix of the fuel. Fission products such as Kr and Xe have significantly lower thermal conductivities than the BeO matrix so their introduction would increase the thermal resistance of the fuel.

Table 3.5: Change of resistivity with respect to burnup [29].

Burnup (Fissions/cm^3)	Resistivity Ratio ($R_{irradiated}/R_{unirradiated}$)
3.45E18	Not reported
7.03E18	5.54
1.2E19	6.16

Using the information in Table 3.5, at the current burnup, it is estimated that the thermal conductivity has decreased by a factor of 3.5. The reactor will be able to operate for another 70 years before the thermal conductivity is reduced by a factor of 6.16.

3.5 Gaseous Fission Products Produced

Most of the fission products are retained by the BeO matrix. However, some of the fission products, such as Kr and Xe, escape the matrix and enter the He filled gaps of the fuel elements [30]. The introduction of Kr and Xe into the gap would lower the thermal conductivity of the gaps and impede heat transfer. The birth rates of the stable isotopes in units of percent per fission of Kr and Xe are shown in Table 3.6. The unstable radioactive isotopes are assumed to decay therefore having no negative impact on the thermal

conductivity of the fuel elements. As Table 3.6 shows, Xe is produced at a significantly

higher rate than the Kr.

Table 3.6: Probability of fission gas atom per fission.

	U235	U238	Pu239
Kr83	0.531	0.406	0.295
Kr84	0.986	0.751	0.478
Kr85	0.288	0.231	0.13
Kr86	1.951	1.194	0.758
Xe131	2.835	3.295	3.745
Xe132	4.217	5.096	5.275
Xe134	7.681	7.092	7.448
Xe136	6.273	6.183	6.627

Because Xe is produced at a much higher rate than Kr, it was assumed that the

contributions due to Kr are negligible. Under this assumption Eqn. 3.1 was used to calculate

the thermal conductivity of the two-gas mixture of Xe and He in the gaps of the fuel

element [12]. The constants k_{He} and k_{Xe}, in Eqn. 3.1 are the thermal conductivities of He

and Xe respectively. The constant x_{he} is the molar ratio of He.

$$k=k_{He}^{x_{He}}*k_{Xe}^{1-x_{He}}$$

Eqn. 3.1

Figure 3.1 shows the thermal conductivities of the gas gaps in the ACRR assuming that all

of the Xe is released into the gaps of the fuel elements and is diffused equally throughout

the elements. It shows the thermal conductivity of the gaps at the current burnup and at

double the current burnup. As Figure 3.1 shows, the release of the fission gasses into the

gap would reduce the thermal conductivity of the gap by nearly 33%.
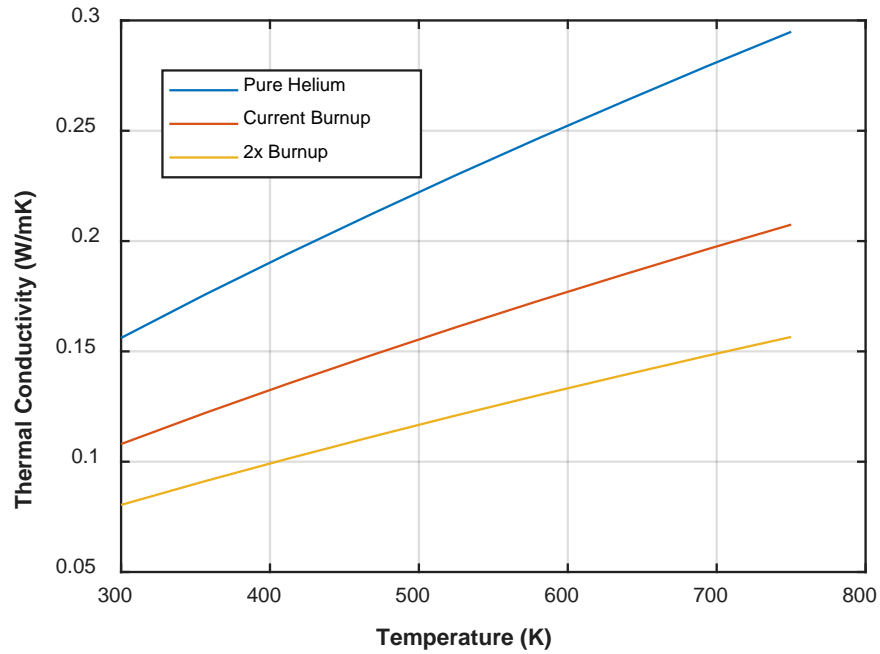
Figure 3.1: Effect of fission gas release on the thermal conductivity of gaps.

3.6 Gaseous Fission Products Released

If the fission products are totally released into the gap the thermal conductivity would be significantly impacted, however fine particle BeO fuels have been found to have excellent gas retention. A study on fission gas release in UO_2-BeO fuel was performed in Australia's HIFAR reactor where the fuel was irradiated in a thermal flux at temperatures ranging from 600°C-800°C for 3550 hours resulting in a burnup of 1.4E20 fissions/cm^3 [30]. The study found that the BeO fuel has a fission gas release rate of approximately 0.5%. A study performed at Oak Ridge corroborated the findings when 30 v/o UO_2 cold pressed and sintered fuel was irradiated at temperatures ranging from 1000°C-1200°C for

120 days resulting in a burnup 3E20 fissions/cm^3 [31]. A release rate of 0.5% would result in a negligible change in gap conduction.

3.7 Swelling

The buildup of fission products, transmutations, and destruction of lattice structures in the fuel pellets causes a volumetric change in the material called swelling. Swelling with respect to burnup was documented in reference [28] and is displayed in Table 3.7. See Section 3.2 for a summary of the experiment. The percent changes in volume, which are reported in Table 3.7, were interpreted as being the change in volume compared to the previous measurement.

Table 3.7: Swelling caused by the burnup.

Burnup (fissions/ cm^3)	Fast Neutron Dose (neutrons/cm^2)	Mean Percent Volume Change Observed (%)
2.06E19	3.6E20	1.77
2.19E19	4.0e20	1.18
2.37E19	4.5e20	0.97

By linearly interpolating, it can be assumed that there has been a volume increase of 0.37%. After another 150 years of operation, the change in volume would approximately be 3.92%.

3.8 Summary

The effects of burnup and radiation damage are dependent on the microstructure of the fuel pellets. Because the burnup effects were never quantified for the ACRR fuel, property changes were estimated using literature on the effects of burnup in similar fuels. These are estimations and are subject to a high degree of uncertainty. These estimations do not account for the fact that many of the radiation and burnup effects can be annealed out at high temperatures, at which the ACRR regularly operates. Because the effects of annealing are not accounted for, these estimations are conservative. Table 3.8 summarizes the estimated effects of burnup on the properties of the fuel in the ACRR. These effects were estimated assuming a burnup of 4.4E18 fissions/cm^3.

Table 3.8: Summary of burnup and radiation effects.

Property	Percent Change in Property (%)
Strength	-1.5
Modulus of Elasticity	-14
Thermal Conductivity	-70
Gap Thermal Conductivity	Negligible
Change in Volume	0.37

4   FUEL ELEMENT PROPERTIES

No documents have been found that show that traditional materials testing was ever performed on the ACRR's fuel pellets. Along with the absence of documentation, there was no consistency in the material properties used in the previous work. Because of the inconsistency of the properties used for the fuel pellets, the properties were derived using material models for this analysis. The following sections document the material properties of the fuel pellets that were derived along with the material properties that were used in both Tills' and Wright's work. Also, the material properties of the He, SS, and Nb are documented. Finally, the change in material properties due to burnup are accounted for in this chapter. The properties for the He assumed that the He is at a pressure of 2 atm. Also, all the data is valid from 296 K to 1673 K.

4.1 Density

4.1.1 UO_2-BeO

The density of fresh UO_2-BeO fuel is approximately 3550 kg/m^3 and is thoroughly documented in quality assurance documentation that can be found the TAV technical library. Table 4.1 compares the densities that were used in Tills' and Wright's reports.

Table 4.1: Density of the ACRR's fuel pellets [6], [22] .

Pelfrey (kg/m^3)	Tills (kg/m^3)	Wright (kg/m^3)
3550 kg/m^3	Not Documented	3500 kg/m^3

4.1.2 Other Materials

The densities of the He, Nb and SS are included in Table 4.2. The densities are at room temperature.

Table 4.2: Densities of He, Nb, and SS and their sources.

Material	Density (kg/m^3)	Source
He	0.3206	[32]
Nb	8590	[33]
SS	7750	[33]

4.2 Modulus of Elasticity

4.2.1 UO$_2$-BeO

The modulus of elasticity of the UO$_2$-BeO fuel was estimated using a Voigt-Reuss-Hill approximation. This approximation averages the Voigt approximation which is the upper bound of a composite's elastic modulus and the Reuss approximation which is the lower bound [34]. The moduli of elasticity for the UO$_2$ and BeO were documented in references [35] and [36] respectively. A power series model was fit to the modulus of elasticity with T being the temperature in K. The equation is given in Eqn. 4.1.

$$E(T)=-41.38*T^{2.879}+3.396E11 \ (Pa)$$
Eqn. 4.1

Table 4.3 compares the approximate elastic modulus to the elastic moduli that were used in Tills' and Wright's work at temperatures of 23°C and 1000°C.

Table 4.3: Modulus of elasticity at 23°C and 1000°C of the ACRR's fuel pellet [6], [24], [25].

Temperature (°C)	Pelfrey (GPa)	Tills (GPa)	Wright (GPa)
23	339.3	338.9	378
1000	303.6	317.5	341

4.3 Thermal Conductivity

4.3.1 UO₂-BeO

Maxwell's analytical solution for effective conductivity of a heterogenic medium was used to calculate the effective thermal conductivity of the composite. Maxwell's solution assumes there is no thermal interaction between the particles so it is only valid for composites with small dispersion volume fractions [37]. The UO₂-BeO fuel has a volume fraction of 6.9% and 1 µm particles so the model is valid for the fuel. The thermal conductivity for UO₂ and BeO were selected from references [35] and [38] respectively. Maxwell's solution is shown in Eqn. 4.2 and a power law fit for the data is shown in Eqn. 4.3, where k_{eff} is the effective thermal conductivity of the composite, k_p is the thermal conductivity of the particulate, k_m is the thermal conductivity of the matrix, V_p is the volume fraction of the particulate, and T is the temperature in K.

$$k_{eff}=k_m\left[1+\frac{3V_p}{\frac{k_p+2k_m}{2(k_p-k_m)}-V_p}\right] \text{ (W/m-K)} \qquad \text{Eqn. 4.2}$$

$$k(T)=2.902E6*T^{-1.636} \text{ (W/m-K)} \qquad \text{Eqn. 4.3}$$

Table 4.4 compares the thermal conductivities of the fresh fuel cited in this report, and the

thermal conductivities documented in both Tills' and Wright's reports.

Table 4.4: Thermal conductivity at 23°C and 1000°C of the ACRR's fuel pellets [6], [24], [25].

Temperature (°C)	Pelfrey (W/m-K)	Tills (W/m-K)	Wright (W/m-K)
23	250.6	~221.9	~65
1000	35.47	~73.269	~10

4.3.2 Other Materials

The thermal conductivities of the other materials are shown in Table 4.5 The data

for He and Nb were tabulated so a curve was fit to the data. The variable T is temperature

in K.

Table 4.5: Thermal conductivities of He, Nb, and SS and their sources.

Material	Thermal Conductivity (W/m-K)	Source
He	$k(T)=0.002913*T^{0.6977}$	[32]
Nb	$k(T) = 0.0001531*T + 0.4909$	[39]
SS	15.1	[33]

4.4 Coefficient of Thermal Expansion

4.4.1 UO₂-BeO

The coefficient of thermal expansion (CTE) for the UO_2-BeO was approximated

using a "refined" rule of mixtures [40]. The rule of mixtures is refined by accounting for

the thermal stresses that occur between the matrix and the particles. The formula is shown

in Eqn. 4.4 and 4.5. A polynomial fit to the derived CTE of the UO_2-BeO with respect to temperature is shown in Eqn. 4.6. The temperature dependent thermal expansion of the BeO and UO_2 were from references [41] and [35], respectively. The Poisson's ratio of BeO and UO_2 were from references [42] and [12], respectively. The variables in the equations are as follows: α_{eff} is the effective CTE of the composite, α_m is the CTE of the matrix, α_p is the CTE of the particle, V_p is the volume fraction of the particle, V_m is the volume fraction of the matrix, θ is the refinement factor, v_m is the Poisson's ration of the matrix, and T is the temperature in K.

$$\alpha_{eff}=\alpha_m-V_p\theta\left(\alpha_m-\alpha_p\right) \ (1/K) \qquad \text{Eqn. 4.4}$$

$$\theta=\frac{3E_p(1-v_m)}{\left[(1+v_m)+2V_p(1-2v_m)\right]E_p+2V_mE_m(1-v_m)} \qquad \text{Eqn. 4.5}$$

$$\alpha(T)=-1.01E\text{-}12*T^2+5.15E\text{-}9*T+5.192E\text{-}6 \ (1/K) \qquad \text{Eqn. 4.6}$$

Table 4.6 is a comparison of the coefficient of thermal expansion from the other analyses.

Table 4.6: Coefficients of thermal expansion at 23°C and 1000°C of the ACRR's fuel pellets [6], [24], [25].

Temperature (°C)	Pelfrey (1E-6/K)	Tills (1E-6/K)	Wright (1E-6/K)
23	6.66	6.4557	8
1000	9.33	9.67	8

4.4.2 Other Materials

The CTE of the other materials are shown in Table 4.7. The original Nb data was originally tabulated so a curve was fit to the data. The variable T is temperature in K. The CTE of He is not documented because it is a gas.

Table 4.7: Coefficients of thermal expansion of Nb and SS and their sources.

Material	Thermal Expansion (1/K)	Source
Nb	$\alpha(T)=-8.284E\text{-}8T^2+7.761E\text{-}7T+8.476E\text{-}6$	[39]
SS	$\alpha=1.7E\text{-}5$	[33]

4.5 Specific Heat

4.5.1 UO$_2$-BeO

The specific heat of the UO$_2$-BeO was calculated using the rule of mixtures as is shown in Eqn. 4.7. The temperature dependent specific heat of the UO$_2$-BeO is represented by the sixth order polynomial shown in Eqn. 4.8. The specific heats of BeO and UO$_2$ were found in references [41] and [35] respectively. The variables are as follows: C_{eff} is the effective specific heat of the composite, V_m is the volume fraction of the matrix, C_m is the specific heat of the matrix, V_p is the volume fraction of the particulate, C_p is the specific heat of the particulate, and T is the temperature in K.

$$C_{eff}=V_mC_m+V_pC_p \ (\frac{J}{kg\text{-}K}) \qquad \text{Eqn. 4.7}$$

$$C_{eff}(T)=1.11e\text{-}15*T^66+8.84e\text{-}12*T^5-2.75e\text{-}08*T^4+$$
$$4.31e\text{-}05*T^3-0.036*T^2+16.68*T-1706 \ (\frac{J}{kg\text{-}K}) \qquad \text{Eqn. 4.8}$$

4.5.2 Other Materials

The specific heats of the other materials are shown in Table 4.8. The specific heat of Nb was originally tabulated so a curve was fit to the data. The variable T is temperature in K. The specific heat of the He at a constant volume was used because the volume of the fuel element is constant.

Table 4.8: Specific heat of He, Nb and SS and their sources.

Material	Specific Heat (J/kg-K)	Source
He	3116	[32]
Nb	$C_p(T) = 9.813T^2 + 0.0711T + 260.9$	[39]
SS	480	[33]

4.6 Fracture Strength

The fracture strength of many ceramics, and brittle materials in general, is a stochastic property that depends on the specimen's porosity, density, grain size, constituent materials, and flaw size. Even specimens with identical manufacturing processes can have a large degree of variability in the fracture strength. For these reasons, declaring the fracture strength of the UO_2-BeO fuel, without properly performing tests to determine it, is improper. Only very qualitative estimates can be made without proper testing.

Because the fracture strength of the fuel pellets was never tested, previous work resorted to calculating the stresses that the fuel experienced during in-pile experiments. This method had the fundamental assumption that the fracture during the in-pile

experiments was a result of the temperature profile caused by the fission distribution. Wright calculated the thermal stresses by using temperature profiles that can be found in the ACPR quarterly reports and using them to calculate the thermal stresses of the in-pile experiments using an analytical solution. Tills' used the energy deposition profile to calculate the temperature profile in the peak fuel pellet during a pulse and then used the finite element method to calculate the thermal stresses. The same approach that was used by both Tills and Wright was used in this work to approximate the thermal stresses experienced by the pellets during the in-pile testing. Both Tills and Wright provided enough information in their reports to recreate the estimated temperature profiles from the fission distribution experienced by the fuel during the in-pile experiments. Sections 4.6.1-4.6.3 describe the geometry, thermal loads, and structural constraints used as inputs to calculate the thermal stresses of the in-pile experiments.

4.6.1 Thermal Loads

4.6.1.1 Tills

The details of the experiments and the analyses are included in Chapter 2. In Tills' report, he provides the energy deposition per mass of the fuel pellet and the radial energy deposition profile of the two experiments. For the smaller of the two pulses, which no pellets fractured, it was estimated that the average energy deposition was 364 cal/g. For the larger pulse, which 25% of the pellets did fracture, it was estimated that the average energy deposition was 429.4 cal/g. For both pulses the peak to average radial energy deposition is shown in Eqn. 4.9.

$$\text{Peak/Avg} = 0.79985971 + .34048928r - 1.2141774r^2$$
$$+1.939536r^3 - 1.2757009r^4 + .32146363r^5$$

<div align="right">Eqn. 4.9</div>

The in-pile experiment was simulated by first determining how much energy was deposited into each fuel pellet. The mass of the one half of an outer annulus is 5.64 g so the amount of energy deposited during the small and large pulse was 8590 J and 10133 J, respectively. It was assumed that the energy was deposited over a 6 ms period, which is a typical full-width half-max in the ACRR. The energy was deposited in the fuel pellet in accordance with the fission distribution profile in Eqn. 4.9. It was assumed that there was no heat loss from the fuel pellet, so no other thermal loads or boundary conditions were applied.

4.6.1.2 Wright

In Wright's report, he recorded the approximate maximum radial temperature profile in the outer annulus of a fuel pellet for both the small and larger pulse [43]. The temperature profile for the 1150°C and 1410°C experiments are shown in Eqn. 4.10 and Eqn. 4.11, respectively, where r is the radial distance in cm. No thermal simulation was necessary because temperature profiles can be applied directly to structural analyses in ANSYS Mechanical 19.2.

$$T(r) = 1150 \left[0.5004 + 0.0187 \exp\left(\frac{r}{0.4997}\right) \right]$$

<div align="right">Eqn. 4.10</div>

$$T(r)=1410\left[0.4928+0.008058* \exp\left(\frac{r}{0.3962}\right)\right] \qquad \text{Eqn. 4.11}$$

4.6.2 Model and Constraints

The model was simply constrained using a weak-spring condition available in ANSYS Mechanical [44]. The weak-spring condition applies spring-like loads to each surface of the geometry which resists movement of the model without causing non-physical stresses. The weak-spring condition made it so the only stresses the fuel pellet experienced were those from the temperature gradient. Figure 4.1 and 4.2 show the top and side views of the meshed geometry used to calculate the thermal stresses.
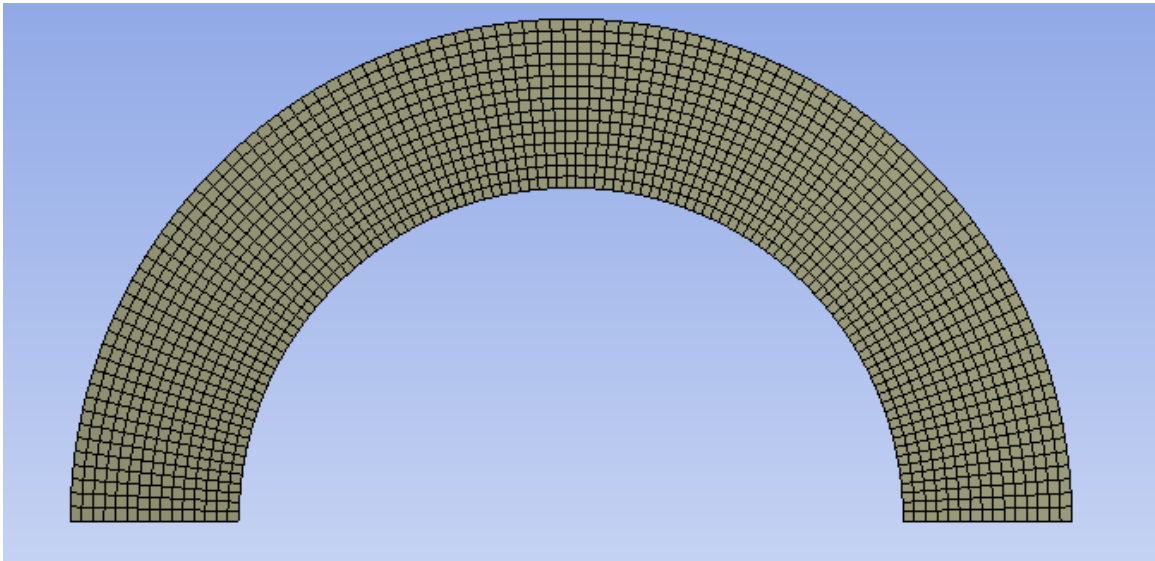
Figure 4.1: Top view of the meshed geometry used to estimate the stresses of the fuel pellets during in-pile experiments.
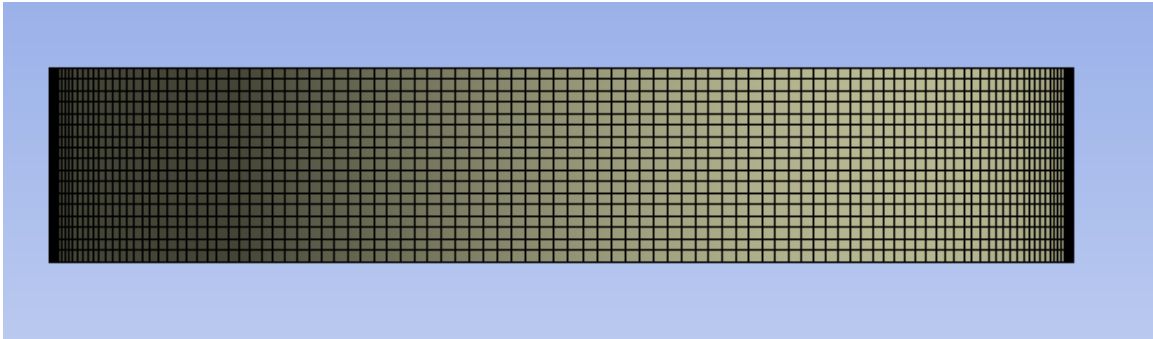
Figure 4.2: Side view of the meshed geometry used to estimate the stresses of the fuel pellets during in-pile experiments.

4.6.3 Results

Figure 4.3 and 4.4 show representative temperature and stress contour plots for these analyses. Although the magnitude of the temperatures varied between the analyses, similar temperature profiles were present. Each experiment had the highest temperature at the outer surface of the fuel and the lowest temperature on the inner surface. These results are consistent with what would be expected seeing more energy is generated in the outer region than in the inner region. Figure 4.4 shows the stress profile induced by the temperature profile shown in Figure 4.3. The stress contours were also similar in each analysis except the magnitudes of the stresses varied. Figure 4.4 shows that the maximum stresses occur near the radial center of the fuel pellet. This is because the outer region of the fuel is hotter thus it experiences larger thermal expansions that compete with the lesser thermal expansions of the middle region. The competition of stresses results in tensile stresses in the middle region and compressive stresses in the outer region.
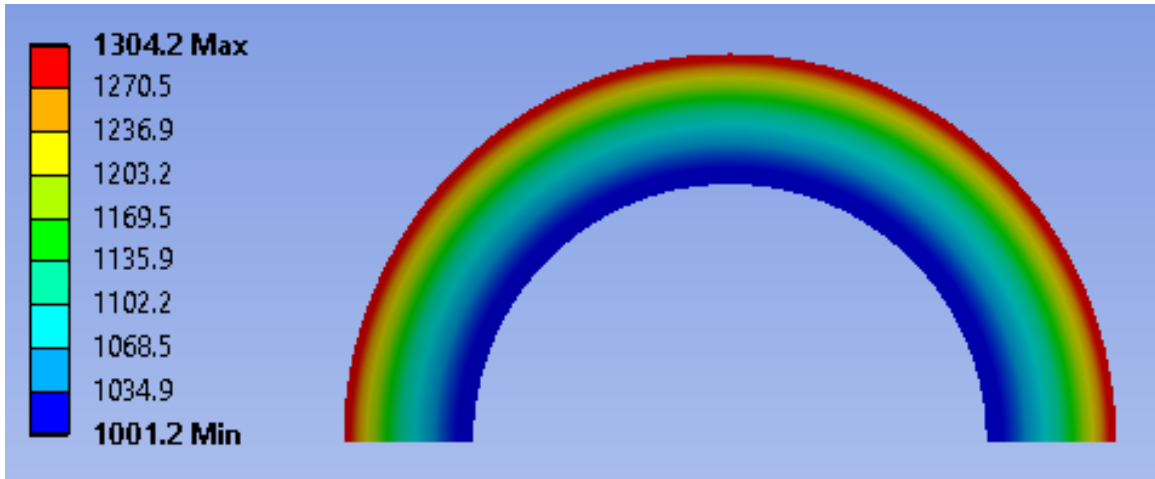
Figure 4.3: Temperature (°C) contour plot for 429.4 cal/g experiment in Tills' report.
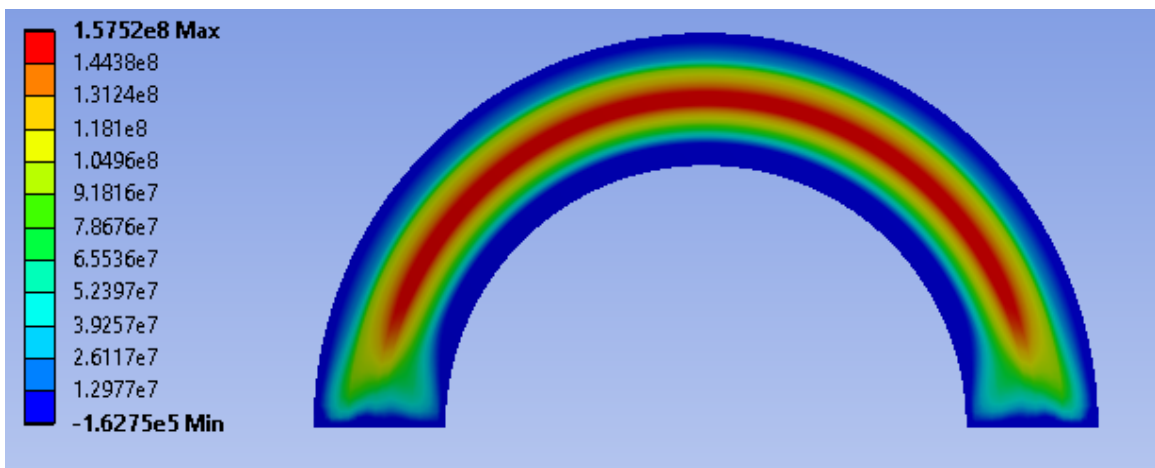
Figure 4.4: Stress (Pa) contour plot for 429.4 cal/g experiment in Tills' report.

Table 4.9 summarizes the experiments, the findings of both Tills and Wright, and the findings of this analysis. The first row of Table 4.9 shows the different experiments performed. The second row shows the approximate maximum temperature of fuel in the experiments. The third row shows the thermal stresses that were calculated by Tills' and Wright. The fourth row reports the thermal stresses calculated in this analysis. Finally, the

last row shows how many pellets fractured in each experiment. The stresses calculated in this work varied by as much as 85% from the original calculations in Tills' and Wright's work. This is likely because this analysis included different material properties, a temperature dependent modulus of elasticity, and a temperature dependent CTE. From this analysis it can be estimated that 75% of fresh pellets survive stresses of 153.5 MPa while 40% can survive stresses over 271.4 MPa. This demonstrates the variability of fracture strength previously discussed. Stresses below 134.7 MPa should not cause fracture in the fresh fuel pellets.

Table 4.9: Summary of the in-pile fuel pellet experiments, analyses, and results.

	Tills		Wright	
Experiment	364 cal/g	429.4 cal/g	1150°C	1410°C
Max Experimental Temperature ($^\circ$C)	1182.9	1340	1189.8	1491.7
Reported Thermal Stresses	74 MPa (10.8 ksi)	88 MPa (12.8 ksi)	68 MPa (9.98 ksi)	108.9 MPa (15.8 ksi)
Pelfrey's Thermal Stresses	134.7 MPa (19.53 ksi)	153.5 MPa (22.2 ksi)	174.0 MPa (25.2 ksi)	271.4 MPa (39.4 ksi)
# of Pellets Fractured	0/40	10/40	2/8 @ 101 Pulses	6/10 @ 71 Pulses

4.7 Accounting for Burnup

The material properties documented in Sections 4.1-4.6 are those of the fresh fuel, however, the ACRR has experienced burnup so the material properties were adjusted to account for the damage induced by burnup and radiation effects. The material properties were adjusted by scaling them using the percent change discussed in Chapter 3.

4.7.1 Density

Section 3.7 documents the swelling of the fuel due to burnup. The swelling results in an increase in volume and a decrease in density. It was estimated that the volume has increased by 0.37% which would result in a density of 3537 kg/m^3. Although the density was adjusted to account for swelling, the effects swelling had on the dimensions of the pellet were neglected. Equation 4.12 shows the equation used to calculate the density.

$$\rho_{burnup}=\rho_{fresh}*(1+\Delta V) \ (kg/m^3) \qquad\qquad \text{Eqn. 4.12}$$

4.7.2 Modulus of Elasticity

The modulus of elasticity has decreased by approximately 14%. The 14% change was accounted for in the modulus of elasticity by simply scaling the fresh modulus. Equation 4.13 shows the power fit representing the modulus of elasticity of the fuel with burnup.

$$E(T)=-34.76*T^{2.879}+2.853E11 \ (Pa) \qquad\qquad \text{Eqn. 4.13}$$

4.7.3 Thermal Conductivity

The effect of the burnup on thermal conductivity was accounted for by scaling the thermal conductivity to represent the 70% decrease in thermal conductivity. Equation 4.14 represents the current thermal conductivity of the ACRR fuel.

$$k(T)=8.5353E6*T^{-1.636} \text{ (W/m-K)} \hspace{4cm} \text{Eqn. 4.14}$$

4.7.4 Fracture Strength

Applying the modest decrease of 1.5% that the burnup has on the fuel strength, the 25% of the ACRR fuel could fracture at stresses as low as 150.1 MPa and 60% could fracture at stresses as low as 266.9 MPa.

5 THERMAL STRESSES DURING A MAXIMUM PULSE OPERATION

5.1 Process

Using the material properties documented in Chapters 3 and 4, both transient thermal and transient structural analyses were performed to simulate a maximum pulse in the ACRR. The power profile and outer cladding temperature used in the transient thermal analysis were calculated using a SNL code named RAZORBACK. The results of the transient thermal calculation were imported into a transient structural simulation and the gradient induced thermal stresses were calculated. Both the transient thermal and transient structural simulations were performed using ANSYS Workbench 19.2.

5.2 RAZORBACK Simulation

Although the boundary conditions of the transient thermal analysis could have been derived from reactor diagnostics, calculating them using RAZORBACK was a more direct method with less uncertainties. RAZORBACK is a code developed at SNL by Darren Talley that simulates research reactors by coupling reactor kinetics, conductive heat transfer, and thermal hydraulics [38]–[41]. The code has undergone extensive verification and validation and has demonstrated the ability to accurately simulate pulses in the ACRR. When using RAZORBACK to simulate pulse operations in the ACRR, the user is able to specify the various transient rod related parameters such as the transient rod start position and rod hold up time. These parameters control the reactivity insertion of the ACRR which

determines the pulse parameters. By adjusting the transient rod start position and transient rod hold up time, a maximum pulse was simulated using RAZORBACK. Operation 11330, which had the largest calculated peak system reactivity since 2003, was modeled [49]. When simulating a pulse, RAZORBACK calculates the reactor power and outer cladding temperature. The reactor power and cladding temperatures were used in the transient thermal analysis. Figure 5.1 shows the reactor power and total energy generated with respect to time. As Figure 5.1 shows, the reactor power reached 52,000 MW and a total energy deposition of 388 MJ. The calculated maximum power of the reactor was higher than the power that was recorded by the ACRR's plant protection system, so this analysis represents a very conservative case for a maximum pulse operation in the ACRR. Figure 5.2 shows the calculated outer cladding temperature for this operation. From the simulation, it was calculated that the cladding would reach a maximum temperature of 135°C. At a time of ~2.7 seconds, Figure 5.2 shows a dip in the cladding temperature which is the result of increased heat transfer due to boiling.
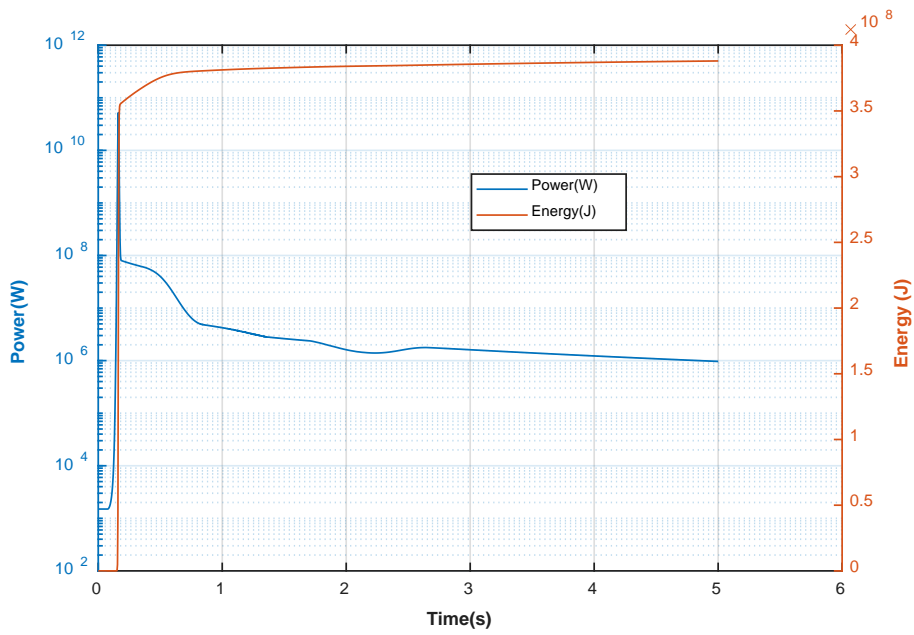
Figure 5.1: Power profile and total energy of a \$3.16 pulse.
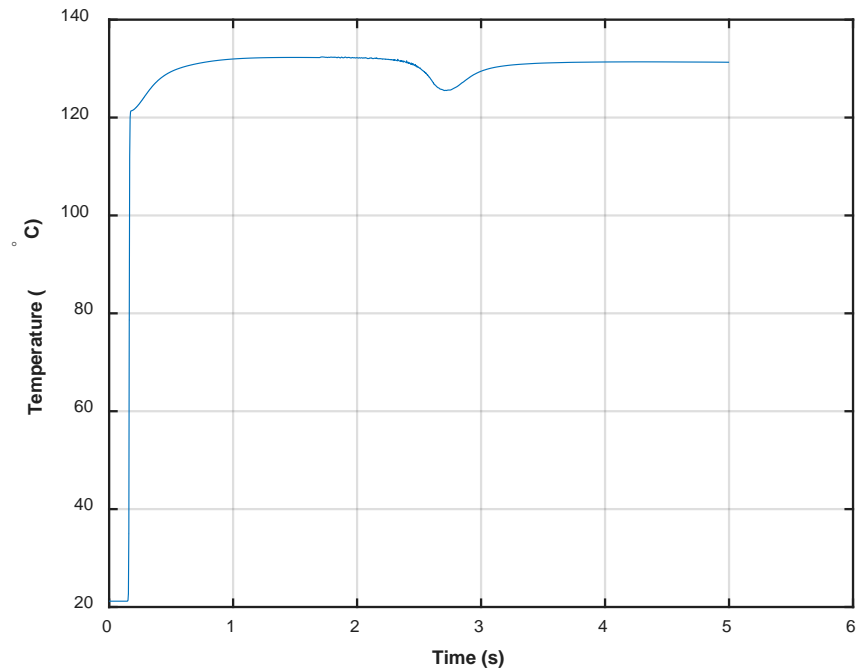
Figure 5.2: Temperature of the outer surface of the cladding during a \$3.16 pulse.

5.3 Transient Thermal Analysis

5.3.1 Geometry and Finite Element Model

Ideally, simulations would be performed on the entire fuel element, however the computational cost would be extremely large. The geometry used to perform the FEA analysis was reduced to the height of one fuel pellet (0.25 in). The model was also split, and a planar symmetry condition was applied to the fuel to reduce the computational cost further. Figure 5.3 shows the geometry used for the analysis from the top plane and Figure 5.4 shows the geometry from the front plane where the symmetry condition was applied. Reducing the model to one pellet assumes that the effects of axial heat transfer are negligible. Although this is not strictly true, the rate of axial heat transfer is dwarfed by the radial heat transfer because the temperature difference produced by the axial fission profile is small compared to the temperature difference between the fuel and the water.
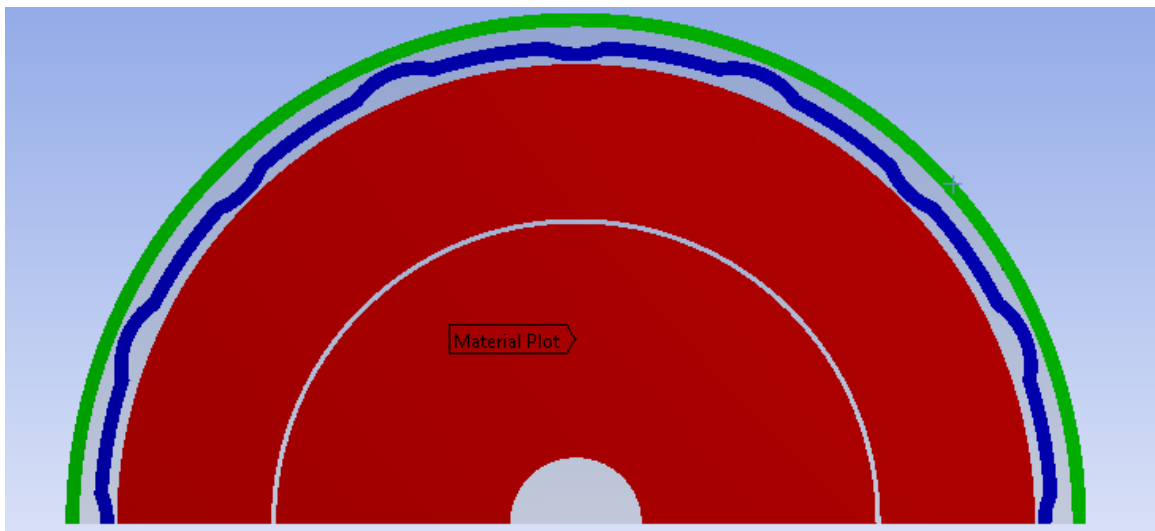
Figure 5.3: Computational geometry from the top plane for the transient thermal analysis.
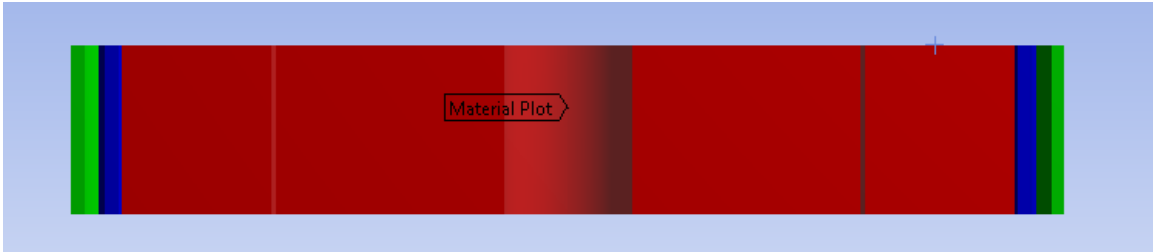
Figure 5.4: Computational geometry from the front plane for the transient thermal analysis.

The top and side views of the meshed geometries can be found in Figure 5.5 and Figure 5.6, respectively. The mesh convergence study can be found in Appendix A.
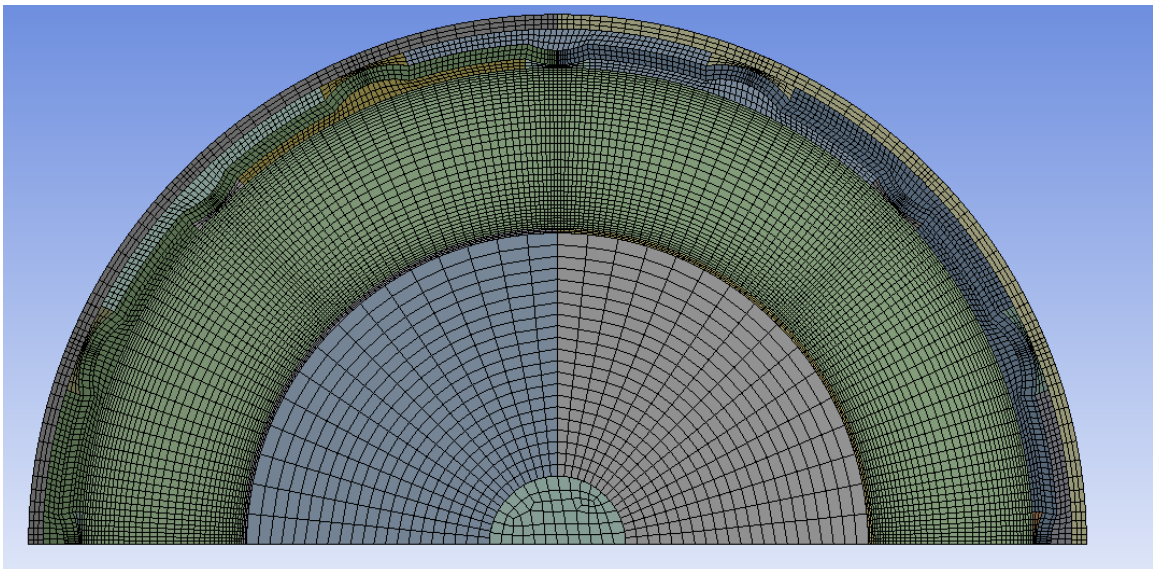
Figure 5.5: Top view of the meshed geometry used for the transient thermal analysis.
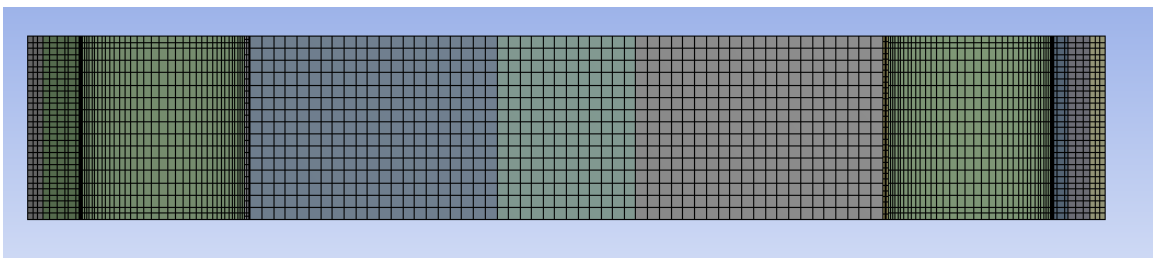
Figure 5.6: Side view of the meshed geometry used for the transient thermal analysis.

46

5.3.2 Simulation

Sections 5.3.2.1-5.3.2.6 document the loads and boundary conditions used to simulate a maximum pulse in the ACRR. These loads and boundary conditions directly affect heat transfer in the fuel pellet and thus the thermal stresses.

5.3.2.1 Internal Heat Generation

Internal heat generation is a body load available in ANSYS Mechanical 19.2 that allows users to apply a volumetric heating load to a body. In this analysis, the internal heat generation load was used to model the heat generated in the fuel pellets and energy deposited in the Nb can. The transient reactor power, calculated using RAZORBACK, was used to determine the average amount of energy generated per cubic centimeter of fuel in the ACRR. To do this, the reactor power was simply divided by the total volume of the fuel in the ACRR to determine the average heat generation per unit volume. The average heat generation was scaled to represent the peak volumetric heat generation that occurs at the axial centerline in the peak element in the ACRR. The heat generation was then made radially dependent by scaling it using the peak radial fission profile determined using MCNP6. The MCNP calculation was performed by Curtis Peters of SNL. The heat generation was scaled to model a fuel element in the second row of the reactor, next to one of the transient rods, which is where the peak heat generation occurs (See Appendix B for a layout of the reactor). The amount of energy deposited in the Nb can was also calculated by Curtis Peters of SNL. He calculated that 1.45e4 rad/MJ of reactor energy is deposited in the Nb. Using the energy deposition ratio, the reactor power was scaled to model the

47

time dependent energy deposition in the Nb can. Table 5.1 shows the axial and core peaking factors that are documented in reference [50] and the fission profile calculated by Curtis Peters. The variable r in the fission profile is the radial position in the fuel pellet in units of cm.

Table 5.1: Peaking factors and pellet radial fission profile in the ACRR.

Axial Peaking Factor (peak/average)	1.24
Core Peaking Factor (peak/average)	1.52
Peak Fission Profile	$F_{peak}(r)=0.7962e^{-0.1299*r}+0.0570e^{1.382*r}$

The internal heat generation condition was applied to both the inner and outer annuli of the fuel pellets. The ANSYS Workbench graphical user interface currently does not support spatially varying internal heat generation so a command snippet was used to impose the condition.

5.3.2.2 Gap Radiation

Because the temperature of the fuel reaches high temperatures (>1000°C), thermal radiation becomes a dominant means of heat transfer. A wall to wall radiation condition was applied to the inner walls of the fuel element to account for thermal radiation. The thermal emissivity of the materials in the fuel elements are shown in Table 5.2.

Table 5.2: Thermal emissivity of SS, UO$_2$-BeO and Nb and their sources.

Material	Emissivity	Source
SS	0.67	[51]
UO$_2$-BeO	0.37	[6]
Nb	0.22	[52]

5.3.2.3 Gap Conduction

The effect of convection in the gap was assumed to be negligible in this analysis. This is the standard assumption when performing heat transfer analyses on fuel elements with small gaps [12]. Because the effects of convection were assumed to be negligible, only conduction through the He is considered.

5.3.2.4 Outer Cladding Temperature

When the ACRR is pulsed, the heat generated in the fuel is ultimately transferred into the water of the pool. The outer cladding temperature is dependent not only on the heat produced in the fuel pellets, but also the rate of convection to the pool. RAZORBACK simulates the heat transfer and convection thus its results for outer cladding temperature were used in this analysis. The outer cladding temperature, plotted with respect to time, is shown in Figure 5.2.

5.3.2.5 Time Stepping

The Fourier Number is commonly used to determine the minimum time-step necessary to accurately capture the physics of a transient thermal simulation [53]. It represents the ratio of heat conduction versus energy storage in a finite element. Fourier's Number is shown in Eqn. 5.1 where k is the thermal conductivity, Δt is the time step, ρ is the density, C is the specific heat and Δx is the thickness of the smallest element.

$$Fo = \frac{4k\Delta t}{\rho C (\Delta x)^2} \qquad \text{Eqn. 5.1}$$

Equation 5.1, when solved for Δt, shows that the minimum time step is proportional to the thickness of the element, the density of the material, and specific heat of the material. Equation 5.1 also shows that Δt is inversely proportional to the thermal conductivity of the material. The He contained in the gaps of the fuel element has the smallest density, specific heat, and thickness thus the He elements were used to determine the time steps. Solving Eqn. 5.1 for Δt, the minimum time step is 1 µs. Using the 1 µs minimum time-step, ANSYS was allowed to automatically adjust the time-step depending on the rate of convergence.

5.3.2.6 Boundary Condition Placement

The boundary conditions incorporated in the analysis were meant to accurately model heat transfer within the fuel elements. The accurate modeling of heat transfer is essential in determining the temperature gradients and thus the thermal stresses in the fuel

pellet. The energy generated by fission and deposited by radiation and fission fragments were modeled as internal heat generation loads. These loads were applied to the fuel pellets to model the energy deposited by neutrons, gamma-rays, and fission fragments. An internal heat generation condition is also applied to the Nb can to model the energy deposited through gamma-rays and neutrons. Thermal radiation conditions were applied in the gaps of the fuel element to model the thermal radiation. The outer cladding temperature was calculated using RAZORBACK and specified for each time step in the simulation. A symmetry boundary condition was applied to reduce the computation time of the simulation. The applied conditions are depicted Figure 5.7.
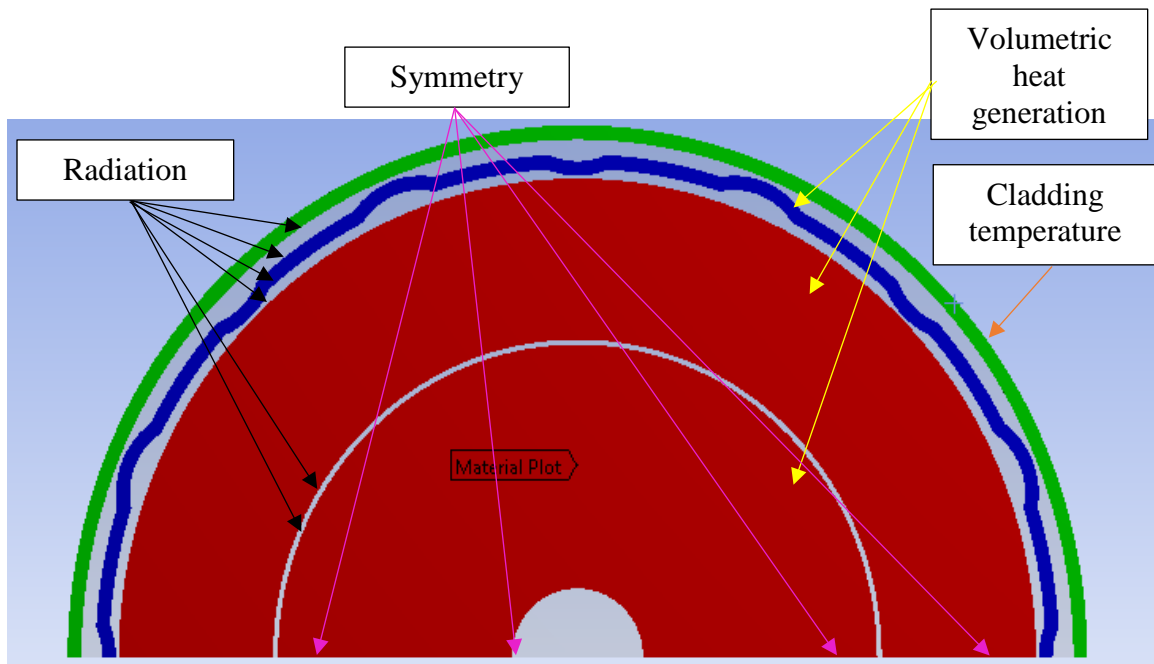

Figure 5.7: Transient thermal simulation boundary conditions.

5.3.3 Results

The results of the transient thermal analysis are shown in Figure 5.8-5.23. Figure 5.8 shows the peak temperature in the fuel element with respect to time. Plotted along with the peak temperature is the reactor power to give context to the temperature at different points in the pulse. Figure 5.8 shows that the maximum temperature occurs immediately after the knee of the pulse. Figure 5.9 shows the peak heat flux in the element with respect to time. Again, reactor power is plotted to give context to heat flux graph. Figure 5.9 shows that the maximum heat flux occurs during the pulse. This makes sense because most of the energy is being introduced into the system during the pulse. The heat flux decreases after the pulse, as the temperature of the fuel and its surroundings begin to equilibrate.
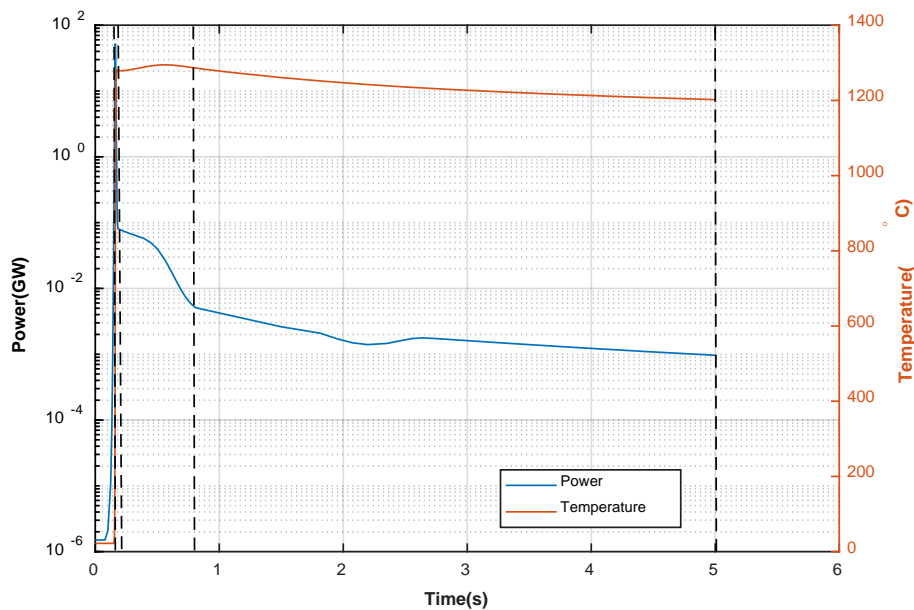
Figure 5.8: Maximum temperature and reactor power vs time.
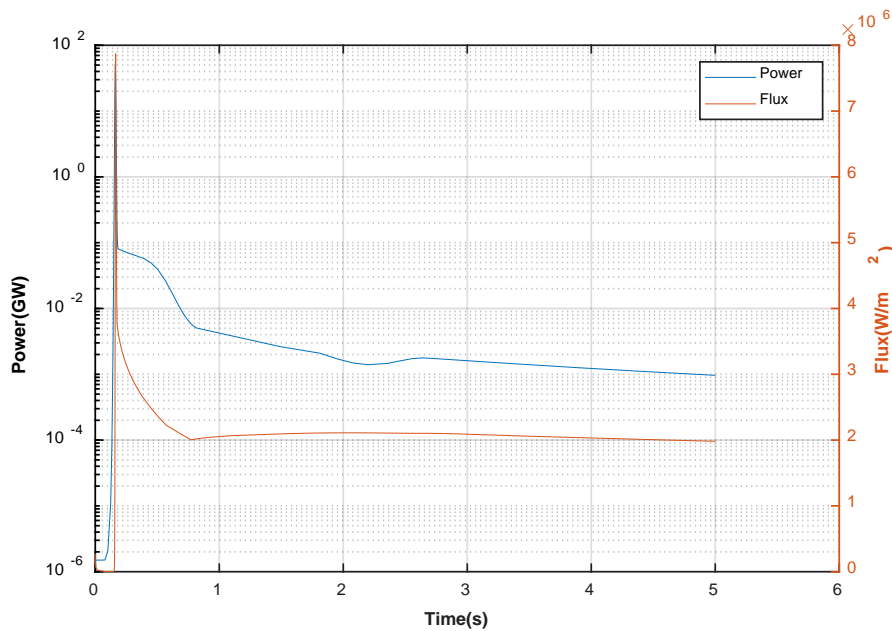
Figure 5.9: Maximum heat flux and reactor power vs time.

Contour plots of the temperature and heat flux in the fuel element are shown at different points in the simulation. The time steps in which these are shown are depicted by the vertical dashed lines in Figure 5.8. Figure 5.10-5.12 show temperature and flux contour plots at the peak of the pulse. Figure 5.10 shows the temperature contour plot of the model at 0.1617 s. It shows that at 0.1617 s some heat has been transferred out of the pellet into the surrounding He, however the outer annulus of the fuel pellet does not show any local cooling. The temperature gradients in the pellet are due to the fission distribution. The highest temperatures occur at the outer edge of the fuel pellet and lowest at the inner edge. This can also clearly be seen in Figure 5.11 which only shows the temperature contour plot of the outer annulus of the fuel pellet. Figure 5.12 shows the heat flux contour plot. This again shows that very little heat is leaving the pellet at this stage.
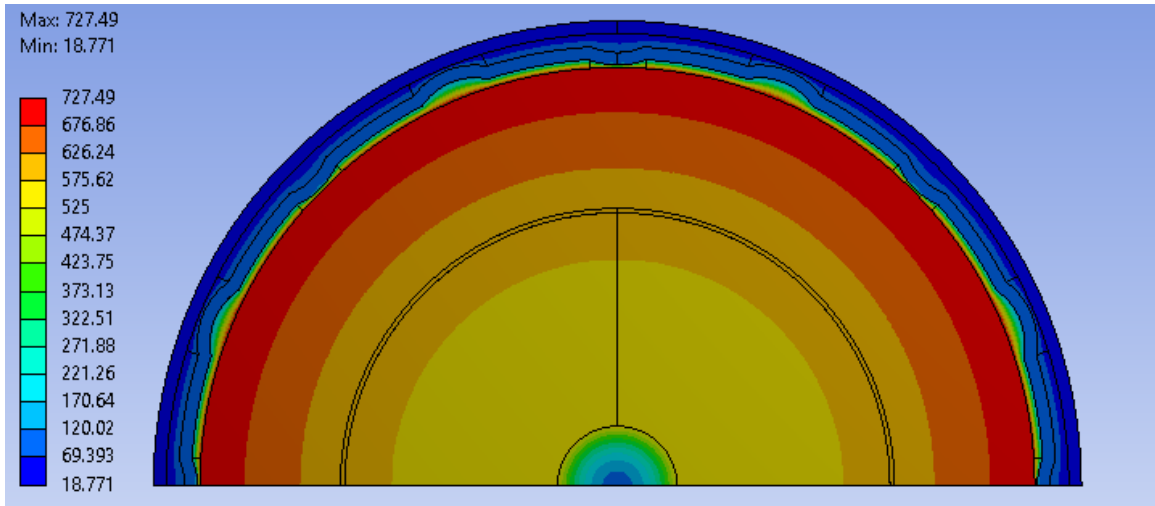
**Figure 5.10: Temperature (°C) contour plot at the peak of the pulse (~0.1617 s).**
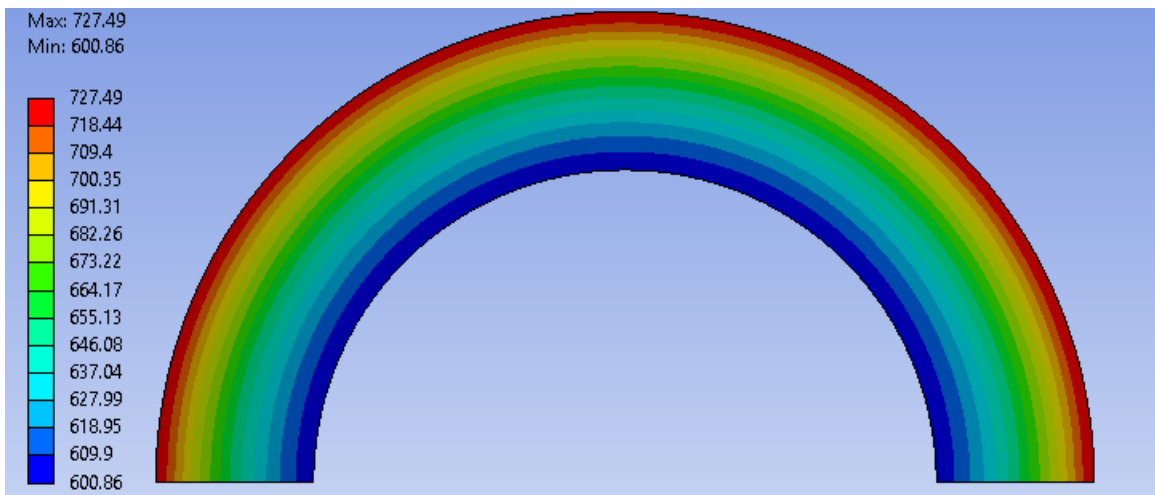
Figure 5.11: Temperature (°C) contour plot of the outer annulus of the fuel pellet at the peak of the pulse (~0.1617 s).

54
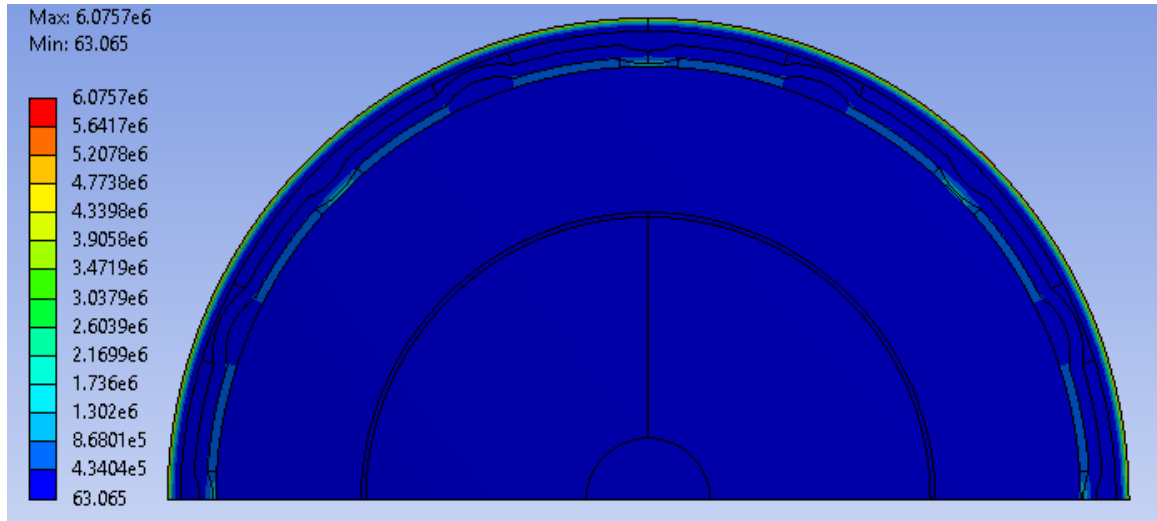
Figure 5.12: Heat flux (W/m^2) contour plot at the knee of the pulse (~0.1617 s).

Figure 5.13-5.15 show the contour plots at 0.18 s. Figure 5.13 shows that the pellet has increased in temperature by over 500°C in the ~0.02 s since the previous set of plots. The temperature distribution shows that heat, at this stage, is beginning to be transferred from the outer annulus of the pellet to the surrounding He with some of it reaching the Nb. Figure 5.14 shows that local cooling of the areas nearest to the Nb fluting is beginning to occur, however the temperature gradient still largely resembles the fission profile. The heat flux contour plot, shown in Figure 5.15, shows the highest heat flux occurs between the Nb fluting and the fuel pellet where the fluting is located. This is because the least He is in these locations.
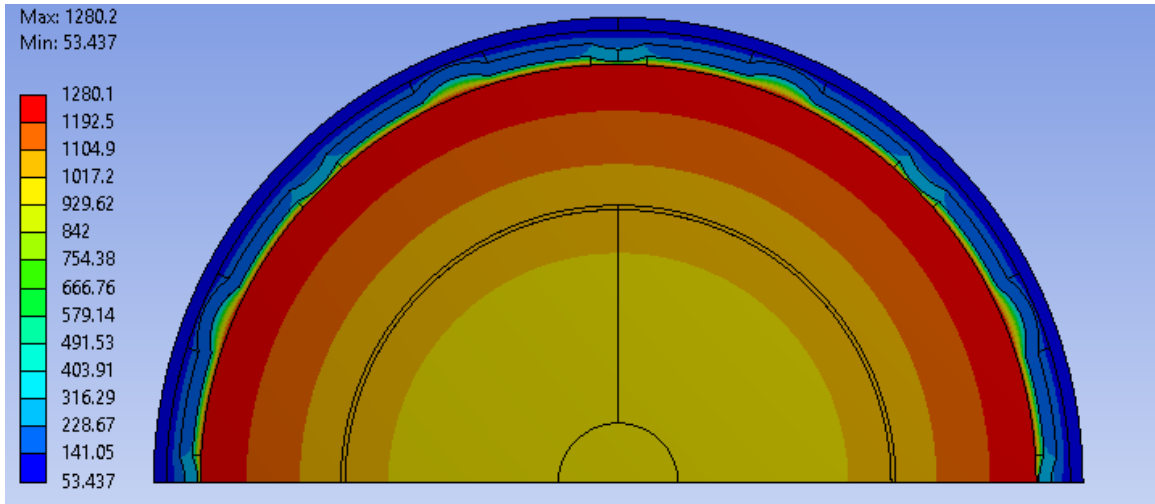
**Figure 5.13: Temperature (°C) contour plot at the peak of the pulse (~0.18 s).**
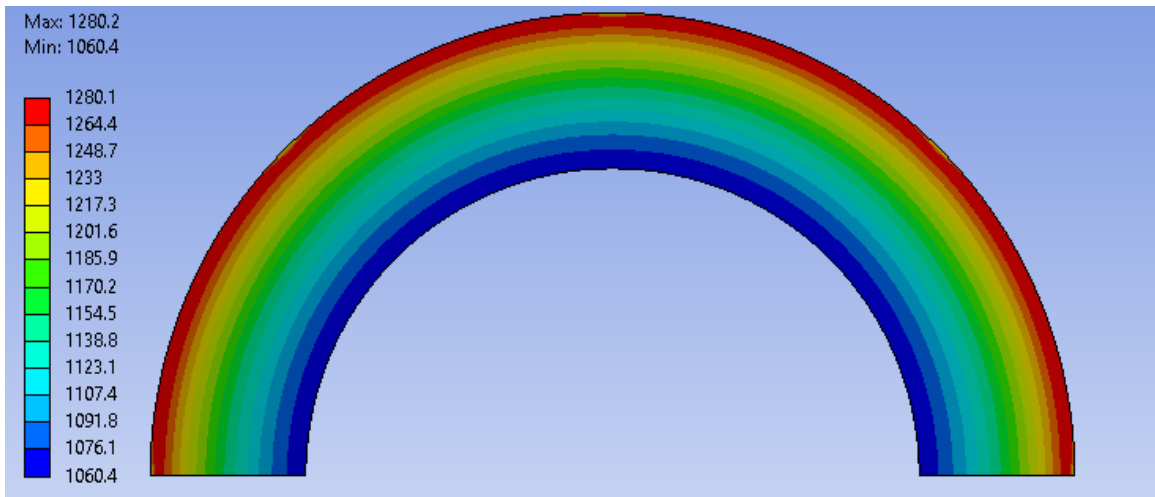
Figure 5.14: Temperature (°C) contour plot of the outer annulus of the fuel pellet at the peak of the pulse (~0.18 s).
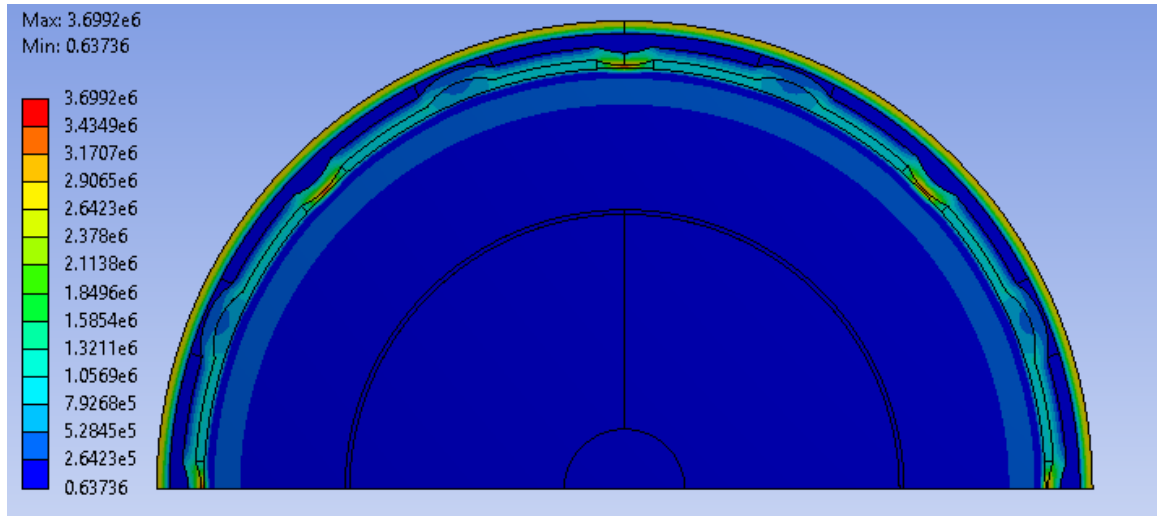
**Figure 5.15: Heat flux (W/m²) contour plot at the peak of the pulse (~0.18 s).**

Figure 5.16-5.18 show that the contour plots at 0.8 s which is right after the knee of the pulse. Figure 5.16 shows both the He and Nb increased in temperature significantly from the last pulse. The temperature of the Nb has increased ~500°C. Also, the localized cooling due to the Nb fluting is much more evident. Figure 5.17 shows this localized cooling. It shows that the area near the Nb fluting is around ~200°C cooler than the hottest part of the pellet. Also, the outer surface of the fuel pellet is cooler than the inner region making the temperature profile no longer consistent with the fission profile. Figure 5.18 shows increased and more distributed heat fluxes in the fuel element. Rather than the largest heat flux occurring in the gaps between the Nb fluting and the fuel pellets, there is increased heat flux in the Nb itself. Because the thermal conductivity of the Nb is ~100 times greater than the thermal conductivity of He, it acts as a heat highway where heat can be transferred at a much higher rate than through the He. As the outer surface of the fuel

57

pellet decreases in temperature, the temperature difference within the fuel pellet increases,

increasing the heat flux within the fuel pellet.
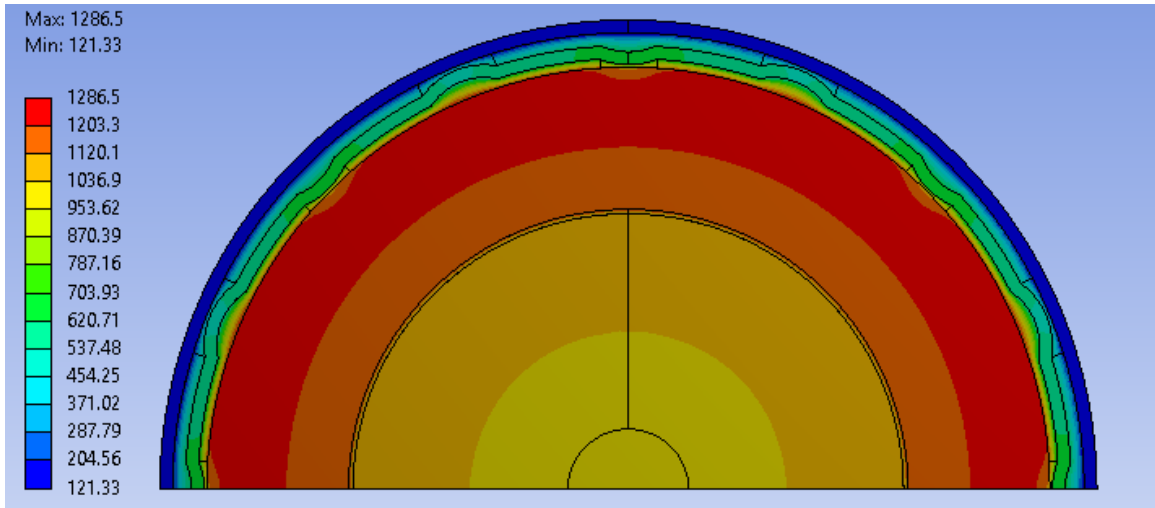
Figure 5.16: Temperature (°C) contour plot at the knee of the pulse (~0.80 s).
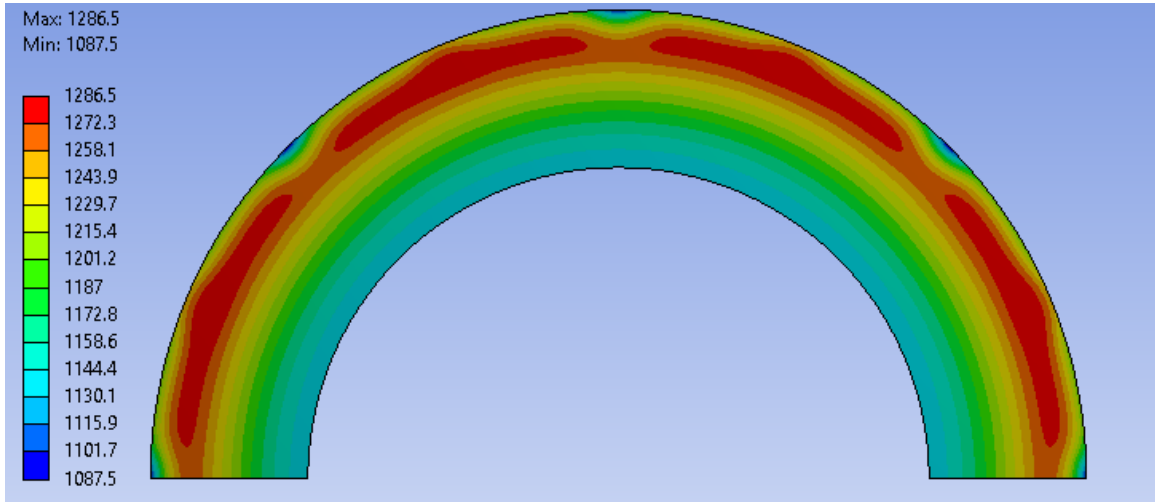

Figure 5.17: Temperature (°C) contour plot of the outer annulus of the fuel pellet at the knee of the pulse (~0.80 s).
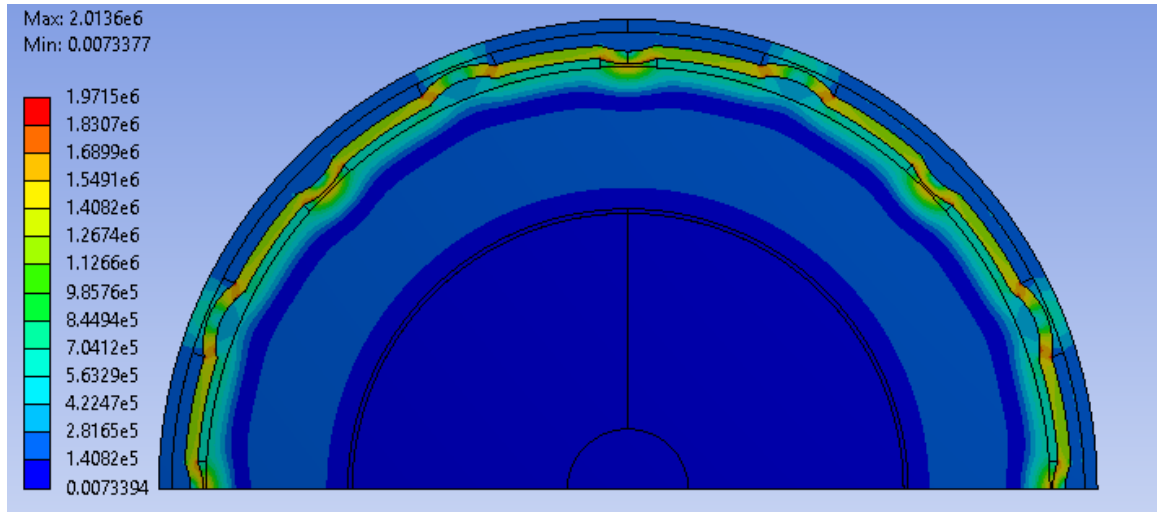
Figure 5.18: Heat flux (W/m^2) contour plot at the knee of the pulse (~0.80 s).

Figure 5.19-5.21 show the contour plots at the end of the simulation. Figure 5.19 shows an equilibrating of the fuel temperature. At his point the outer and inner annuli are nearly the same temperature. Also, the effects of the Nb fluting on the outer annulus' temperature are even more evident. The temperature gradients due to the fluting are no longer local, but instead are influencing the whole outer annulus. Figure 5.20 shows this even more clearly. The outer region of the outer annulus is ~110°C cooler than the inner region and the temperature contour clearly shows influence by the Nb fluting. The heat flux, shown in Figure 5.21, is now at its peak in the Nb.
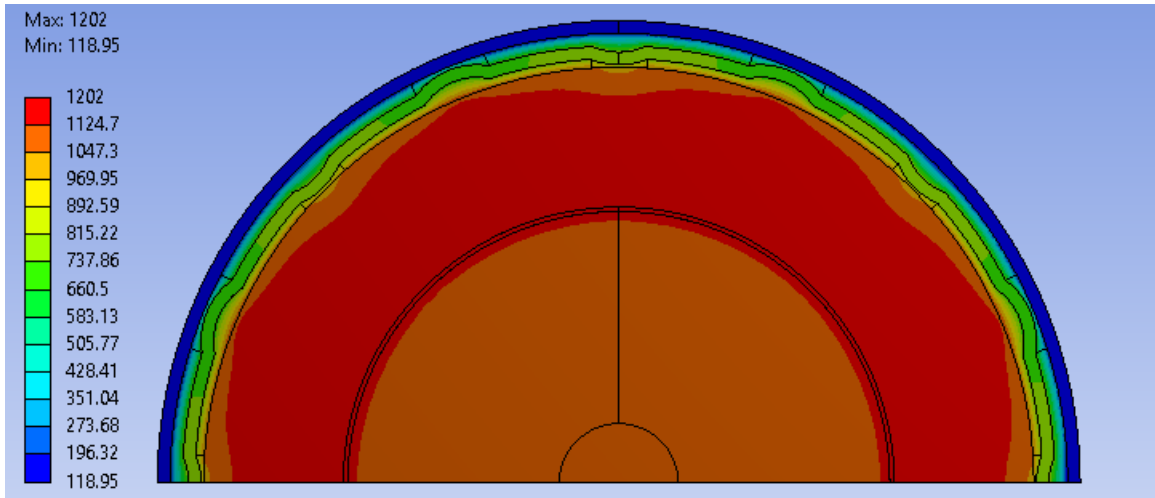
Figure 5.19: Temperature (°C) contour plot at the end of the simulation (5 s).
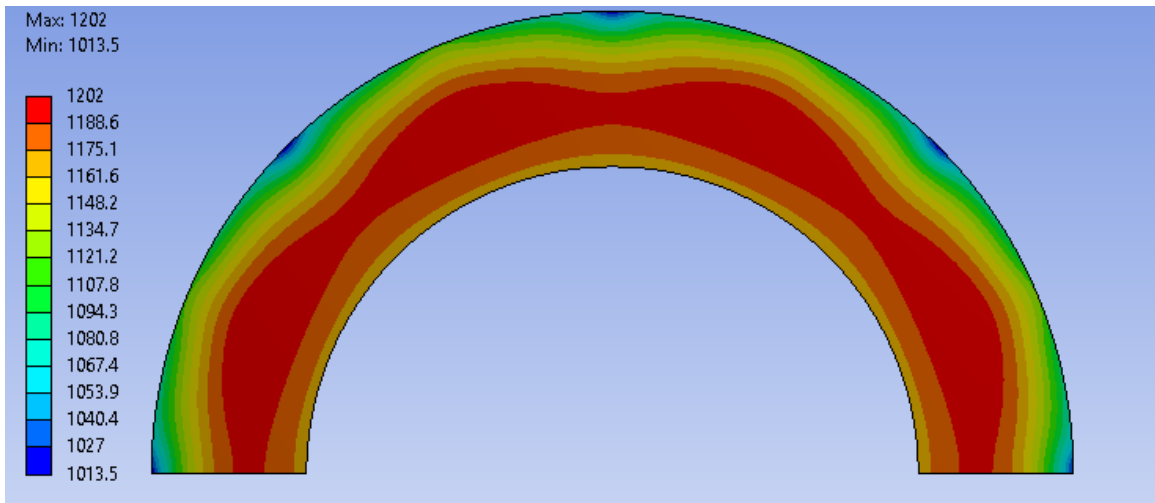
Figure 5.20: Temperature (°C) contour plot of the outer annulus of the fuel pellet at the end of the simulation (5 s).
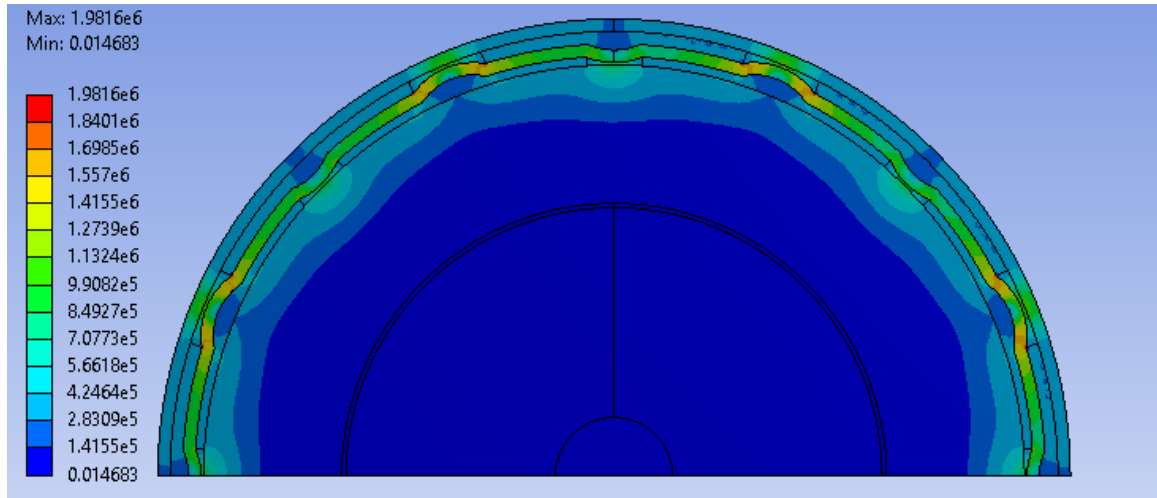
Figure 5.21: Heat flux (W/m^2) contour plot at the end of the pulse (5 s).

The heat flow in the fuel element is most clearly shown in Figure 5.22 and Figure 5.23. Both figures are vector plots of the heat fluxes at the end of the simulation. The figures show increased heat fluxes where the Nb can is closest to the SS and outer annulus fuel pellet. Figure 5.23 shows that the heat flux is higher in areas where the Nb can is closest to outer annulus of the fuel pellet and the SS cladding. This kind of heat flow causes localized heating of the SS cladding. This heat flow pattern is corroborated by the photograph of the cladding shown in Figure 5.24. The cladding has increased oxidation in a pattern that appears to correlate with the pattern of the Nb fluting. The increased oxidation indicates larger heat fluxes near the Nb fluting.
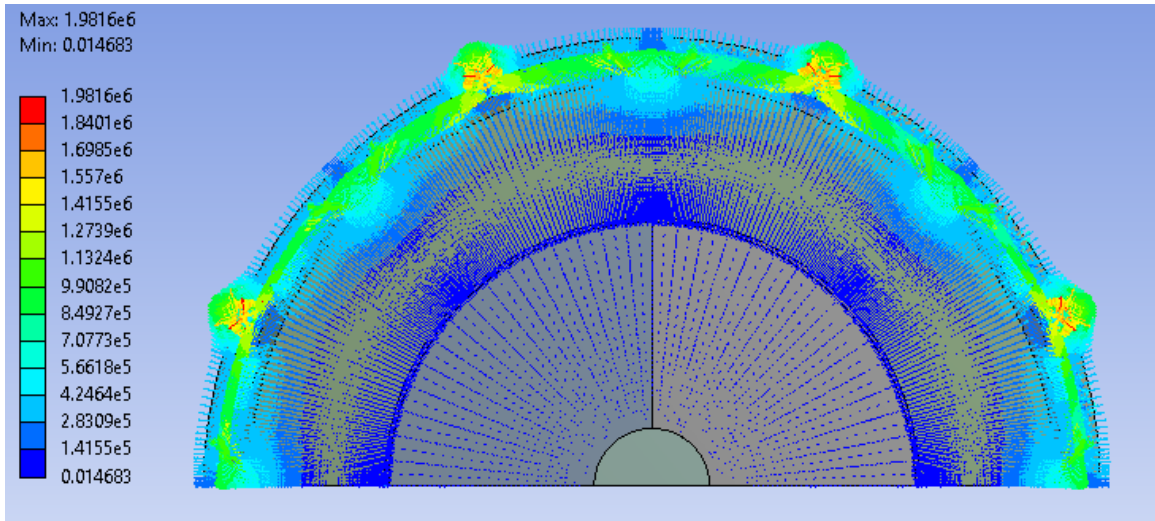
Figure 5.22: Heat flux (W/m^2) vector plot at the end of the simulation (5 s).
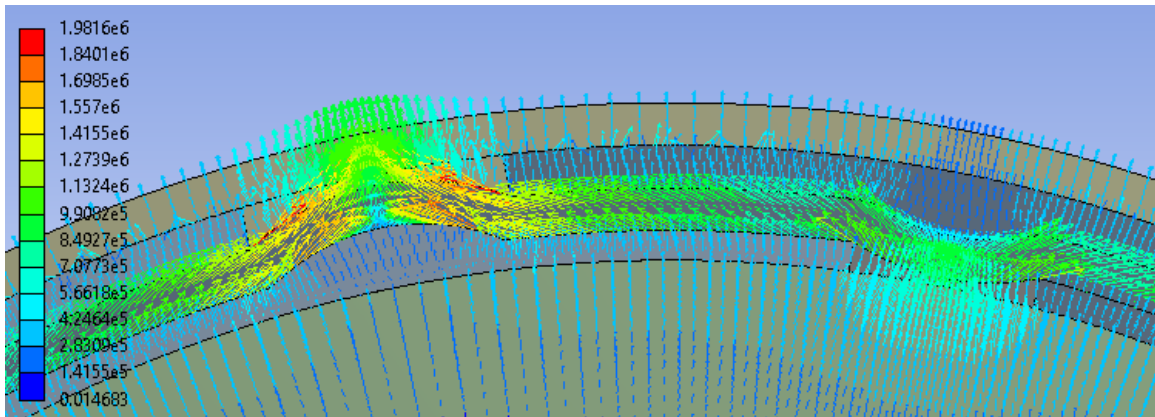
Figure 5.23: Heat flux (W/m^2) vector plot with close up of the gap at the end of the simulation (5 s).

Figure 5.24: Photograph of the outer surface of the cladding of a fuel element in the ACRR.

The temperature gradients calculated in this section are significantly different from the gradients induced by the fission profiles alone. The Nb fluting has a cooling effect on the outer annulus of the fuel pellet resulting in temperature differences up to 200°C. The stresses caused by these temperature gradients are discussed in Section 5.4.

5.4 Transient Structural Analysis

Only the outer annulus of the fuel pellet was modeled for the transient structural analysis. The outer annulus of the fuel pellets, as discussed previously, experiences the

largest thermal stresses and thus are most prone to fracture. The transient structural analysis was performed by applying the temperature gradients, which were calculated in the transient thermal analysis, to calculate the thermal stresses. Because the fuel pellet was assumed to be in the axial centerline of the fuel element, it was assumed that 8 fuel pellets were above, and 7 pellets were below the modeled fuel pellet. The weight of the pellets above and the resultant force were applied as forces on the upper and lower surfaces of the pellets. The force applied had a magnitude of 0.4431 N. Also, weak spring boundary conditions were applied to the whole model. Weak springs provide numerical stability for the analysis and provide a load to prevent motion normal to the force loads. Figure 5.25 shows the force loads that were applied as part of the structural analysis. The weak springs are applied to all the surfaces. The force loads, depicted by the red arrows in Figure 5.25, are distributed across the whole surface. Figure 5.26 and 5.27 show the meshed geometry used in this analysis.
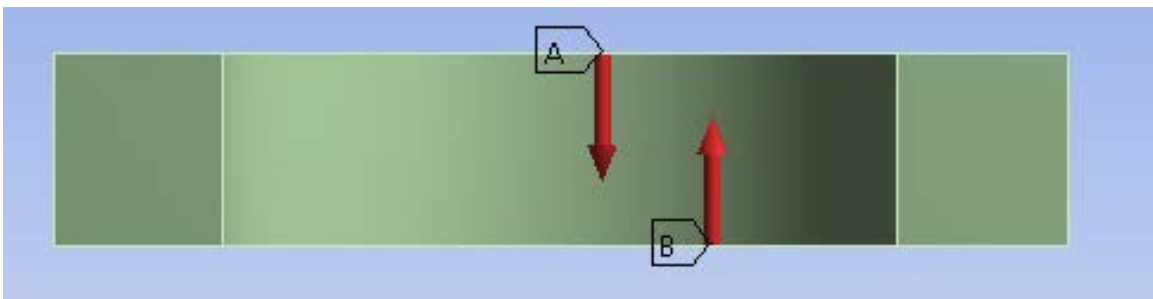
Figure 5.25: Transient structural constraints.
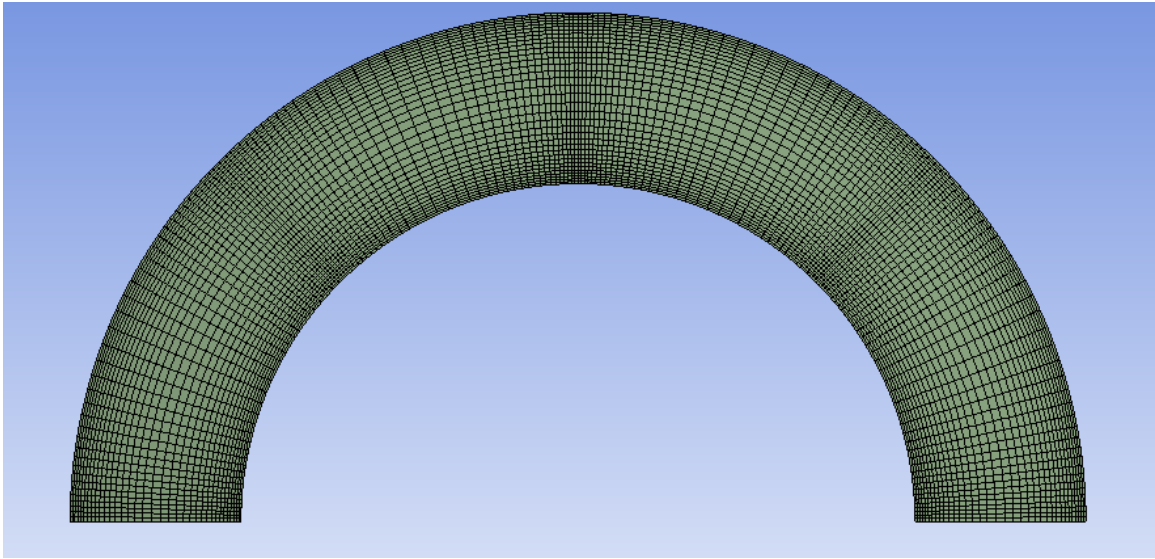
Figure 5.26: Top view of meshed geometry used for the structural analysis.
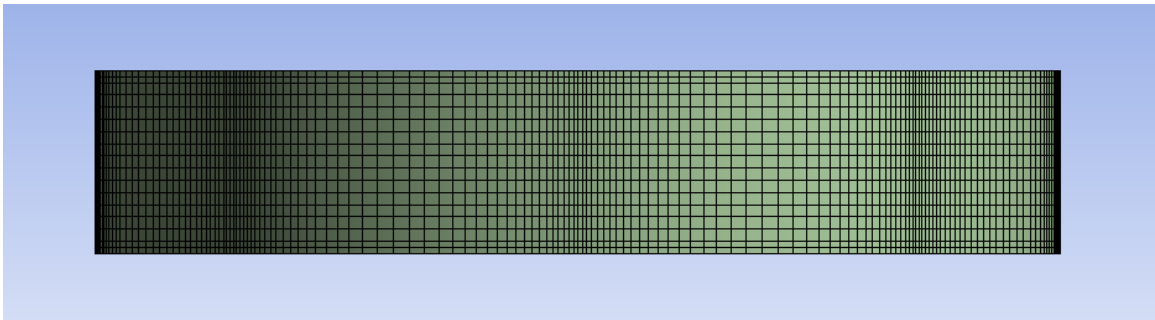
Figure 5.27: Side view of the meshed geometry used for the structural analysis.

5.4.1 Results

The results of the transient structural analysis are shown in Figure 5.28-5.39. Figure 5.28 shows the maximum principal stress in the outer annulus of the fuel pellet plotted along with the reactor power. It shows that the maximum principal stress occurs at ~0.5 s and has a magnitude of 700 MPa. As the temperatures equilibrate, the stresses decrease.

The vertical dashed lines show the times steps that are displayed in Figure 5.29-5.40. At each time step a top view, sectional view, and side view of the fuel pellet are shown.
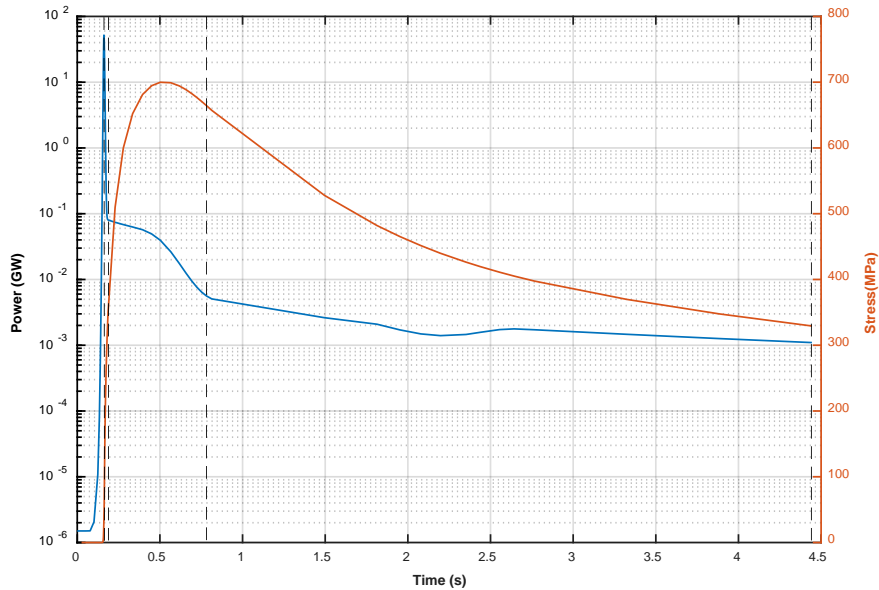
Figure 5.28: Principal stresses for a maximum pulse at current burnup.

Figure 5.29-5.31 show the contour plots of the stresses at 0.1617 s. Figure 5.29 shows the outer annulus of the fuel pellet from the top view. This view shows that there are no large stresses on the top or bottom surface of the fuel pellet. The solid black line, shown in the figure, is the shape of the undeformed fuel pellet. Not only has the pellet expanded radially at this time step, but outer edge has expanded more than the inner edge causing the ends of the fuel pellet to angle downward. Figure 5.30 shows the sectional view at this same time step. It shows that the maximum stresses, at this time step, occur in the radial center of the fuel pellet. This indicates that the fission profile causes the stresses. Figure 5.31 shows the thermal stresses on the outer surface of the fuel. The plot shows

66

large thermal stresses exactly where Nb can causes cooling. These stresses show that the cooling, that is caused by the fluting of the Nb can, does cause thermal stresses. The section view shows the stresses at the axial centerline of the pellet as if the upper half of the pellet was invisible.
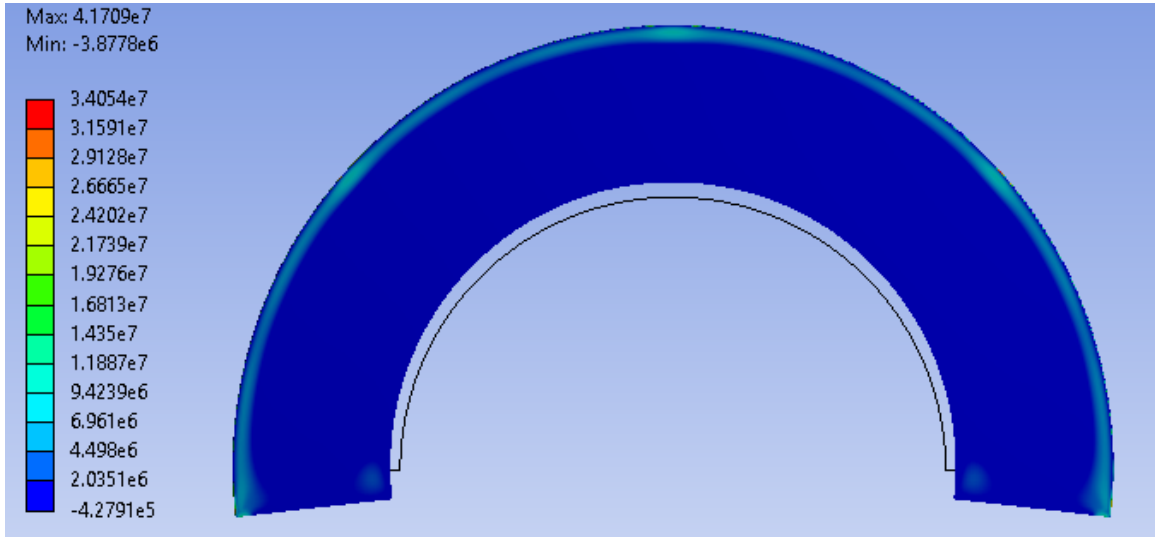
Figure 5.29: Top view of maximum principal stresses at ~0.1617 s.
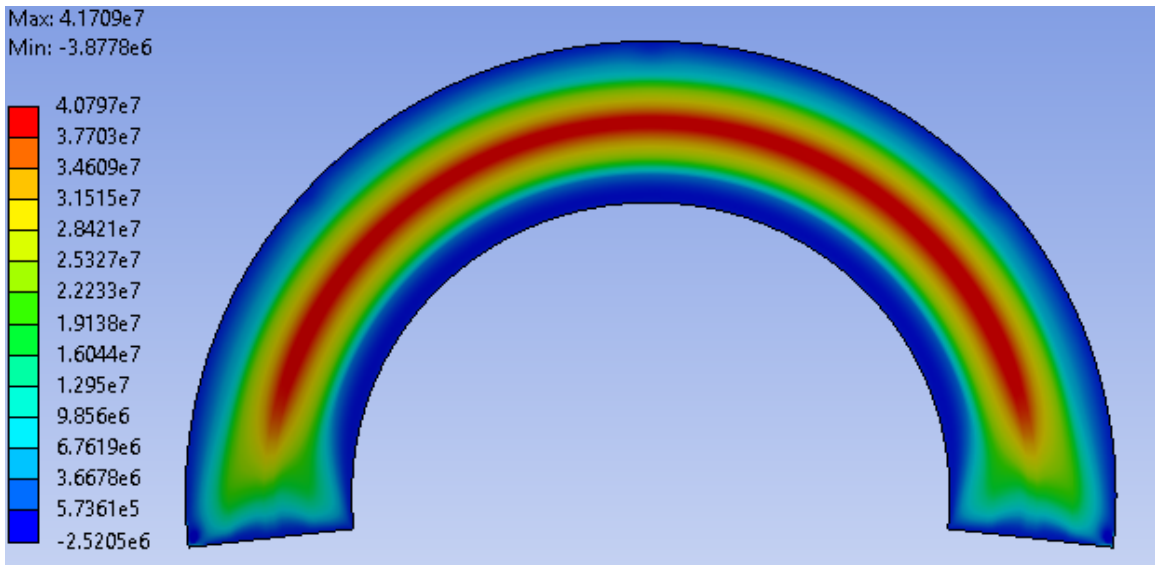
Figure 5.30: Section view of maximum principal stresses at ~0.1617 s.

67
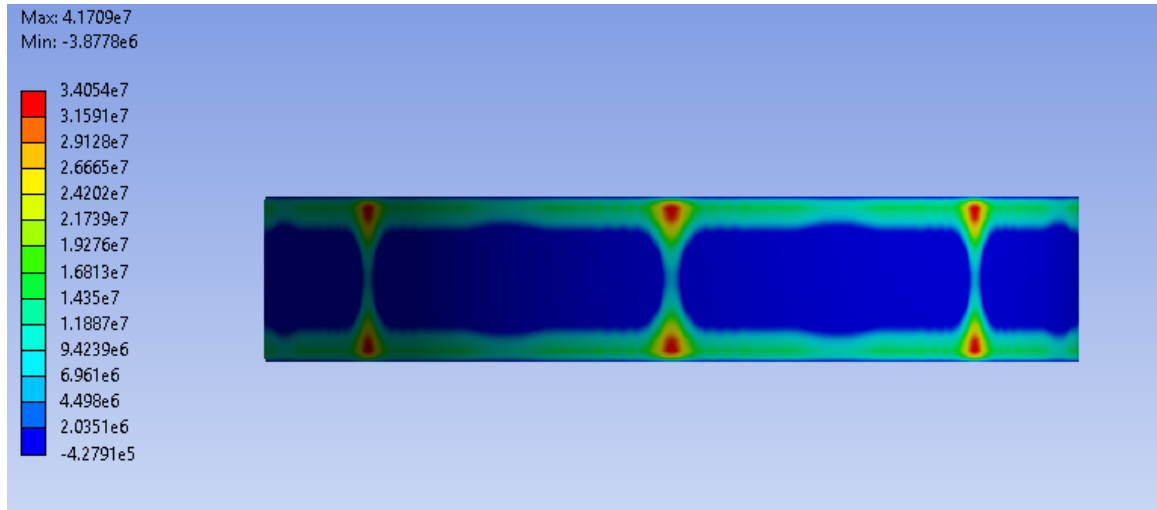
Figure 5.31: Side view of maximum principal stresses at ~0.1617 s.

Figure 5.32-5.34 show the thermal stresses at 0.18 s. Figure 5.32 shows the thermal stresses from the top. The stress profile is very similar to that of the previous time step except an order of magnitude higher in very localized regions. The strains also appear to be larger than the previous step. Figure 5.33 shows the stress contour of the section view. The thermal stresses from the fission profile are still visible, however the fission profile is no longer the source of the maximum stresses. Figure 5.34 shows the thermal stresses of the outer surface of the fuel pellet. The figure shows large thermal stresses where the fuel pellet experiences cooling due to the Nb fluting. The stresses are very superficial as they can barely be seen from the section view.
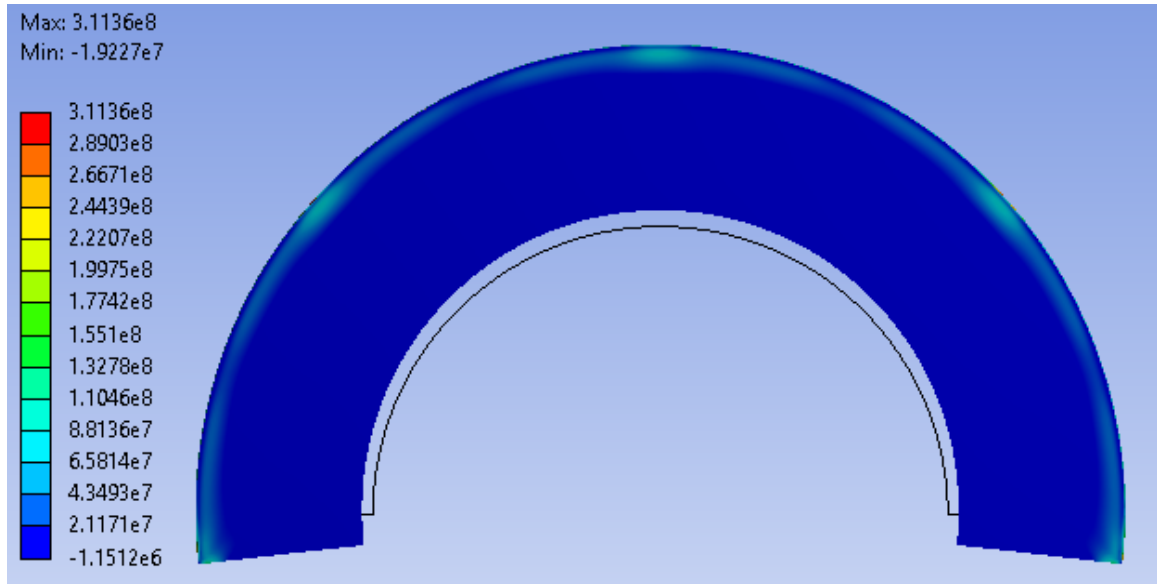
Figure 5.32: Top view of maximum principal stresses at ~0.18 s.
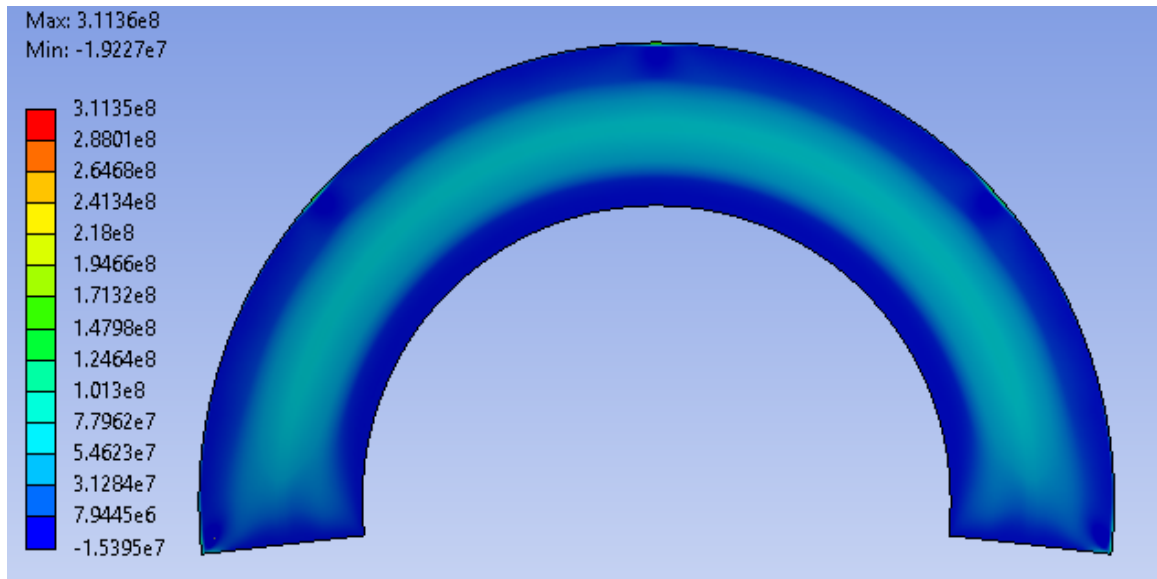
Figure 5.33: Section view of maximum principal stresses at ~0.18 s.
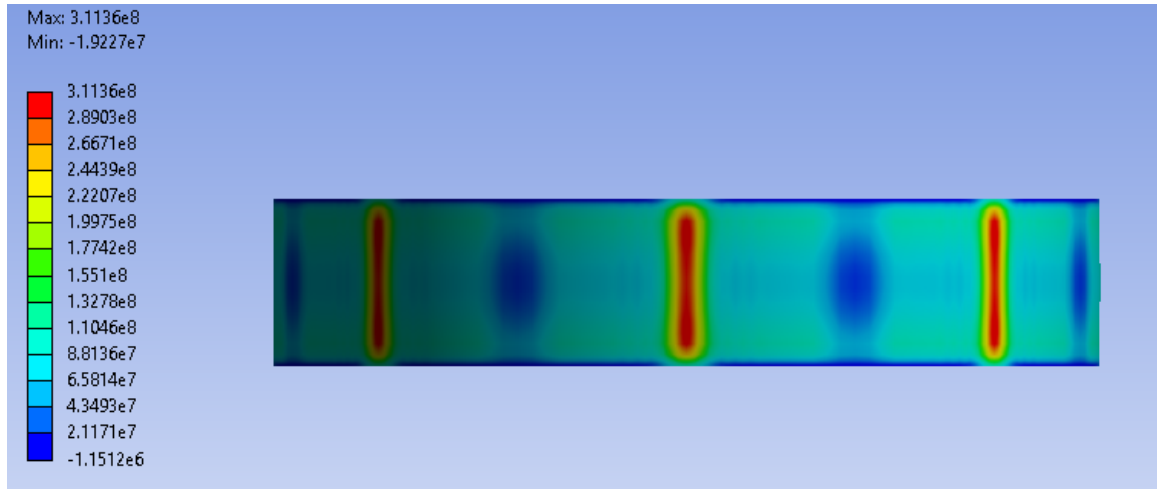
Figure 5.34: Side view of maximum principal stresses at ~0.18 s.

Figure 5.35-5.37 show the thermal stresses at 0.8 s. Figure 5.35 shows the thermal stress from the top view. The thermal stresses are no longer only seen close to the outer surface. The middle section of the fuel is also experiencing the thermal stresses. The deformation of the fuel pellet is more relaxed at this time step with less deformation caused by the heating of the outer surface. Figure 5.36 shows the section view. The thermal stresses caused by the fission profile are no longer dominant at this time step. The maximum thermal stresses occur on the outer surface of the fuel where the Nb can causes cooling. Figure 5.37 gives a clearer view of the maximum thermal stresses. Although the whole height of the fuel pellet is not being affected, the stresses are double those of the last step. The maximum stresses at this time step are 657 MPa.

70
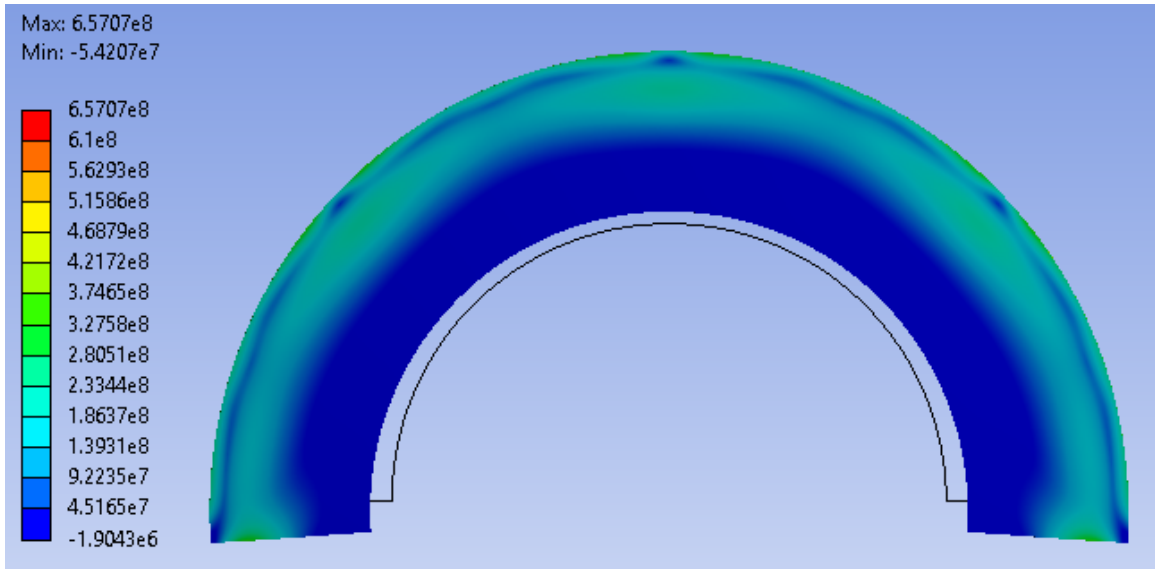
Figure 5.35: Top view of maximum principal stresses at ~0.8 s.
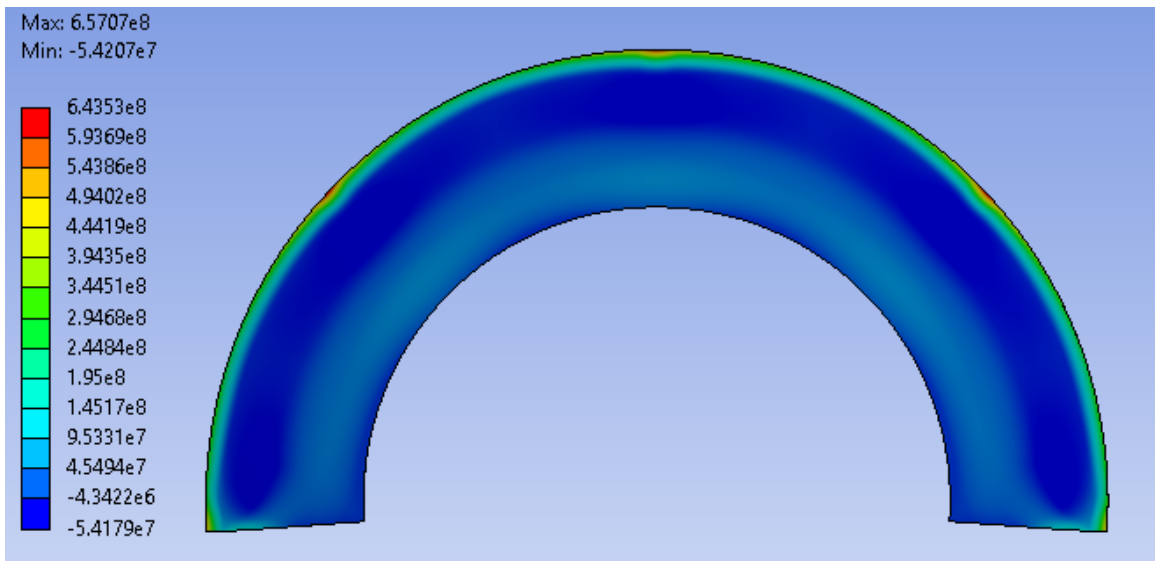
**Figure 5.36: Section view of maximum principal stresses at ~0.8 s.**
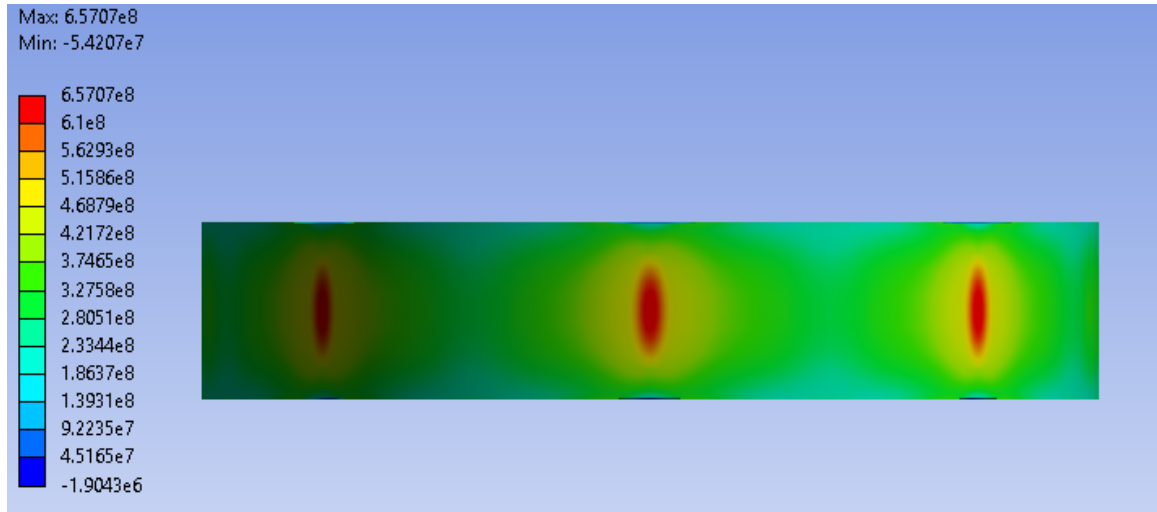
Figure 5.37: Side view of maximum principal stresses at ~0.8 s.

The thermal stresses of the last time step are shown in Figure 5.38-5.40. Figure 5.38 shows that the thermal stresses affect a much larger volume than 0.8 s. Also, the strain is much more uniform with the ends of the fuel pellet nearly parallel to their starting position. The largest stresses in this view occur at the outer surface of the fuel pellet. Figure 5.39 shows a section view of the fuel pellet at this time step. The center portion of the fuel pellet is in a state of compression while the outer surface of the fuel pellet is in tension. The maximum principal stresses are due to the cooling of caused by the Nb can. Figure 5.40 shows that the stresses on the outer surface are much more distributed, however the peak stresses occur due to the cooling induced by the Nb can.
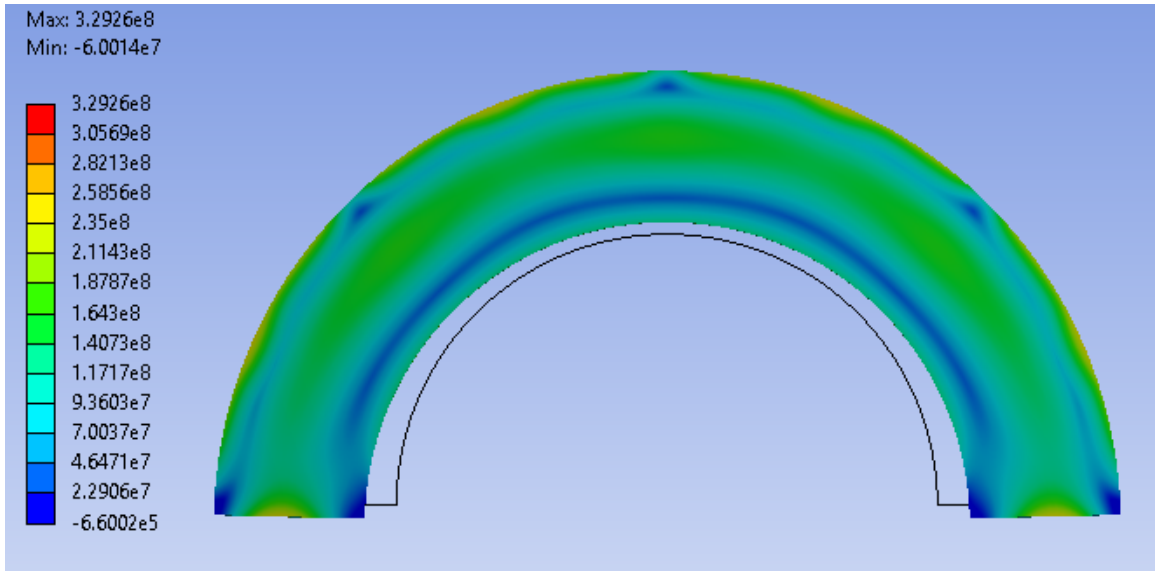
Figure 5.38: Top view of maximum principal stresses at ~4.4 s.
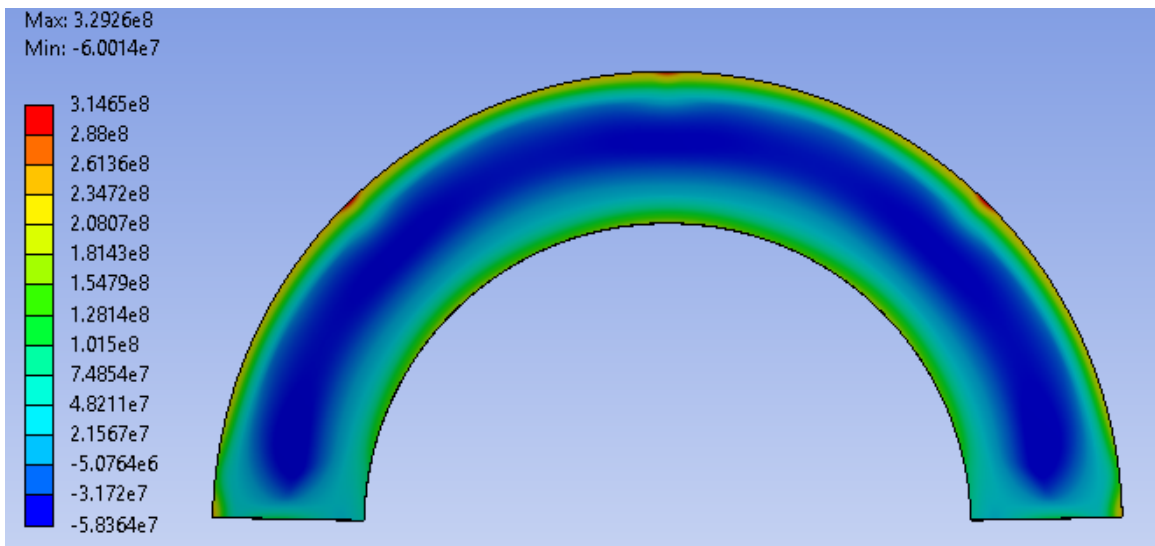
**Figure 5.39: Section view of maximum principal stresses at ~4.4 s.**
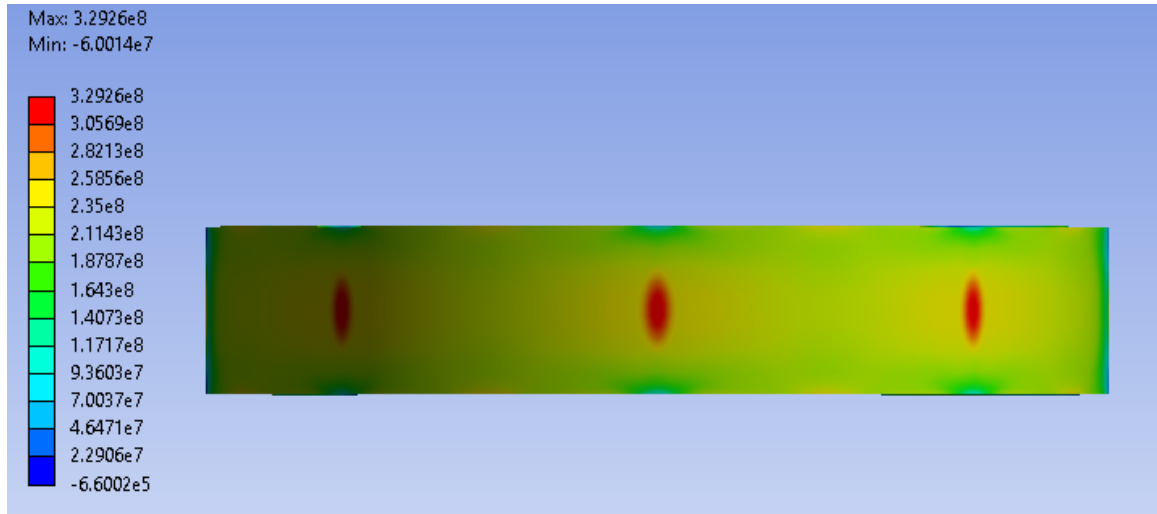
Figure 5.40: Side view of maximum principal stresses at ~4.4 s.

Unlike what was observed when calculating the thermal stresses induced by the fission profiles, the largest stresses experienced by the fuel pellets in transient operations occur at the outer surface. The Nb can has a clear impact on the stresses in the fuel due to the localized cooling it causes. The maximum calculated thermal stresses are shown in Figure 5.41-5.43. They all clearly show that the cooling caused by the Nb can causes the peak stresses. Figure 5.41 shows the maximum principal stress state in the fuel pellet from the top view. The maximum stresses cannot be seen from this view, but thermal stresses are present on the upper surface of the fuel. These stresses are highest were the local cooling due to the Nb can occurs. Figure 5.42 shows the section view of the stress state. It shows that although the stresses caused by the cooling due to the Nb can are very large, they are very localized and influence a very small volume of the fuel pellet. Figure 5.43 shows that the thermal stresses do not span the height of the fuel pellet. Aside from the thermal stresses caused by localized cooling, the outer surface experiences thermal stresses

74

caused by the cooling of the fuel pellet. These stresses are nearly half of the peak stresses. The contraction caused by the cooling of the outer surface of the fuel pellet causes compressive stresses inside the fuel pellet.
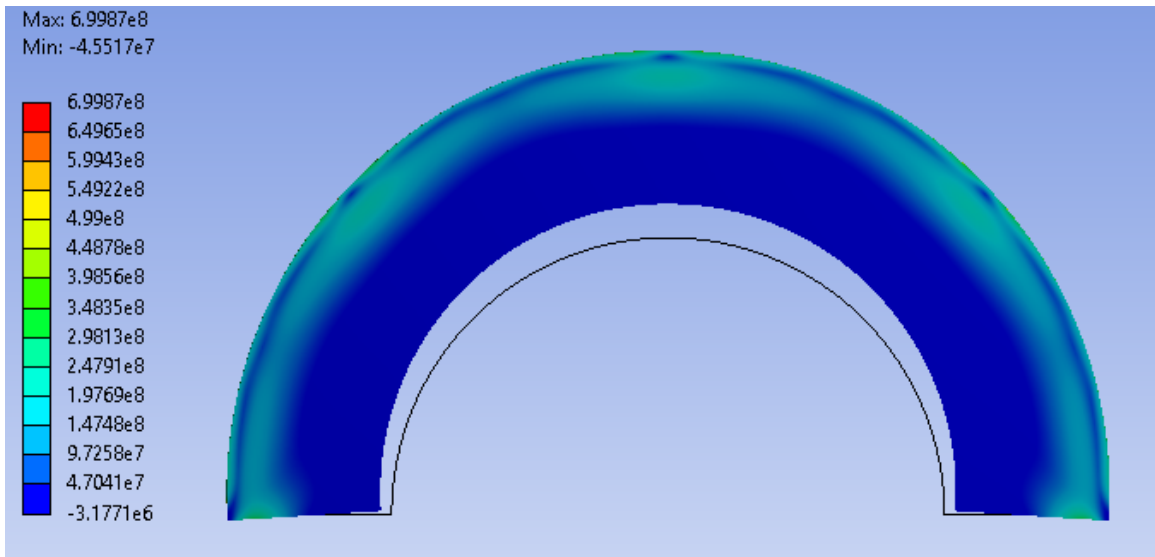
Figure 5.41: Top view of the peak stresses in the outer annulus of the fuel pellet over the 5 s simulation.
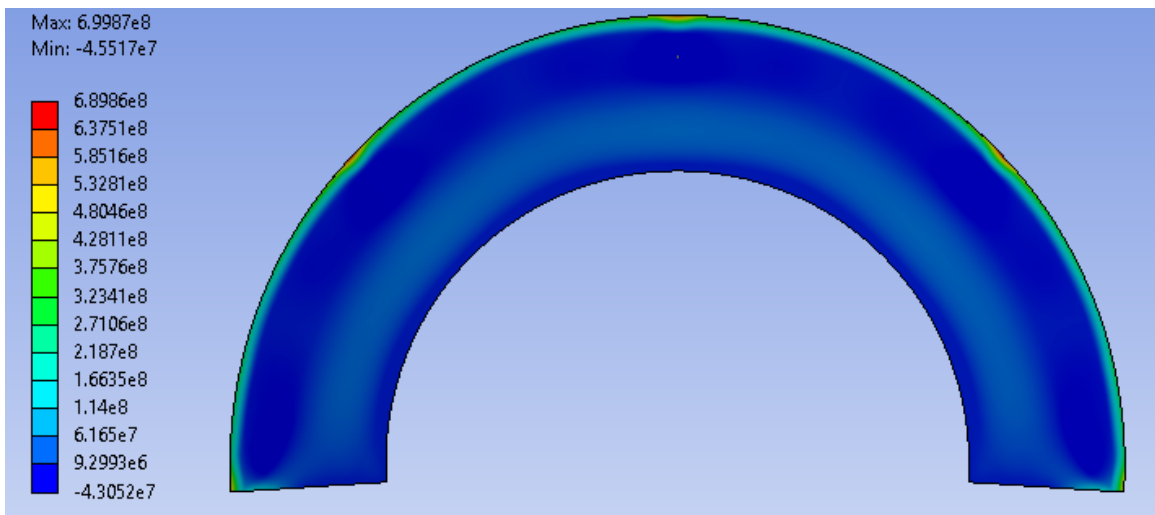
Figure 5.42: Section view of the peak stresses in the outer annulus of the fuel pellet over the 5 s simulation.
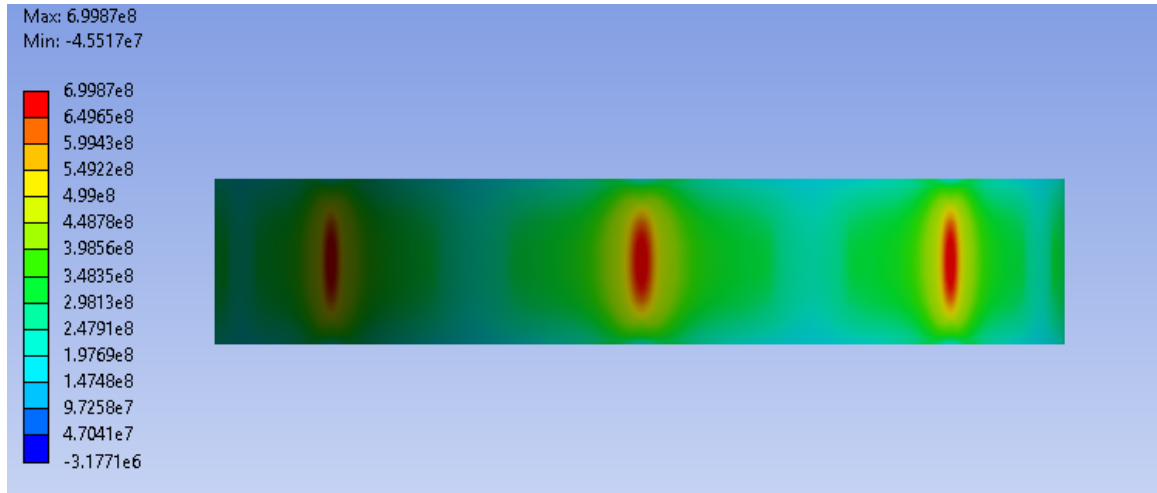
Figure 5.43: Side view of the peak stresses in the outer annulus of the fuel pellet over the 5 s simulation.

5.5 Discussion

The contour plots shown in Figure 5.29-5.43 show the progression of the thermal stresses in a peak fuel pellet over the first 5 s of a pulse operation. From the initiation of the pulse, at 0.08 s, to 0.1633 s the thermal stresses in the fuel pellet are dominated by the fission profile. After 0.1633 s, the thermal stresses are caused by the temperature gradients towards the outer surface of the fuel pellet caused by the Nb fluting. Figure 5.44 shows the maximum principal stresses during the transient thermal analysis along with the maximum principal stresses from an adiabatic analysis. The adiabatic analysis was performed in the same way as the transient thermal analysis except it was assumed that there was no heat loss from the pellet. This assumption allowed for the calculation of the thermal stresses strictly caused by the fission profile. Figure 5.44 shows that the maximum

principal stresses diverge at 0.1633 s which is when the thermal stresses become dominated

by the stresses induced by heat loss.
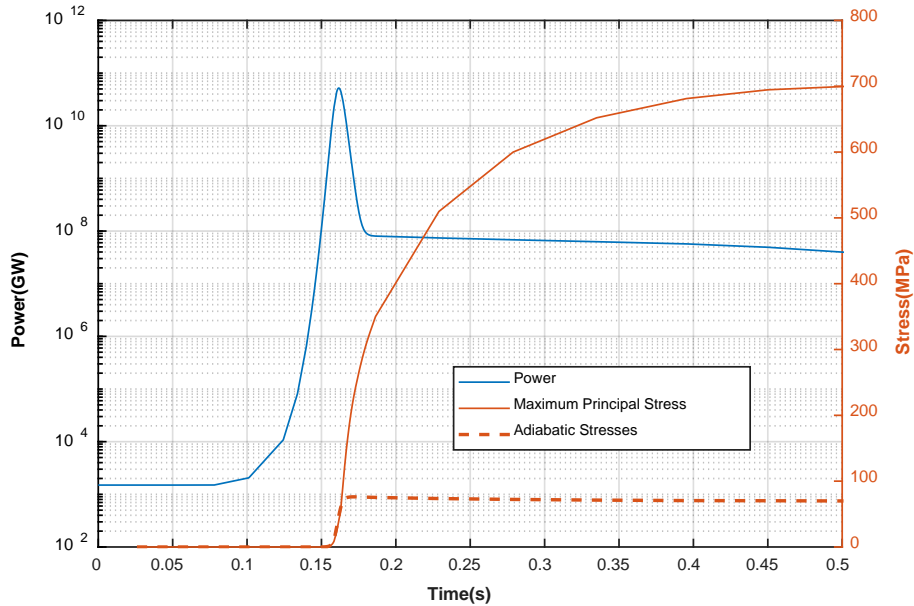
Figure 5.44: Adiabatic and transient thermal stresses in the peak fuel pellet.

The purpose of the in-pile testing, discussed in Chapter 2, was to determine whether

the fuel pellets were able to survive the fission profile induced thermal stresses. If the

stresses caused by heat loss are neglected, the stresses that the fuel pellets experience are

well below the range that pellets began to fracture during the in-pile experiments (76 MPa

vs 150 MPa). The stresses caused by localized cooling, however, were 10 times larger than

the maximum principal stresses caused by the fission profile alone. These stresses, when

examined alongside neutron radiography of the peak fuel element that was performed in

1989, do not seem to have any impact on the structural integrity of the fuel. Figure 5.45

shows a radiograph of the center Nb cup of a peak fuel element. There is no obvious

cracking shown by the neutron radiograph and all the fuel pellets appear to be intact.
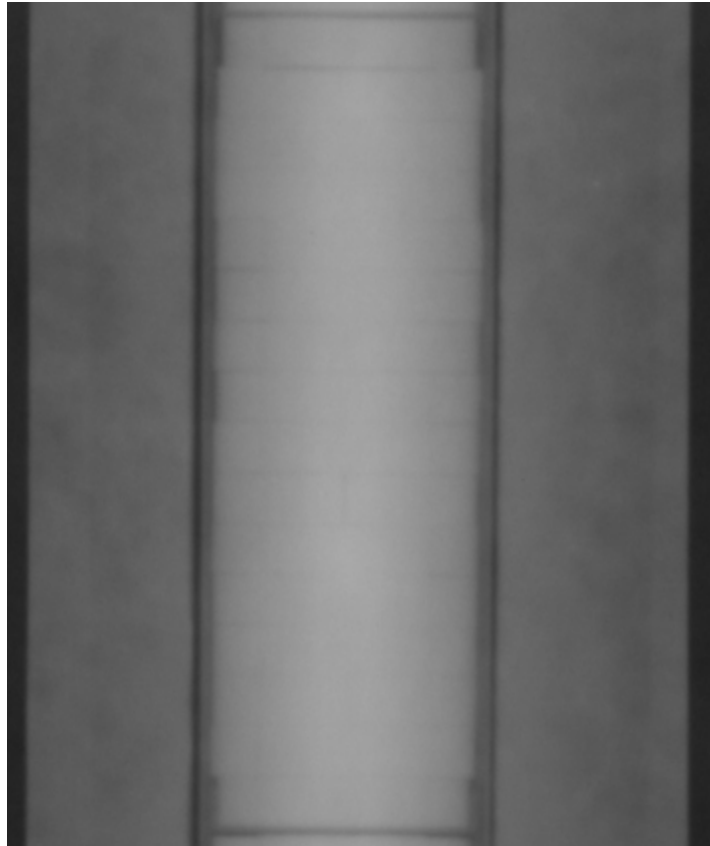
Figure 5.45: Neutron radiography of the peak fuel element in the ACRR.

Since the radiography was performed, the ACRR has been in operation for 30 years

and accrued burnup. To ensure that the large thermal stresses were not a result of changes

in material properties due to burnup, a transient thermal and transient structural analysis

was performed on the fuel with properties of the fresh fuel. Figure 5.46 shows the

maximum thermal stresses in the outer annulus of the fuel pellet with respect to time. It

shows that, although the thermal stresses are less than those calculated in the current fuel,

they still are at levels nearly double those the pellets survived in the in-pile experiments discussed in Section 4.6. The calculated stresses, even for the fresh fuel, would indicate fuel is fracturing.
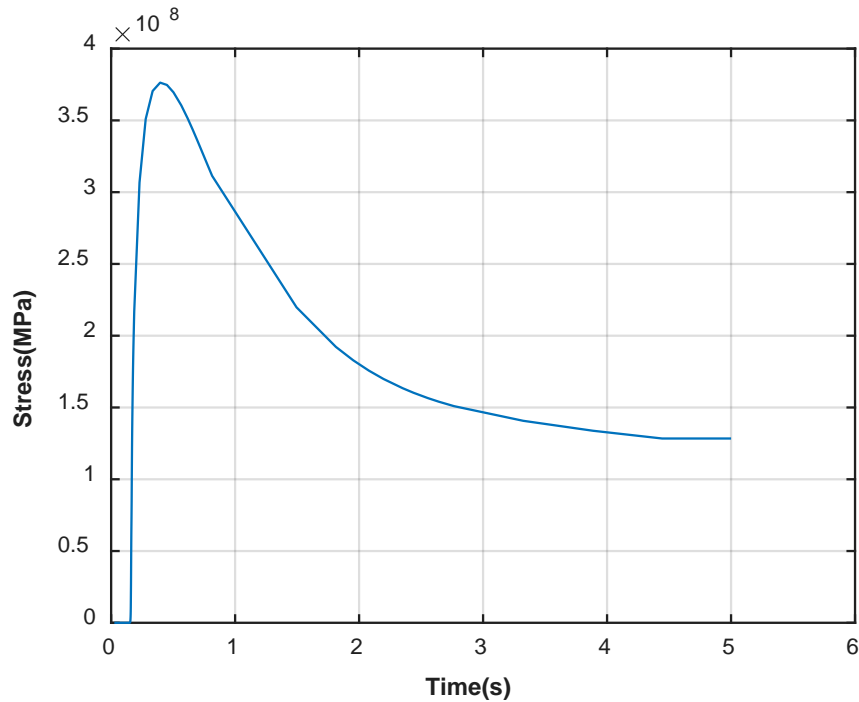
Figure 5.46: Maximum principal stress for a maximum pulse with no burnup.

There are several possible explanations for the discrepancy between conclusions drawn from neutron radiographs and the calculated stresses during the transient thermal simulation. The first of these explanations is that the calculated stresses could be artificially high due to incorrect material properties. The thermal stresses of fuel are directly related to the fuel's material properties; however, the material properties of the fuel are very poorly characterized. Without proper materials testing this possibility cannot be ruled out, however a material property sensitivity study was performed to examine how sensitive the

stresses are to the material properties of the fuel. The sensitivity study can be found in Chapter 6. Another possible reason for discrepancy is that the neutron radiography performed was not of high enough resolution to detect cracking. Without performing further neutron radiography, this explanation cannot be further investigated. Even if the radiography performed was too low in resolution to detect cracks, it is clear that the pellets are still intact, and the overall structure of the fuel pellets was not affected by the stresses. The final possible reason for the disagreement between the simulation and the radiography is that peak stresses occupy such a small volume of fuel that either they do not encounter a critical flaw, or they cause localized cracking but not complete fracture. This possibility is examined further in Chapter 7.

6   PARAMETRIC STUDY ON THE EFFECTS OF MATERIAL PROPERTIES ON THERMAL STRESSES

To better understand the thermal stresses sensitivity to the material properties, the material properties directly related to thermal stresses where varied by 25%. These properties include the thermal conductivity, CTE, and modulus of elasticity. For the sake of brevity, only the maximum stresses of the simulation will be compared in each analysis. These analyses were performed in the same manner described in Chapter 5. The material properties varied were those of the fuel with burnup.

6.1 Thermal Conductivity

The thermal stresses within a material are directly related to the materials thermal conductivity [54]. Materials with higher thermal conductivities have less severe temperature gradients and lower thermal stresses because the heat can be more uniformly distributed through the material. The simulation shows that a 25% increase in thermal conductivity will result in thermal stresses of 614 MPa which is a 12% decrease. Conversely a 25% decrease in thermal conductivity will result in a 18% increase in the thermal stresses. Table 6.1 documents the effects.

Table 6.1: Thermal conductivity sensitivity.

Thermal Conductivity	Maximum Principal Stress (MPa)	Percent Change (%)
25% ↑	614	-12
-	700	-
25% ↓	823	+18

6.2 Modulus of Elasticity

Stress, in any material, is proportional to the modulus of elasticity multiplied by the strain of the material. This relation is shown in Hooke's Law. The analysis showed a 25% decrease in the modulus of elasticity results in thermal stresses of 525 MPa which is a 25% decrease. A 25% increase in the modulus of elasticity would result in a 25% increase in stress. These results are shown in Table 6.2.

Table 6.2: Modulus of elasticity sensitivity.

Modulus of Elasticity	Maximum Principal Stress (MPa)	Percent Change (%)
25% ↑	875	+25
-	700	-
25% ↓	525	-25

6.3 Coefficient of Thermal Expansion

As mentioned in Section 6.2, the stresses in a material are proportional to the strain. Thermal stresses are induced when materials expand when heated so they are related to the CTE. The analysis showed a 25% decrease in CTE would result in thermal stresses of 525

MPa which is a 25% decrease in thermal stresses. A 25% increase would result in a 25% increase in thermal stresses. These results are shown in Table 6.3.

Table 6.3: Coefficient of thermal expansion sensitivity.

Coefficient of Thermal Expansion	Maximum Principal Stress (MPa)	Percent Change (%)
25% ↑	875	+25
-	700	-
25% ↓	525	-25

6.4 Discussion

Because there is a high level of uncertainty in the material properties, it is helpful to know how sensitive the thermal stresses are to changes in the properties. This analysis showed that the thermal stresses are most sensitive to the both the modulus of elasticity and CTE and a 25% change can affect the stresses by as much as 25%.

7 EFFECTS OF THE STRESSES FROM A FRACTURE MECHANICS PERSPECTIVE

Rather than treat the fracture stress as a material property, fracture mechanics acknowledges that the fracture stress of a material is dependent on a materials microstructure and the presence of flaws [54]. The flaws in a material act as stress concentrators which are where cracks initiate. Alan Griffith, one of the forefathers of fracture mechanics, examined fracture from an energy standpoint [55]. He hypothesized that cracks will only propagate in an unsteady manner when it is energetically favorable to do so i.e. when the potential energy of the system decreased. From his work, the fracture toughness was derived. Fracture toughness is the critical stress concentration factor that is required for crack propagation. The equation of fracture toughness is shown in Eqn. 7.1 where K_{IC} is the fracture toughness, σ_0 is the fracture strength, Y is a geometric constant, and a is the crack length. When solved for the fracture stress, Eqn. 7.1 shows that the fracture stress is a function of crack size and fracture toughness.

$$K_{IC} = Y * \sigma_0 \sqrt{a * \pi} \qquad \text{Eqn. 7.1}$$

Equation 7.1 can be used to find the maximum possible strength of the fuel in the ACRR. Because the mechanical and microstructural properties of the fuel are poorly characterized, several assumptions were made to calculate the maximum strength. The first of the assumptions was that the fracture toughness of the fuel is approximately the fracture toughness of BeO. This assumption is made since 93 v/o of the fuel is BeO. The second assumption was that the minimum crack size of the fuel is no larger than the largest grain

84

size of UO_2 (~1µm). This assumption treats the UO_2 particles as voids in the BeO matrix. The final assumption is that the pellet satisfies the plane strain condition meaning the width of the pellet is much greater than the length of the crack. Under these assumptions, the fracture toughness, K_{IC}, can be calculated from the fracture energy of BeO, which is 32.3 J/m^2 [56]. Equation 7.2 demonstrates the fracture toughness of a material as a function of fracture energy, G_c, and modulus of elasticity.

$$K_{IC}=\sqrt{G_c*E}$$
Eqn. 7.2

Using the current value of elastic modulus at 1200°C, which is 310 GPa, the fracture toughness is approximately 3.16 MPa√m. Using the fracture toughness and Eqn. 7.1, the maximum strength of the fuel can be estimated to be 782 MPa. When examined along with the results shown in Table 4.9 of Section 4.8 it can be inferred that the reason that some pellets begin to fracture at much lower thermal stresses than others is due to the presence of internal flaws in the pellets. Inversely, it is likely that the pellets that were able to withstand larger stresses had smaller internal flaws.

Because of the large variability of strength in brittle materials, it is common to use Weibull statistics to determine the probability of failure at a given stress level. To use Weibull statistics however, it is essential to use identical test specimens with a similar stress distribution to that in which the material will be used [57]. The requirement for similar stress distributions acknowledges the fact that a larger volume has a larger probability of a critical flaw. In other words, if two specimens have a uniform stress applied, but one has a larger volume to which the stress is applied, the specimen with the larger volume has a

higher likelihood of having a critical flaw and thus a higher likelihood of fracturing. It is possible for this reason that no fracturing was observed in the neutron radiography shown in Section 5.4. The thermal stresses that are caused by the local cooling near the fluting is over a small volume compared to the stresses caused by the fission profile thus they have a lesser likelihood of interacting with a flaw large enough to cause fracture. Also, it is possible that some cracking did occur, but it did not propagate through the pellet. This possibility is further discussed in Section 7.1.

7.1 Effect of Cracks on Stress

As mentioned in Section 7, Griffith proposed that cracks will not propagate unless it is energetically favorable to do so. Based on the principal of minimum potential energy, it is energetically favorable for the crack to propagate when the total energy of the system decreases. It is possible, however, that cracks do occur near those peak stresses on the outer surface of the fuel, but they do not propagate through the entire pellet to cause fracture. To examine this idea, 'cracks' were introduced to the outer surface of the fuel pellet using ANSYS Workbench's element death feature. This feature removes the selected elements from the analysis by giving it a very small stiffness [44]. The cracks were introduced where the thermal stresses were highest in the fuel pellet, and the transient structural analysis was performed from 0.18 s to 0.8 s which is the time frame where the peak stresses occur. The introduction of cracks in the fuel caused stress singularities at the corners of the crack.

Figure 7.1 shows the singularities at one of the cracks. It was assumed that the singularities were only an artifact of the simulation, so they were neglected.
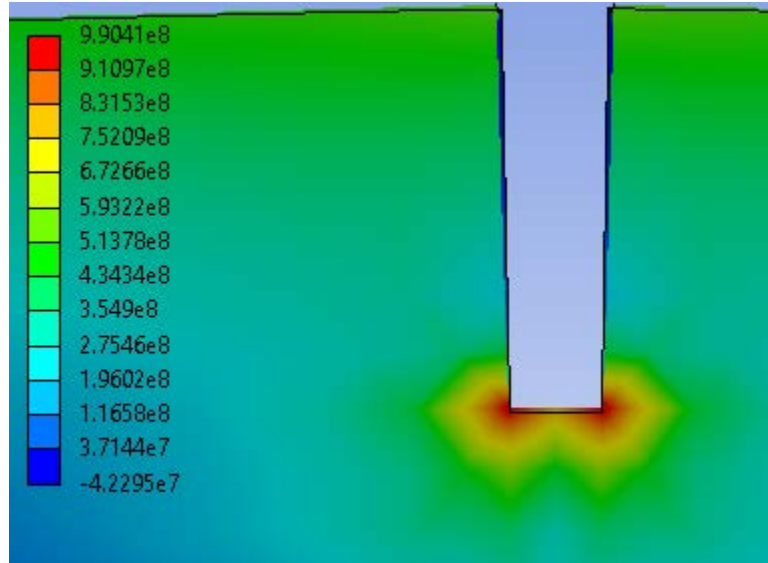
Figure 7.1: Stress singularity at crack corners.

Because the stress singularities due to the cracks were neglected, the scales of Figure 7.2 and 7.3 were adjusted so that the maximum stress displayed is 700 MPa. With the adjusted scale, neither Figure 7.2 nor Figure 7.3 showed stresses of 700 MPa. The maximum principal stress with cracks introduced was 555 MPa which was a reduction from the 700 MPa in uncracked fuel. The competition between the thermal stresses on the outer surface of the fuel is reduced when a crack is introduced thus reducing the thermal stresses. If cracks in the fuel did nucleate and did not propagate through the pellet, the stresses could be reduced in the fuel pellet.
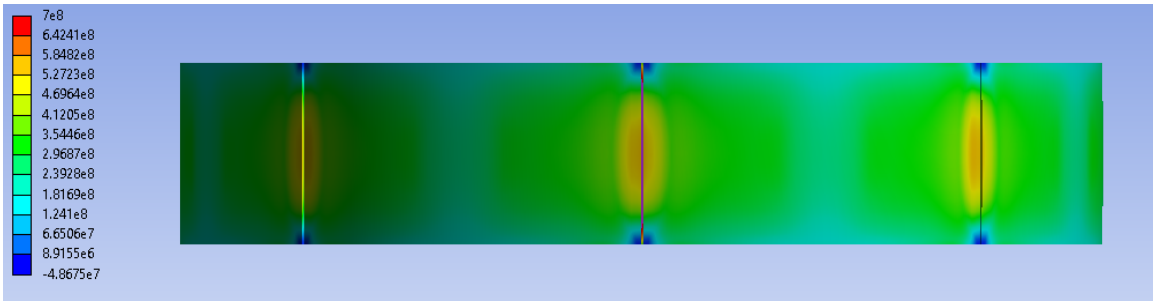
Figure 7.2: Side view of maximum principal stresses in the model with cracks.
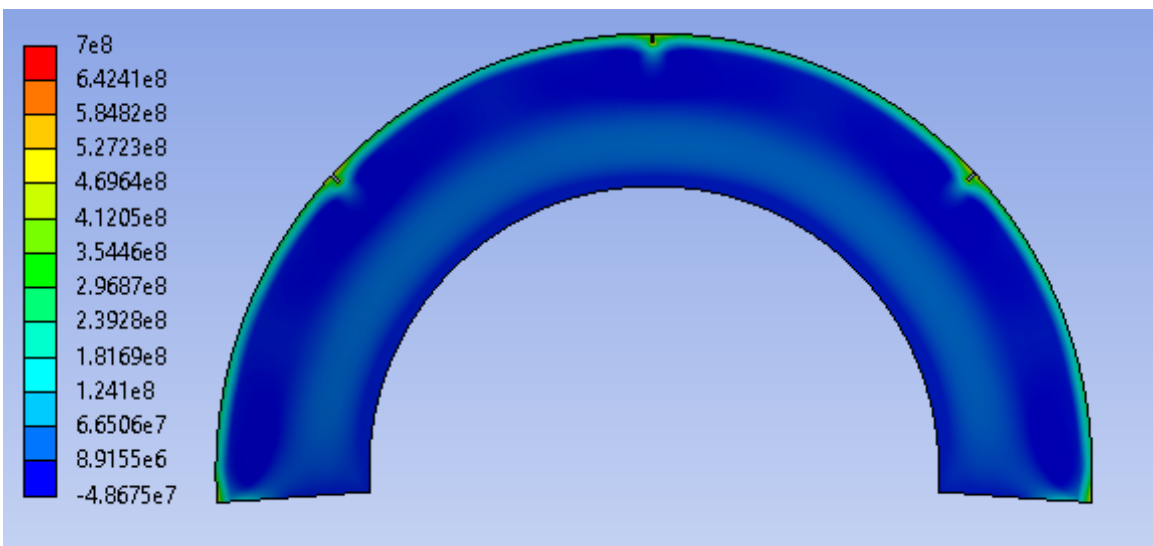
Figure 7.3: Section view of maximum principal stresses in the model with cracks.

7.2 Effect of Fracture on Stress

Another analysis was performed to examine whether the stresses in a fuel pellet would be affected if the pellet fractured. The purpose of this study was to determine if initial fracture did occur, whether the thermal stresses in the resultant pieces would be reduced as a result of the fracture. This analysis examined the average thermal stresses in a fuel pellet if the pellet cracked 0, 2, 4 or 8 times. A full transient thermal analysis was not performed for this portion of the analysis. Instead, it was assumed that the thermal

stresses from the fission profile were the cause of fracture. Figure 7.4 shows a plot of the maximum thermal stresses with respect to the number of fractures that occurred. It shows that fracture does reduce the stresses caused by the fission profile in the fuel pellet and that the more the fuel fractures, the more the stresses are reduced. If the pellets do fracture, it will require larger temperature gradients to cause them to fracture again.
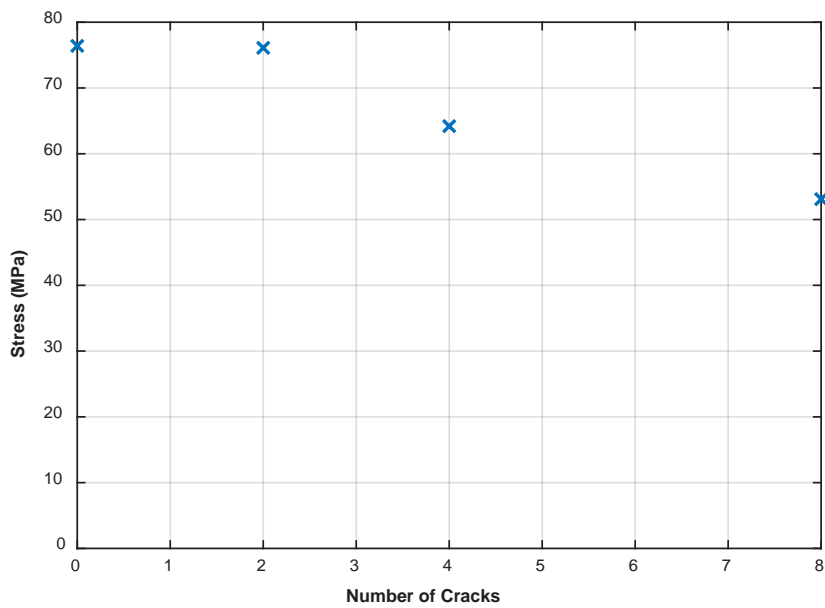
Figure 7.4: Maximum principal stress vs number of times the pellet cracked.

7.3 Discussion

Chapter 7 discussed the thermal stresses from a fracture mechanics perspective by examining the maximum strength of the fuel as a function of flaw size and by examining how cracking and fracturing affect the stress field. Using Eqn. 7.1, the maximum fracture strength of the fuel at 1200°C was calculated to be 782 MPa. The transient thermal analyses showed that the maximum thermal stresses experienced by the fuel is 700 MPa which is

82 MPa less than the estimated maximum fracture strength. Because the peak stresses do not occupy a large volume of the fuel, it is possible that the stresses do not encounter a flaw large enough to cause fracture. Section 7.1 examined how the introduction of a crack would affect the stress field in a fuel pellet. The analyses showed that a crack would lower the stresses. Finally, in Section 7.2, the pellet was assumed to fracture multiple times and the maximum stress of the pellet was examined. The analysis showed that fracturing the fuel reduces the stresses making it less likely for the pellet to continue to fracture.

8   CONCLUSION AND FUTURE WORK

8.1 Conclusion

The purpose of this work was to calculate the maximum thermal stresses experienced by the fuel pellets during a maximum pulse operation. To accomplish this purpose, the material properties of the fuel were first derived. Next the material properties were adjusted to account for radiation effects. A transient thermal analysis of a maximum pulse in the ACRR was then performed. The temperature profiles from the transient thermal analysis were then used to calculate the thermal stresses in the fuel. A property sensitivity study was then performed to examine the effect of the material properties on the thermal stresses. Finally, the impact of thermal stresses on the fuel were approached from a fracture mechanics perspective.

Results from the analyses showed that maximum thermal stresses in the fuel are caused by heat loss rather than the fission profile. The fluting of the Nb can causes localized cooling in the outer region of the fuel pellet. The localized cooling causes very large localized thermal stresses. Because the thermal stresses influence such a small volume, they are unlikely to cause fracture. This conclusion is supported by neutron radiography that was performed in 1989 that showed healthy fuel. The analyses also showed that the thermal stresses in the fuel are most sensitive to changes in the modulus of elasticity and CTE. Finally, the analyses showed that if fracture did occur in the fuel, it is unlikely that it would continue to fracture because stresses are relieved when the fuel fractures. Because

the actual material properties of the fuel are uncertain, neutron radiography would need to be performed to know the state of the fuel with certainty.

Within this analysis there were several sources of uncertainty. The first of these involved the material properties of the fresh fuel. The material properties of the fresh fuel were never measured, so they were instead derived. Although the derivations provide approximations to the material properties, they are not exact. Secondly the burnup effects were approximated. Burnup studies have never been performed on the ACRR's fuel, thus approximations were made from literature. Recent studies found that the effect of burnup on the fuel's thermal conductivity is likely not as severe as was implied by literature. Increased thermal conductivity would result in lower thermal stresses. The approximated effect of burnup adds another layer of uncertainty to the material properties. Because the current properties of the fuel are only approximate, the exact magnitude of the thermal stress in the fuel is subject to uncertainty. Although the material properties add uncertainty, the trends found in this study are not dependent on material properties, so they can be assumed to be true.

8.2 Proposal for Future Work

One of the shortcomings of this work was that the material properties were derived thus there is inherent uncertainty in the properties. Accurate material properties would reduce the level of uncertainty in the calculations. In the future, the material properties should be determined experimentally. Also, the simulations assumed that the fuel pellets

were perfectly centered within the cladding and Nb can which is not always the case. Further analyses should be performed to examine the effects of different pellet orientations. Finally, a directly coupled thermal-structural analysis should be performed to examine how the physical interaction of the different components of the fuel elements have on the thermal stresses.

APPENDIX A – MESH CONVERGENCE STUDIES

Thermal Mesh Convergence

Mesh convergence studies are used to determine what mesh is small enough to properly capture the physics and geometry of a problem when performing a finite element analysis. Convergence can be determined by progressively decreasing the size of a mesh until the desired quantity has converged. The mesh can also be refined locally to save computational time while still capturing the physics. Figure 0.1 shows the meshes used to perform the mesh convergence study. In subfigures a.-c. the mesh was globally refined using the mesh resolution slider in ANSYS Workbench. Subfigure d. was refined to capture the heat transfer of the small gaps between the Nb fluting and the outer annulus of the fuel pellet. Subfigure e. was the finest mesh used and showed that the refined mesh was converged. The mesh shown in subfigure d. was used to perform the thermal analyses shown in this report.
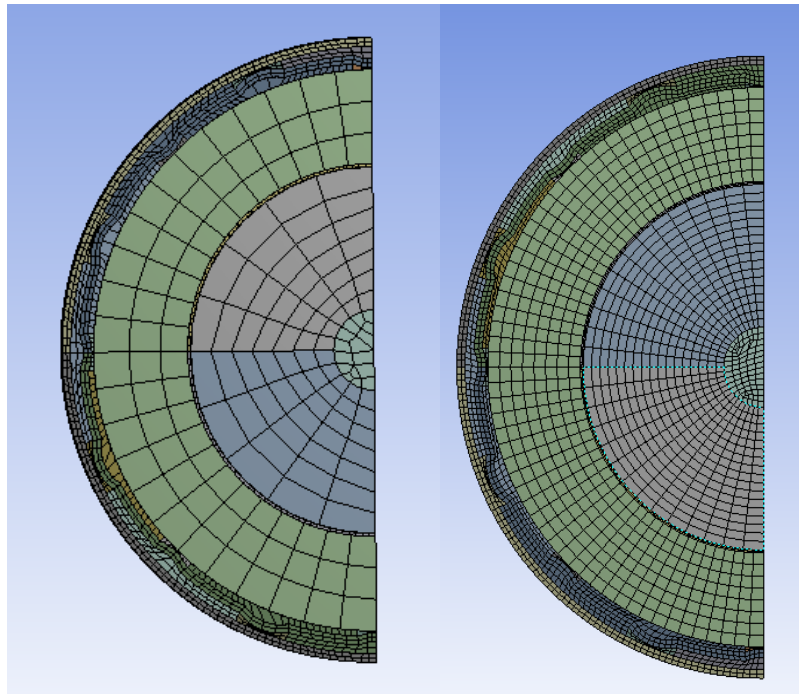
a. Course mesh   b. Medium mesh
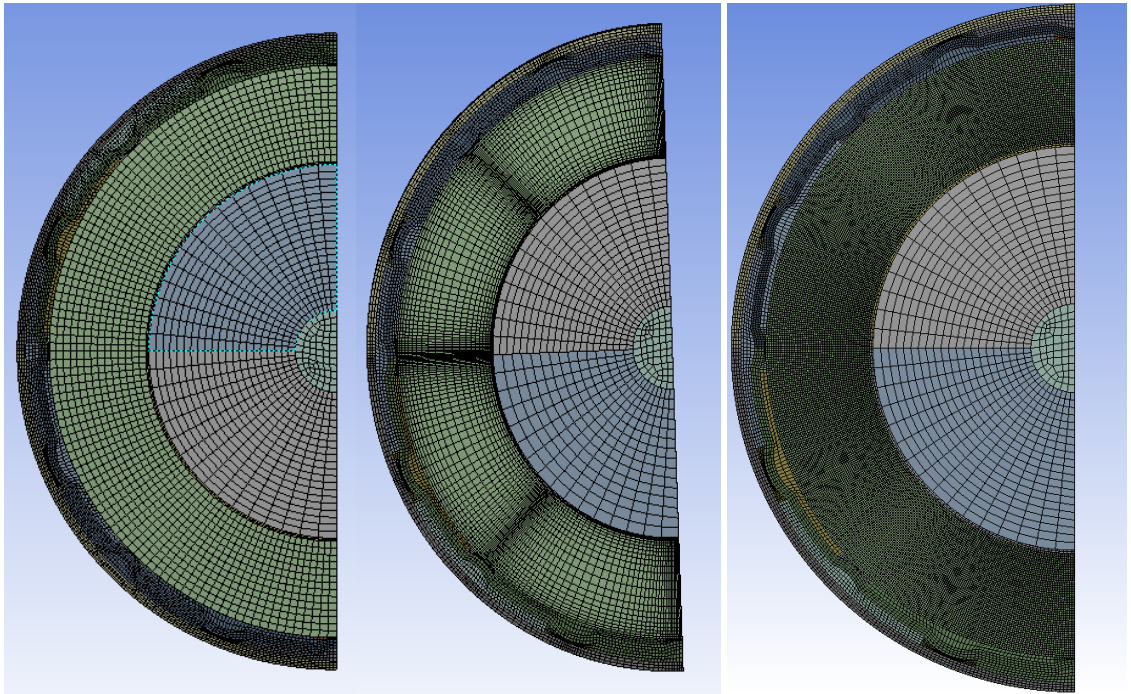
c. Fine mesh   d. Fine refined mesh   e. Very fine mesh

Figure A.1: This figure shows the meshes used in the mesh thermal convergence study.

Table A.1 shows the results of the mesh convergence study. The table shows the number of elements, and the maximum and minimum temperature of the outer surface of the outer annulus of the fuel pellet. The convergence of these values was measured because the temperature differences on the outer surface were the causes of maximum stresses.

Table A.1: Thermal mesh convergence.

	Coarse	Medium	Fine	Very Fine	Refined
Elements	8114	38288	166443	1750515	252705
Maximum Temperature (°C)	979.13	979.8	980.18	980.39	980.1
Minimum Temperature (°C)	956.36	956.63	957.38	957.26	957.34

Structural Mesh Convergence

Another mesh convergence study was performed for the structural analysis. Figure 0.2 shows the meshes used for the convergence study. Subfigure d. was the mesh used in the structural analyses.
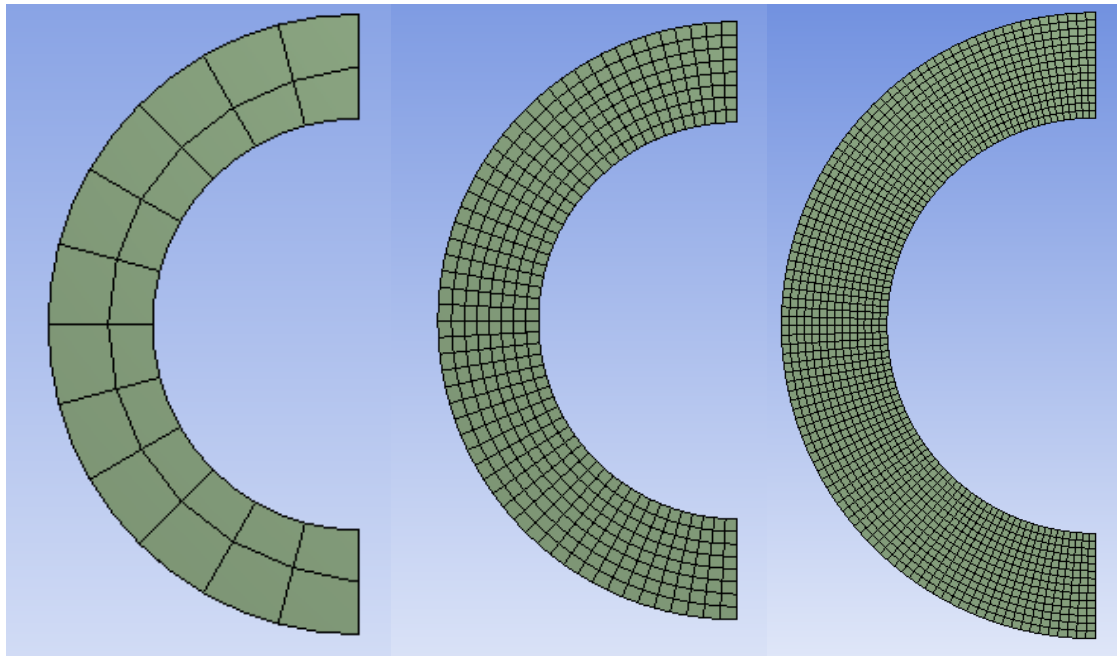
a. Coarse   b. Medium   c. Fine
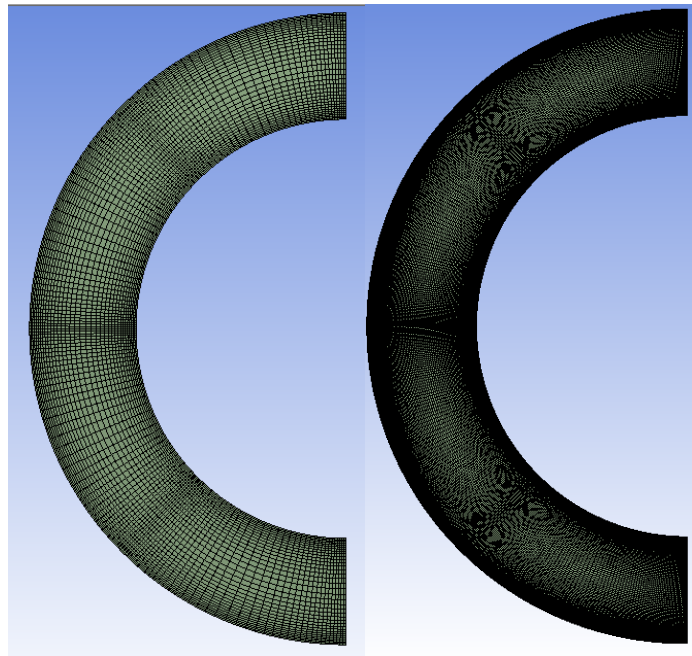
d. Very Fine   e. Ultra-Fine

Figure A.2: This figure shows the meshes used in the mesh structural convergence study.

Table A.2: Structural mesh convergence.

	Coarse	Medium	Fine	Very Fine	Ultra-Fine
Elements	48	4104	21840	95200	2120000
Stress	222	634	688	700	700

APPENDIX B – ACRR CORE LAYOUT

Figure B.1 shows map of the ACRR core. The six purple elements represent the elements in the peak locations of the ACRR.
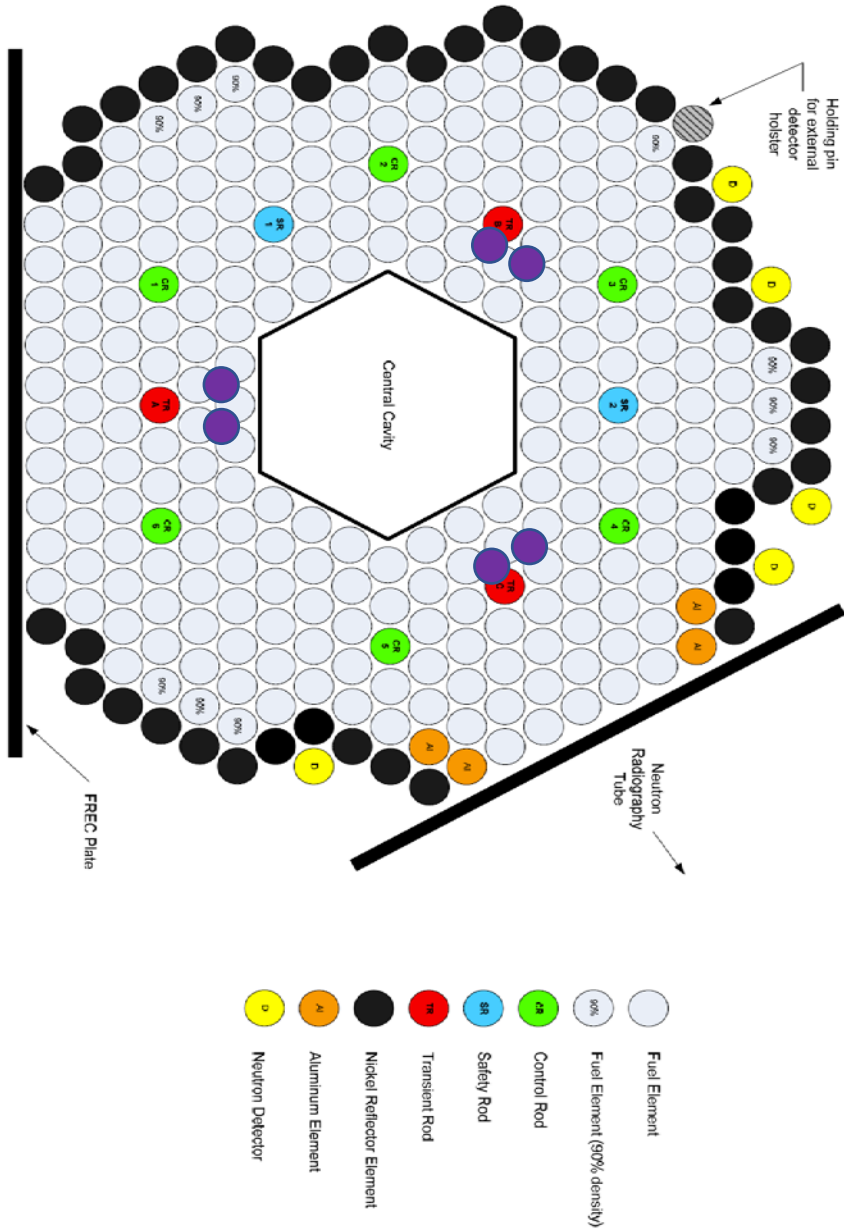
Figure B.1: ACRR core layout.

REFERENCES

[1] E. J. Parma, T. J. Quirk, L. L. Lippert, P. J. Griffin, G. E. Naranjo, and S. M. Luker, "Radiation Characterization Summary: ACRR 44-Inch Lead-Boron Bucket Located in the Central Cavity on the 32-Inch Pedestal at the Core Centerline (ACRR-LB44-CC-32-cl)," Sandia National Laboratories, Albuquerque, New Mexico, Technical Report SAND2013-3406, 2013.

[2] E. J. Parma *et al.*, "Radiation Characterization Summary: ACRR Cadmium-Polyethylene (CdPoly) Bucket Located in the Central Cavity on the 32-Inch Pedestal at the Core Centerline (ACRR-CdPoly-CC-32-cl)," Sandia National Laboratories, Albuquerque, New Mexico, Technical Report SAND2016-10114, 2016.

[3] E. J. Parma, D. W. Vehar, L. L. Lippert, P. J. Griffin, G. E. Naranjo, and S. M. Luker, "Radiation Characterization Summary: ACRR Polyethylene-Lead-Graphite (PLG) Bucket Located in the Central Cavity on the 32-Inch Pedestal at the Core Centerline (ACRR-PLG-CC-32-cl)," Sandia National Laboratories, Albuquerque, New Mexico, Technical Report SAND2015-4844, 2015.

[4] E. J. Parma *et al.*, "Radiation Characterization Summary: ACRR-FRECII Cavity Free-Field Environment at the Core Centerline (ACRR-FRECII-FF-cl)," Sandia National Laboratories, Albuquerque, New Mexico, Technical Report SAND2017-8674, 2017.

[5] T. Ball, "The Inverse Kinetics Method and Its Application to the Annular Core Research Reactor," Masters, University of New Mexico, Albuquerque, New Mexico, 2017.

[6] R. A. Chang, "Documented Safety Analysis (DSA) for the Annular Core Research Reactor Facility (ACRRF)." 09-Jan-2018.

[7] T. R. Schmidt, D. J. Sasmor, J. T. Martin, F. Gonzalez, and D. N. Cox, "Design and Fabrication of the Instrumented Fuel elements for the Annular Core Research Reactor (ACRR)," Sandia National Laboratories, Albuquerque, New Mexico, SAND80-2365, Apr. 1981.

[8] "Annular Core Pulse Reactor Upgrade Quarterly Report, January-March 1977," Sandia National Laboratories, Albuquerque, New Mexico, Sandia Report SAND77-0610, Jun. 1977.

[9] D. G. Talley, "RAZORBACK – A Research Reactor Transient Analysis Code, Version 1.0 Volume 3: Verification and Validation Report," Sandia National Laboratories, Albuquerque, New Mexico, Sandia Report SAND2017-3372, Apr. 2017.

[10] A. T. T., "Beryllium - A Unique Material in Nuclear Applications," Idaho National Laboratory (INL), INEEL/CON-04-01869, Nov. 2004.

[11] "Nuclear Data for Safeguards," *International Atomic Energy Agency*. [Online]. Available: https://www-nds.iaea.org/sgnucdat/c3.htm#92-U-235. [Accessed: 13-Mar-2019].

[12] D. R. Olander, *Fundamental aspects of nuclear reactor fuel elements*. Springfield, Virginia: Technical Information Center, Office of Public Affairs Energy Research and Development Administration, 1976.

[13] "Annular Core Pulse Reactor Upgrade Quarterly Report, July-September 1975," Sandia National Laboratories, Albuquerque, New Mexico, Sandia Report SAND75-0630, Jan. 1976.

[14] "Annular Core Pulse Reactor Upgrade Quarterly Report, October -December 1975," Sandia National Laboratories, Albuquerque, New Mexico, Sandia Report SAND76-0165, Apr. 1976.

[15] "Annular Core Pulse Reactor Upgrade Quarterly Report, January-March 1976," Sandia National Laboratories, Albuquerque, New Mexico, Sandia Report SAND76-0281, Jul. 1976.

[16] "Annular Core Pulse Reactor Upgrade Quarterly Report, April-June 1976," Sandia National Laboratories, Albuquerque, New Mexico, Sandia Report SAND76-0371, Sep. 1976.

[17] "Annular Core Pulse Reactor Upgrade Quarterly Report, July-September 1976," Sandia National Laboratories, Albuquerque, New Mexico, Sandia Report SAND76-0653, Jan. 1977.

[18] "Annular Core Pulse Reactor Upgrade Quarterly Report, October-December 1976," Sandia National Laboratories, Albuquerque, New Mexico, Sandia Report SAND77-0053, Mar. 1977.

[19] "Annular Core Pulse Reactor Upgrade Quarterly Report, April-June 1977," Sandia National Laboratories, Albuquerque, New Mexico, Sandia Report SAND77-1133, Sep. 1977.

[20] "Annular Core Pulse Reactor Upgrade Quarterly Report, July-September 1977," Sandia National Laboratories, Albuquerque, New Mexico, Sandia Report SAND77-1807, Dec. 1977.

[21] "Experimental Fast Reactor Safety Research Program (Combined) Quarterly Report," Sandia National Laboratories, Albuquerque, New Mexico, SAND75-0068, Feb. 1975.

[22] "Experimental Fast Reactor Safety Research Program - Quarterly Report January-March 1975," Sandia National Laboratories, Albuquerque, New Mexico, Sandia Report SAND75-0225, Apr. 1975.

[23] "Experimental Fast Reactor Safety Research Program - Quarterly Report April-June 1975," Sandia National Laboratories, Albuquerque, New Mexico, Sandia Report SAND75-0449, Aug. 1975.

[24] J. L. Tills, "THERMAL/MECHANICAL ANALYSIS OF BeO-UO2 FUEL PELLETS FOR THE ANNULAR CORE RESEARCH REACTOR," Albuquerque, New Mexico, May-1982.

[25] S. Wright, "Annular Core Research Reactor Fuel Burnup Performance Evaluation," Albuquerque, New Mexico.

[26] B. A. Boley and J. H. Weiner, *Theory of Thermal Stress*. Mineola, New York: Dover Publications, Inc, 1997.

[27] K. I. Kaiser, L. E. Martin, and A. M. Miller, "Fuel Health Working Group Proposal for Continued Monitoring of Annular Core Research Reactor Facility Nuclear Fuels," Albuquerque, New Mexico.

[28] B. S. Hickman, W. B. Rotsey, R. J. Hilditch, and K. Veevers, "Effects of Irradiation on Beryllia-Based Fuels," *J. Am. Ceram. Soc.*, vol. 51, no. 2, pp. 63–69, Feb. 1968.

[29] J. R. Gilbreath and O. C. Simpson, "The Effect of Reactor Irradiation on the Physical Properties of Beryllium Oxide," in *Proceedings of the Second United Nations International Conference on the Peaceful use of Atomic Energy*, Geneva, Switzerland, 1958, vol. 5, pp. 367–374.

[30] G. L. Hanna, B. S. Hickman, and R. J. Hilditch, "The Irradiation Behavior of Beryllium Oxide Dispersion Fuels," Australian Atomic Energy Commission, Australia, AAEC/E106, Mar. 1963.

[31] J. G. Morgan and M. F. Osborn, "Radiation Effects on Fueled BeO," Oak Ridge National Laboratories, Oak Ridge, Tennessee, ORNL-TM-311, Oct. 1964.

[32] V. D. Arp, R. D. McCarty, and D. G. Friend, "Thermophysical Properties of Helium-4 from 0.8 to 1500 K with Pressures to 2000 MPa," National Institute of Standards and Technology, Boulder, Colorado, NIST Technical Note 1334, Sep. 1998.

[33] *ANSYS Mechanical 19.2*. Ansys Inc.

[34] R. Hill, "The Elastic Behavior of a Crystalline Aggregate," *Proc. Phys. Soc. Sect. A*, vol. 65, no. 5, p. 349, 1952.

[35] J. K. Fink, "Review Thermophysical properties of uranium dioxide," *J. Nucl. Mater.*, vol. 279, no. 1, pp. 1–18, Mar. 2000.

[36] K. Veevers and W. B. Rotsey, "THE VARIATION WITH TEMPERATURE AND POROSITY, OF THE MODULI OF RUPTURE AND ELASTICITY OP 'STANDARD' ISOSTATICALLY PRESSED AND SINTERED BERYLLIA," Apr. 1965.

[37] K. Pietrack and T. S. Wisniewski, "A review of models for effective thermal conductivity of composite materials," *J. Power Technol.*, vol. 95, no. 4, pp. 14–24, 2015.

[38] Y. S. Touloukian, R. W. Powell, C. Y. Ho, and P. G. Klemens, "Thermophysical Properties of Matter - The TPRC Data Series. Volume 2. Thermal Conductivity - Nonmetallic Solids," THERMOPHYSICAL AND ELECTRONIC PROPERTIES INFORMATION ANALYSIS CENTER, Lafayette, In, ADA951936, Jan. 1971.

[39] "Thermophysical Properties of Matter Database Recommended values for Nb," *CINDAS LLC*. [Online]. Available: http://cindasdata.com/.

[40] T. T. Wang and T. K. Kwei, "Effect of Induced Thermal Stresses on the Coefficients of Thermal Expansion and Densities of Filled Polymers," *J. Polym. Sci.*, vol. 7, no. A-2, pp. 889–896, 1969.

[41] *Thermophysical Properties of Materials For Nuclear Engineering: A Tutorial and Collection of Data*. Vienna. Austria: International Atomic Energy Agency, 2008.

[42] B. A. Chandler, E. C. Duderstadt, and J. F. White, "Fabrication and Properties of Extruded and Sintered BeO," *J. Nucl. Mater.*, vol. 8, no. 3, pp. 329–347, 1963.

[43] E. J. Garcia, "Thermal Stresses in BeO-UO2 Fuel for ACPR Upgrade." 28-Jun-1976.

[44] "Ansys 18.2 Workbench User's Guide," ANSYS, Inc, Canonsburg, Pa, User's Guide.

[45] D. G. Talley, "Initial Verification and Validation of RAZORBACK – A Research Reactor Transient Analysis Code," Sandia National Laboratories, Albuquerque, New Mexico, Sandia Report SAND2015-8336, Sep. 2015.

[46] D. G. Talley, "RAZORBACK – A Research Reactor Transient Analysis Code, Version 1.0 Volume 1: User's Manual," Sandia National Laboratories, Albuquerque, New Mexico, Sandia Report SAND2017-10561, Sep. 2017.

[47] D. G. Talley, "RAZORBACK - A Research Reactor Transient Analysis Code, Version 1.0 Volume 2: Software Design and Development Report," Sandia National Laboratories, Albuquerque, New Mexico, Sandia Report SAND2018-4507, Apr. 2018.

[48] D. G. Talley, "RAZORBACK – A Research Reactor Transient Analysis Code, Version 1.0 Volume 3: Verification and Validation Report," Sandia National Laboratories, Albuquerque, New Mexico, Sandia Report SAND2017-3372, Apr. 2017.

[49] A. M. Miller, "Annular Core Research Reactor Pulse History Report 2003–2017," Sandia National Laboratories, Albuquerque, New Mexico, Sandia Report SAND2018-9945.

[50] "ACRR Peaking Factor Distributions," Sandia National Laboratories, Albuquerque, New Mexico, ACRR-CAL-009.00.

[51] W. D. Wood, H. W. Deem, and C. F. Lucks, "THERMAL RADIATIVE PROPERTIES OF SELECTED MATERIALS," Battelle Memorial Inst. Defense Metals Information Center, Columbus, Ohio, DMIC-177(Vol.2), Nov. 1962.

[52] D. A. Howl and A. F. Davis, "The emissivities of various niobium surfaces in the temperature range 500-1100° C," *Br. J. Appl. Phys.*, vol. 13, no. 5, p. 219, 1961.

[53] "Module 03: Nonlinear and Transient Thermal Analysis," presented at the ANSYS Mechanical Heat Transfer 17.0, 14-Jul-2017.

[54] D. P. H. Hasselman, "Unified Theory of Thermal Shock Fracture Initiation and Crack Propagation in Brittle Ceramics," *J. Am. Ceram. Soc.*, vol. 52, no. 11, pp. 600–604, Nov. 1969.

[55] M. Janssen, J. Zuidema, and R. J. H. Wanhill, *Fracture Mechanics*, 2nd Edition. Netherlands: VSSD, 2002.

[56] P. L. Gutshall and G. E. Gross, "Fracture Energy of Polycrystalline Beryllium Oxide," *J. Am. Ceram. Soc.*, vol. 51, no. 10, pp. 602–602, 1968.

[57] B. Lawn and T. R. Wilshaw, *Fracture of Brittle Solids*. Cambridge University Press, 1993.